SELENOLOGY TODAY

GLR GROUP.org

Geological Lunar Researches Group

Selenology Today is devoted to the publication of contributions in the field of lunar studies.

Manuscripts reporting the results of new research concerning the astronomy, geology, physics, chemistry and other scientific aspects of Earth's Moon are welcome.

Selenology Today publishes papers devoted exclusively to the Moon.

Reviews, historical papers and manuscripts describing observing or spacecraft instrumentation are considered.

SELENOLOGY TODAY #3
January 2007

Cover : Image taken by Piergiovanni Salimbeni, Schmidt Cassegrain 200 mm f/10.

Selenology Today websites

http://digilander.libero.it/glrgroup/

http://www.glrgroup.org/

LETTER TO THE EDITORS

A flash detected during the smart -1 impact date by Peter Lipscomb

The following letter is a report about a flash detected at about the time of the smart-1 impact and is to our knowledge the only flash reported by an amateur. Based upon the approximate coincidence in timing of Peter Lipscomb's observation with the smart-1 collision it is quite possible that the flash is of the event. However, the reality that the recorded flash is the smart-1 impact is not certain because the exact time of the Peter's image and the flash's location on the Moon cannot be determined with precision. Furthermore, the faint after-image frame shows a low-amplitude signature above the background noise, i. e. a low signal-to-noise ratio, and it is difficult to be sure that it is not a random peak of the background noise. Hence, only one frame of the acquired video stream shows an intensity peak with an amplitude significantly above the background noise level. At this point we are excited about the possibility that Lipscomb did record the smart-1 collision but we cannot be certain. We invite all readers of Selenology Today to send possible observations (positive or negative) to the editorial board

selenology_today@christian-woehler.de

On the evening of September 2nd 2006, I began setting up my 8" Meade LX-90 UHTC with a stock wedge and tripod in the driveway of my Santa Fe home. I was hurrying to get everything ready and aligned in time to try and record images of the SMART-1 impact area on the lunar surface. Impact was predicted to occur at approximately 11:42PM local time (Mountain Daylight Time) on September 3rd at 05:42AM Universal Time. Conditions had been partly cloudy during the early evening and were improving as impact time neared. There was a slight breeze out of the west, but it was steady with no gusts. It was probably about 5-7 miles per hour. At my location, the Moon was to be just about 13 degrees above the horizon as impact time approached. It showed a waxing gibbous phase, with 73% of the surface illuminated while it steadily dropped toward the southwestern horizon in the constellation Sagittarius. A stream of patchy clouds billowed across the face of the Moon adding an element of suspense. I brought out my laptop and Philips ToUcam Pro webcam fitted with an Infrared blocking filter to use for image capture. I mounted the webcam to a diagonal for prime focus imaging at the LX-90's native focal ratio of f/10. I wasn't that familiar with area of lunar surface near where impact was predicted to occur, but on my laptop display I could make out ray features near the southern end of the terminator related to the crater Tycho. I used those rays as guides to help me know where I needed to "step off" into the earthshine. I used K3CCD Tools as my capture software. Expecting a dim event, I placed the webcam settings to a fairly high gain with a medium saturation. I used a slow shutter speed and set the recording to 5

frames per second. I worked to frame the area of the lunar surface where I thought SMART-1 was going to make impact. On my live display, I noticed that the area of earthshine was very dark. Few surface features were visible. I didn't want the capture to be too noisy (it seemed like there was enough noise already) so I resisted further adjustments to the gain setting. As I used my Autostar hand paddle to make small movements towards final placement, I could see the outline of an ancient ridge near the bottom right corner of my field of view. I decided to move a little farther into the earthshine in an easterly direction. The

Figure 1

ridge disappeared out of the frame. The still image shown is frame 000217 from capture 0001 and shows a start time of about 2 minutes earlier than scheduled impact (Figure 1).

I began recording AVI video frames a few minutes before impact time to ensure everything was working smoothly. My

image scale is 0.58 arc seconds per pixel with a field of view 3.08 x 2.31 arc minutes. I had no problem with the first couple of attempts capturing AVI data, so I kept on recording. After a few captures had passed and while recording another file, I was startled by what seemed to be a faint streak near the bottom right side of my capture frame. It was almost like a small insect had flown into the glow of my laptop screen. I recorded 5 more captures with durations ranging from about 30-60 seconds to be sure I had covered the impact interval. Seeing nothing more than patches of cloud moving across the fra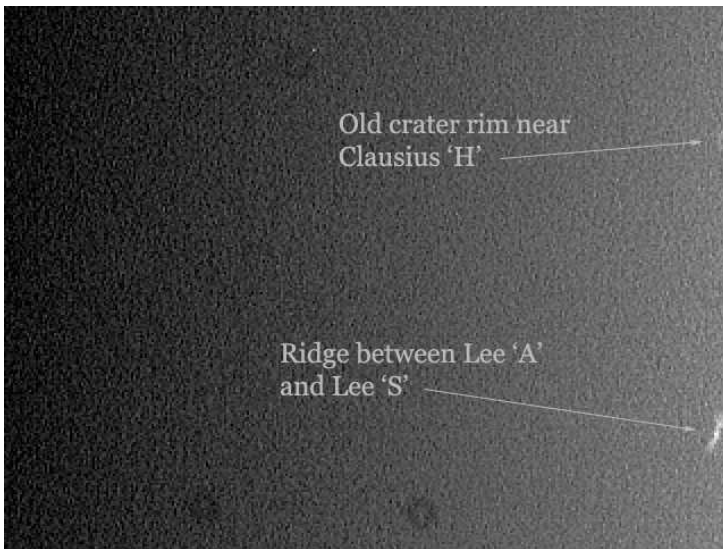me, I began to shutdown and pack the gear back into the house. Once back inside, I began to examine the capture data. I was excited to see if I could find the file that had the 'streak' in it. I didn't see anything like that, but in the fourth capture file I did see a small blue dot appear for an instant near the bottom right corner of the recording. Enlarging the view from 320 x 240 to 640 x 480, I ran it again and I could see that there was a dim afterimage in the frame just following the blue dot frame. I checked the time shown on my files and uncovered a discrepancy. I went to the nist.gov site to synchronize my laptop clock. I noted a change of a minute. This means my file times are about minus 1 minute 19 seconds from the known impact time of 05:42:21 UT.

I worked to convert the AVI file to BMP single frames for assembly into an animated GIF. I used AVITricks Classic

Figure 2

to convert to BMP frames and Adobe ImageReady to assemble the animated GIF and add titles. The animated GIF is comprised of a 9 frame loop with a 0.5 second delay between each frame. A gradient from the terminator can be seen from right to left. Other than enlarging the frame and converting and compiling the data, no other processing or image enhancement was done. A still of the flash is shown here it is frame 000037 from capture 0004 (Figure 2). By browsing around online astronomy discussion groups, I learned that the Canada-France-Hawaii Telescope (CFHT) team had imaged the event. So, I visited their site to see what information had been posted. There I found a flash contour plot that I thought might be interesting to use for comparison with my flash capture. A contour plot is a way to show shape and values of brightness. Similar to how a topographic map shows the contour of a mountain with closer lines indicating steeper grade, the CFHT plot shows brighter parts of the flash as areas with lines closer together. The central part of the CFHT plot shows a loss of data due to saturation of their detector. In Adobe Photoshop CS, I worked to isolate the part of the frame where the blue dot
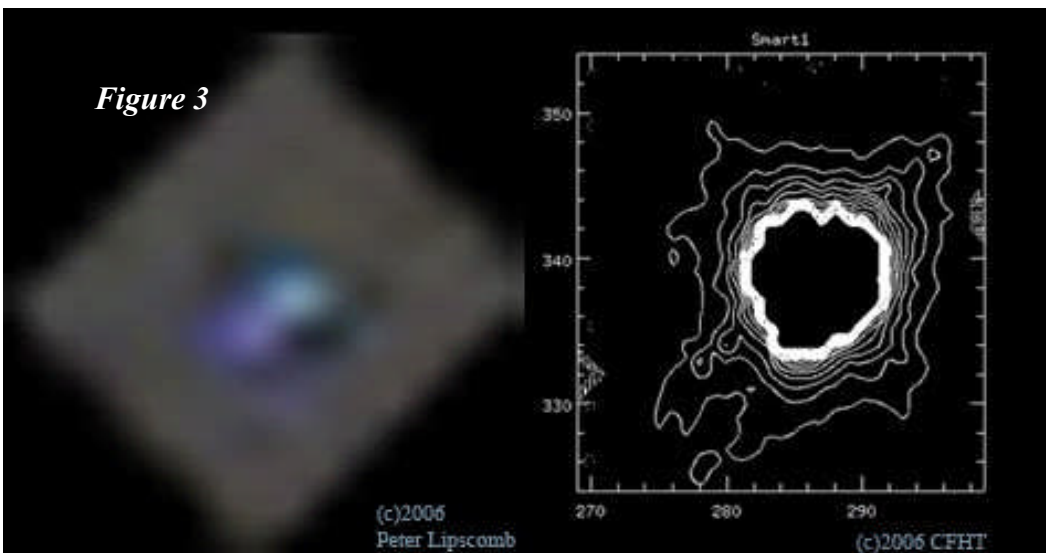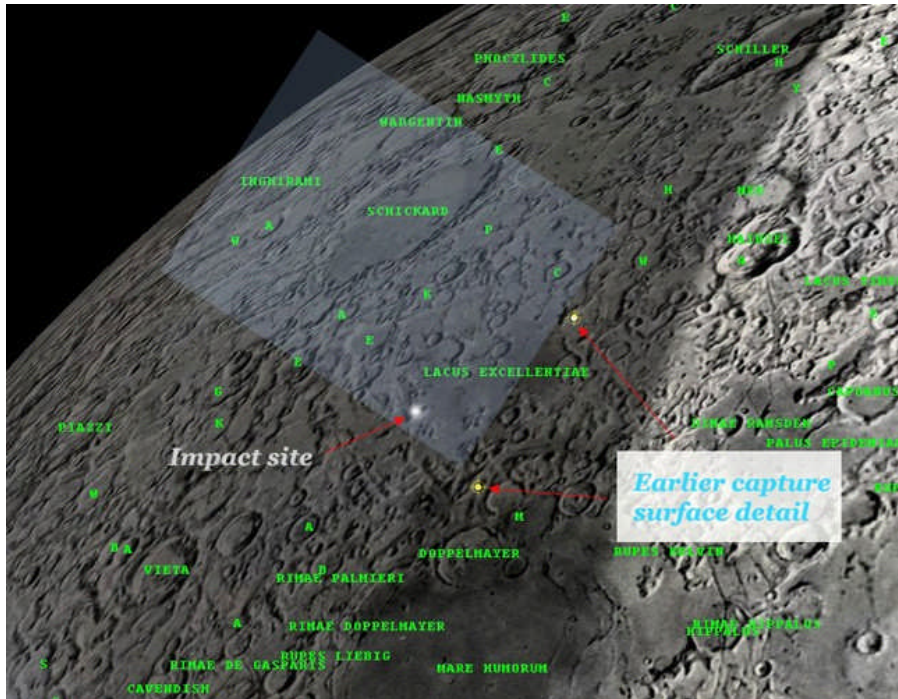

Figure 3

appeared and enlarged it by 600x from the 640 x 480 size image.

Figure 4

Then, I rotated it counter-clockwise to give an orientation that appeared to match what was posted on the CFHT site. The blue dot spans a number of pixels and shows evidence of shape and different levels of brightness (Figure3). I opened Patrick Chevalley's and Christian Legrand's Virtual Moon Atlas (VMA), and started to work on comparing the position of my capture frame with the surface features known to be in the area of the impact site. Using VMA, I was able to approximately match the position of impact area with what I had framed before beginning my capture. I used a blue overlay to get a better sense of how the webcam detector was oriented. The surface features of the crater rim near Clausius 'H' and the ridge near Lee 'A'

and Lee 'S' that I slewed out of the frame referenced in Figure 1 are identified by yellow target marks (Figure 4). Going back to the CFHT site I looked at the 15 frame mosaic posted there to get a sense of how the shape of the faint glow in the afterimage frame compares with the dust cloud imaged by the 3.58 meter CFHT. The elongated 'C' shape looks pretty close to the faint after image of frame 000038 capture 0004 (Figure 5). In the absence of rigorous time data due to the discrepancy with my laptop clock, I had to look at other ways of examining my data. The data was scrutinized using 3 other methods.

1. By using the earlier capture footage (capture 0001 and identifying features on the lunar surface (frame 000217 capture 0001) I can state that I had the camera positioned to image the impact area. Where the blue dot appears in the lower corner of my frame is consistent with the known impact area of the SMART-1 lunar probe (Figure 4).

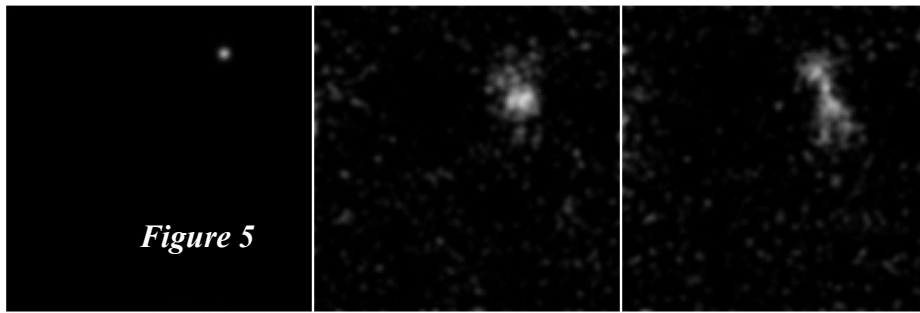*2.* A study of the blue dot and faint after image in frame 000037 capture

Figure 5

Figure 6

factor of 1200% in Photoshop, I note some similarity between these frames and the first 3 frames for the CFHT mosaic (Figure 5). This similarity seems even more apparent when one views the animated GIF of my capture file.
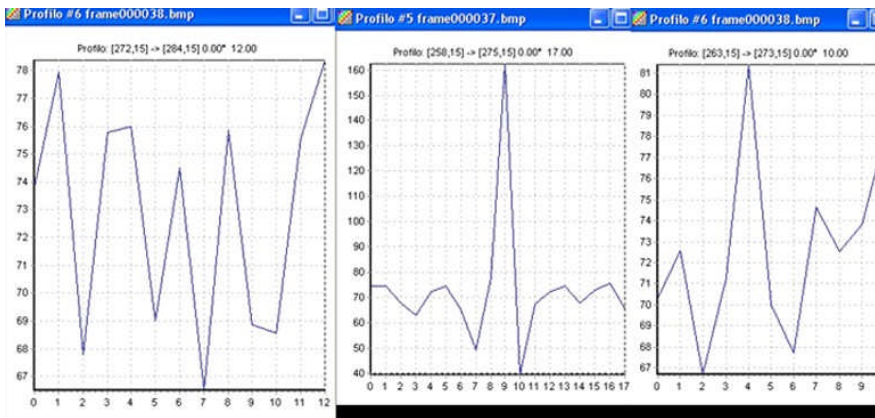
3. Raffaello Lena of the Geological Lunar Research Group in Italy, conducted a noise analysis of the flash frame. He took both frames and averaged the noise profile resulting in the image shown to the left. The flash frame is at center and shows a signature clearly above the background noise profile. To the right, is the faint after image frame which shows a lower amplitude signature, but is still above the background noise profile (Figure 6) **[editor note (Raffaello Lena): another possible explanation is reported in the editorial presentation above].**

0004 and frame 000038 was conducted. By isolating and enlarging the area of the frame 000037 capture 0004 where the blue dot appears, it is possible to compare its characteristics with the flash contour plot of CFHT. An elongation is noticeable and when compared to the center still frame of the CFHT image (Figure 5) there are 2 noticeable centers of brightness. In addition, the blue dot spans a number of pixels. In the after image frame 000038 capture 0004, I isolated and inspected the same area where the blue dot appeared in frame 000037 capture 0004. A faint signature in the exact location were the blue dot appeared can be seen. Finally, by enlarging the frames 000036 capture 0004, frame 000037 capture 0004 and frame 000038 capture 0004 from their original resolution of 320 x 240 by a

A STUDY ABOUT THE MANILIUS REGION AND A DOME LOCATED AT 08.26° E AND 10.52° N

By Raffaello Lena, Christian Wöhler, KC Pau and Maria Teresa Bregante

Geologic Lunar Research (GLR) Group

Abstract

In this study we describe a previously unreported dome at selenographic coordinates 08.26° E and 10.52 ° N. It is 9.3 km in diameter, 70 m high, with an average flank slope of 0.86°, and has a summit crater. The dome, termed Hyginus 3, is of class A in the GLR classification scheme. Rheologic modelling of the dome suggests that it was built by lava of low viscosity, erupting at a high effusion rate over a period of three months. It lies in a complex volcanic region characterized by pyroclastic events and hummocky terrains.

1. Introduction

The region to the south and southwest of Mare Imbrium is characterised by mare patches and highland remnants that have been scoured by Imbrium impact ejecta. This region includes Mare Vaporum and mountainous regions running linearly from the northwest and southeast that represent ejecta from the Imbrium impact (Wilhelms, 1987). Mare Vaporum is a volcanic province and is covered by lava that flowed from surface vents. The geologic processes involved in lunar volcanism in the Mare Vaporum region have been examined ande Imbrium impact occurred 3.85 billion years ago, creating fractures in the rock layers and spreading ejecta throughout this region. At the same time, radioactive decay of elements in the mantle produced a sufficient amount of heat to cause melting of the surrounding rock. The magma ascended along the fractures produced by the Imbrium shock wave in dikes which generated effusive flows (a large part of Mare Vaporum), pyroclastic events (southeast section of Mare Vaporum) and graben (Hyginus Rille) due to pressurised magma at shallow depth, generating a stress field at the surface (Petrycki and Wilson, 1996).

Different lithological units, included in the USGS lunar geologic map I-548, are apparent in Mare Vaporum (Wilhelms, 1968 and references therein). Dark terrain extending in the region near Hyginus M and NA, also known as the Sulpicius Gallus Formation (units EIS and EISd), has been interpreted as volcanic material predominantly pyroclastic with the presence of hummocky material and different local sources including dark craters, irregular craters, domes and rilles (Wilhelms, 1968). The apparent superposition of some dark mantling material on other terrain suggests a pyroclastic origin (Wilhelms, 1968 and references therein). Moreover, a large region (EIS unit), covering 4129 square kilometres, centred at 7.9° E and 10.0° N, has been spectrally characterised as a lunar pyroclastic deposit by Gaddis et al. (2003).

During the volcanic activity in Mare

Vaporum the formation of domes occurred, e. g. the dome located at 9.44° E and 8.22° N near Hyginus Z (Lena and Douglass, 2006). Lunar domes are gentle swells, a few hundred metres high, similar to low shield volcanoes found on the Earth. They represent the terminal phase of a lunar eruption and occur mostly in the maria. Constructional volcanic features formed during the later stages of eruptions, characterised by a decreasing rate of lava extrusion and comparably low temperature of eruption, resulting in the formation of effusive domes (Basaltic Volcanism Study Project, 1981; Head and Gifford, 1980).

We have observed a recently unreported shallow dome near the crater Manilius. It will be described in this article. The dome is located at 08.26º E and 10.52º N and has been added under the name "Hyginus 3" to the revised catalogue of lunar domes by Kapral and Garfinkle (2005). We examine the morphometric characteristic of the dome by making use of a combined photoclinometry and shape from shading approach described by Wöhler et al. (2006) and by Lena et al. (2006). The obtained values are used to derive information about the physical parameters of dome formation (lava viscosity, effusion rate, duration of the effusion process), employing the rheologic model by Wilson and Head (2003). We provide a geological interpretation of our spectrophotometric, morphometric, and rheologic modelling results, comparing them to the corresponding parameters typically observed for lunar mare domes.

2. Instruments and measurements

For each of the observations, the local solar altitude (Alt.) and the Sun's selenographic colongitude (Col.) were calculated using the Lunar Observer's Toolkit by H. D. Jamieson. All images are oriented with south up and west (IAU) to the right. A 3D profile of the dome, i. e. a digital elevation map (DEM), was obtained from the image shown in Fig. 2, relying on a combined photoclinometric and shape from shading analysis (Horn, 1989; Wöhler et al., 2006; Lena et al., 2006, and references therein). The dome diameter D is measured in the image, the dome height h can be readily inferred from the DEM, while the dome edifice volume V was determined by integrating the DEM over an area corresponding to a circular region of diameter D around the dome centre. Rheologic properties were obtained using the model by Wilson and Head (2003), which is applied to a large set of representative lunar mare domes by Wöhler et al. (2006). This rheologic model estimates the yield strength τ, i. e. the pressure or stress that must be exceeded for the lava to flow, the plastic viscosity η, yielding a measure for the fluidity of the erupted lava, the effusion rate E, i. e. the lava volume erupted per second, and the duration $T = V/E$ of the effusion process.

We furthermore determined a UVVIS five-band spectrum of the dome based on Clementine imagery. The Clementine UVVIS multispectral image data were obtained the wavelengths 415, 750, 900, 950, and 1000 nm. The reflectance values were derived relying on the calibrated and normalised Clementine UVVIS reflectance data as provided by Eliason et al. (1999). The extracted Clementine UVVIS data were examined in terms of
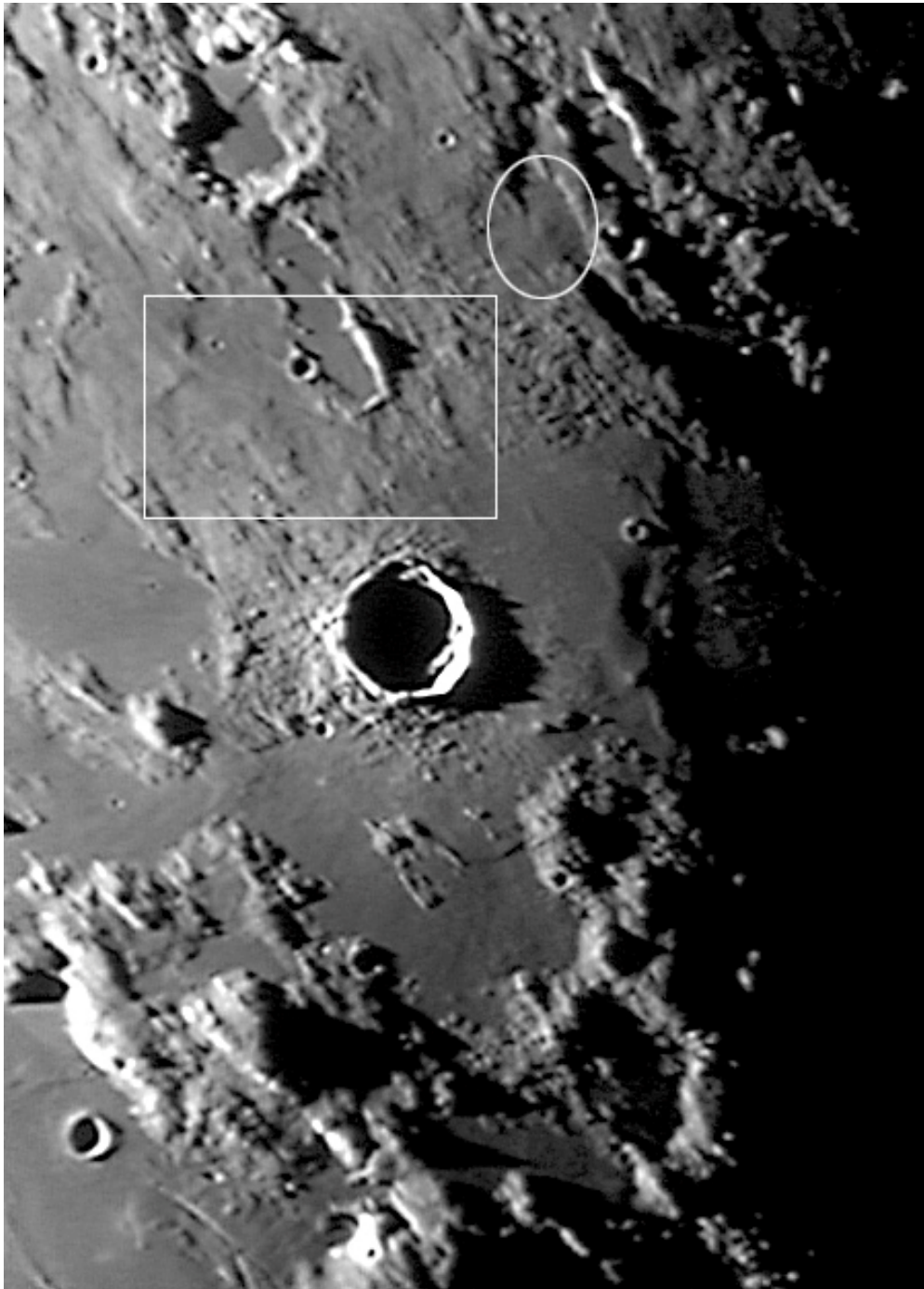
Figure 1: K. C. Pau on December 30, 2003, at 12:36 UT

750 nm reflectance (albedo) and the R_{415}/R_{750} and R_{950}/R_{750} colour ratios. Albedo at 750 nm is an indicator of variations soil composition, maturity, particle size and viewing geometry. The R_{415}/R_{750} colour ratio essentially is a measure for the TiO_2 content of mature basaltic soils, where high R_{415}/R_{750} ratios correspond to high TiO_2 content and vice versa (Charette et al. 1974). However, for

many lunar regions the relation between R_{415}/R_{750} ratio and TiO_2 content displays a significant scatter (Gillis and Lucey, 2005). The R_{950}/R_{750} colour ratio is related to the strength of the mafic absorption band, representing a measure for the FeO content of the soil, and is also sensitive to the optical maturity of mare and highland materials (Lucey et al. 1998).

3. Observations and digital images

Fig. 1 displays the dome under sunrise illumination. This image was taken by K. C. Pau on December 30, 2003, at 12:36 UT using a 250 mm f/6 Newtonian telescope (Alt. 2.77º, Col. 354.78°). This image clearly shows a dome and a narrow rille-like structure located to the south of Manilius. The feature is not shown in the lunar atlas by Rükl (1999), in the Lunar Quadrant Maps and in the Lunar Aeronautical Charts. Figure 2 shows the dome and the elusive rille under a higher Sun angle (Alt. 5.33º, Col. 357.25°). The image was made by K. C. Pau on November 22, 2005, at 22:32 UT using the same instrumentation as for Fig. 1. Figure 3 shows the dome and the elusive rille as drawn by R. Lena during an observation carried out on April 26, 2004, at 20:55 UT with a 100mm f/15 refractor (Alt. 3.77º, Col. 355.61°). Fig. 4 displays the dome under a lower solar altitude (Alt. 2.26°, Col. 354.23°).

The image was taken by R. Lena on January 6, 2006, at 18:36 UT using a 130 mm TMB apochromatic refractor. In Fig. 4 the dome is marked in green, while a second dome located near Hyginus Z at longitude 9.44° E and latitude 8.22° N (Lena and Douglass, 2006) is marked in

blue. The CCD images shown in Figs. 1, 2, and 4 were taken with a Philips ToUCam CCD camera (image size 640x480 pixels, pixel size 5.6 μm). The scale of the image in Fig. 2 is 440 m per pixel.

The shading on the dome's antisolar flank in Figs. 1-4 is not black, indicating that the slope is of low inclination.

4. Morphologic, morphometric and rheologic properties

According to our images, the dome diameter amounts to 9.3 ± 0.5 km. Furthermore, a summit pit crater with an estimated size of about 3.10 x 1.60 km is apparent (Table 1). Further morphometric data were obtained by generating a 3D profile of the dome from the image shown in Fig. 2, relying on a combined photoclinometric and shape from shading analysis (Horn, 1989; Wöhler et al., 2006; Lena et al., 2006). This leads to a dome height of 70 ± 10 m, corresponding to an average flank slope of 0.86° ± 0.2°. The dome edifice volume amounts to 2.2 ± 0.4 km³. A rough quantitative measure for the shape of the dome is given by the form factor $f = V/[\pi h(D/2)^2]$, where we have $f = 1/3$ for domes of conical shape, $f = 1/2$ for parabolic shape, $f = 1$ for cylindrical shape, and intermediate values for hemispherical shape. For the dome examined in this study, the form factor is 0.44.

The computed digital elevation map obtained based on Fig. 2 is shown in Fig. 5.
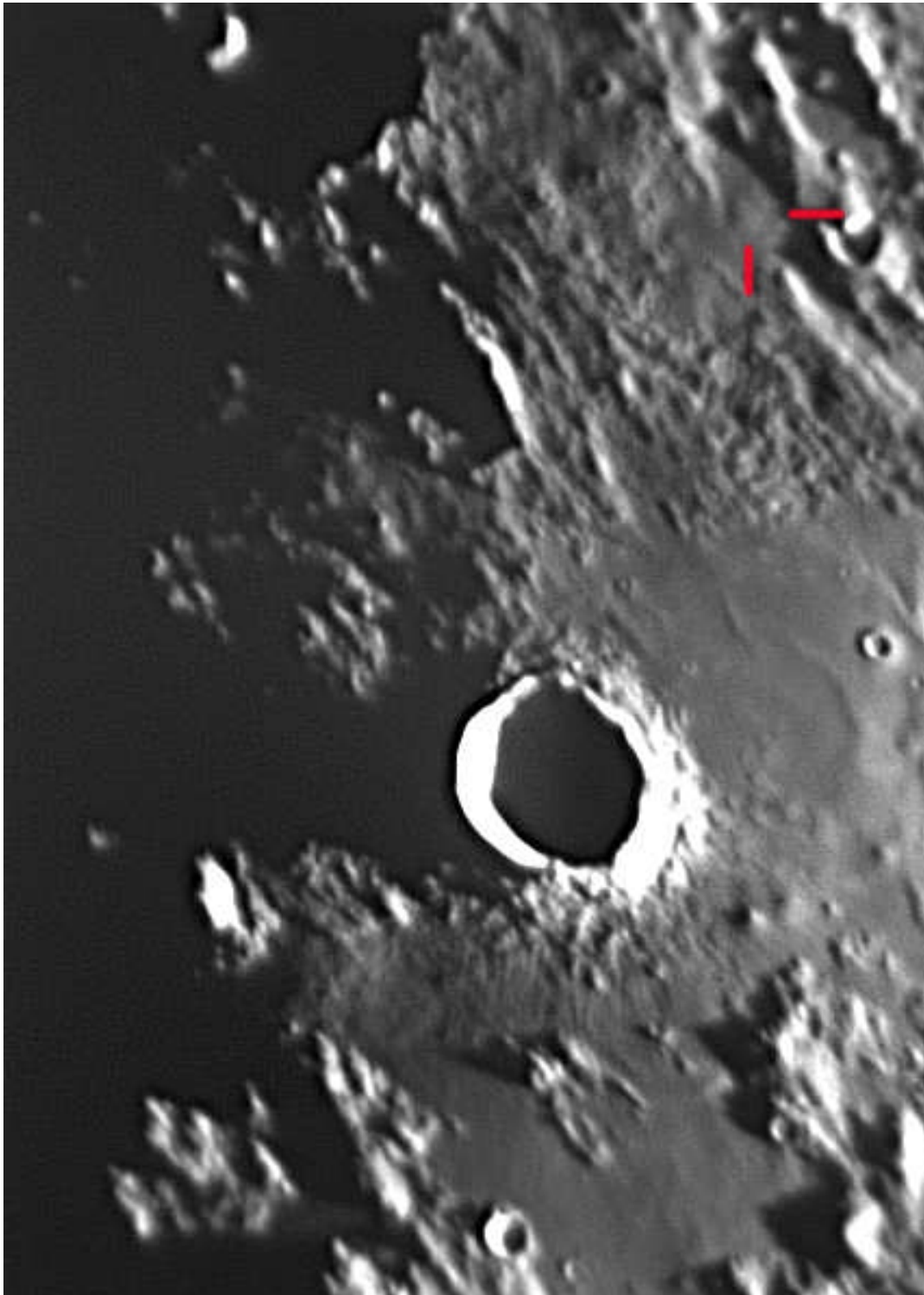
*Fig. 2: K C Pau on November 22, 2005,
at22:32 UT*
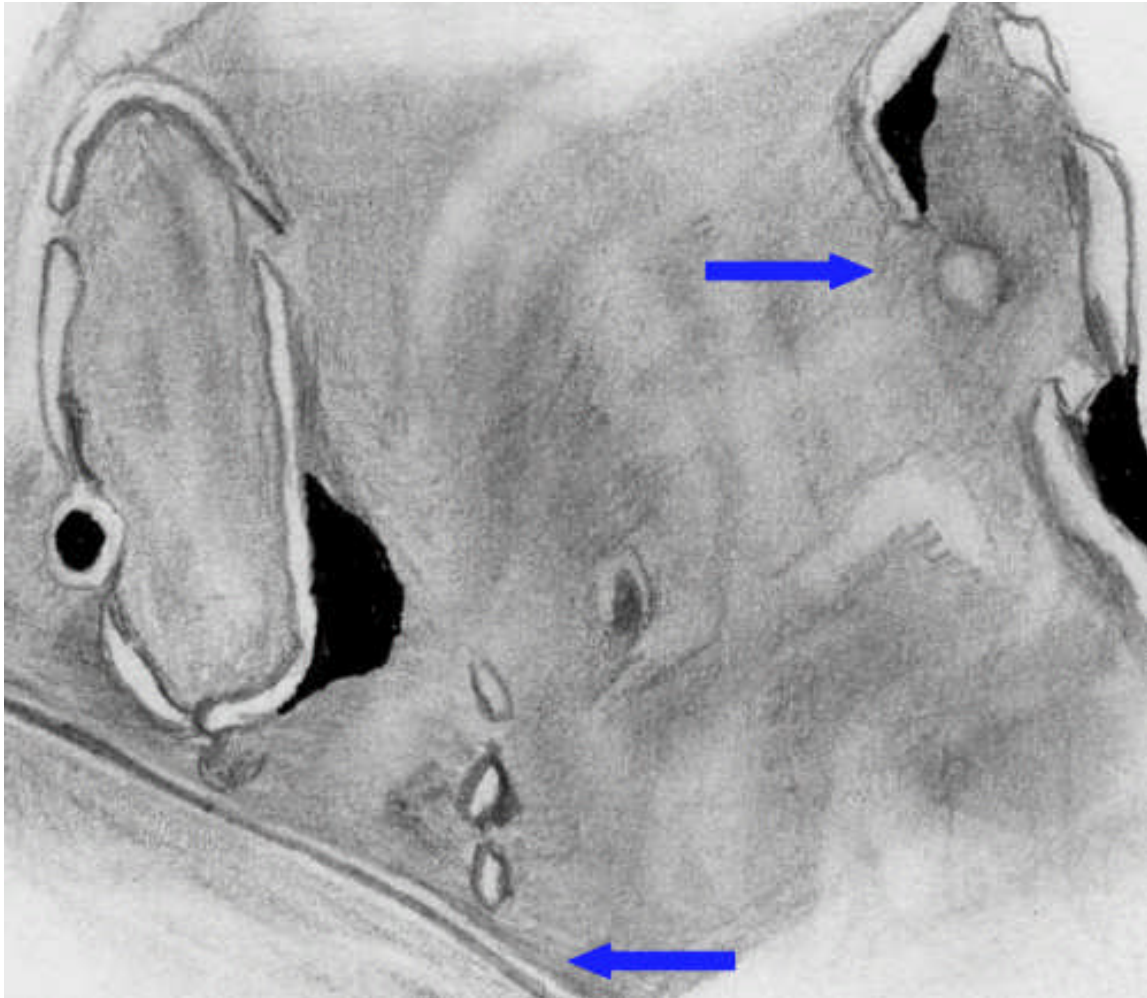
*Fig. 3: Raffaello Lena on April 26, 2004,
at 20:55 UT*

We assume that the examined dome was formed by extrusion of magma onto a flat plane spreading in all directions from the vent, in contrast to lava flows resulting from lava extrusion onto an inclined surface. Wilson and Head (2003) provide a quantitative treatment of such dome-forming eruptions. The computed values for τ, η, E, and T obtained with the model by Wilson and Head (2003) are valid for domes that formed from a single flow unit (monogenetic volcanoes). Otherwise, the computed rheologic values are upper limits to the respective true values. The low slope and edifice volume of the dome regarded in this study yield a high effusion rate of 218 m^3/s, a low lava viscosity of 1.2×10^4 Pa s, and a short duration of the effusion process of only 0.32 years or less than 4 months.

5. Lunar Orbiter imagery, Clementine UVVIS imagery, spectral properties

Fig. 6 displays Lunar Orbiter frame IV-097-H2. Due to higher solar altitude, the dome does not appear clearly in this frame, demonstrating its low height and slope. Fig. 7 shows the locations in the Clementine 750 nm albedo image at which the spectra were obtained. The pyroclastic deposit characterised by Gaddis et al. (2003) is marked in red, the dark and smooth terrain in green, the dome in blue, and the nearby hummocky terrain in violet. Fig. 8 shows the Manilius region, the pyroclastic deposit, and further geologic units in the Clementine colour ratio image. The inferred reflectance spectra for the dome examined in this study and further geologic units including the dark and smooth terrain west of dome and the nearby hummocky terrain located just to

its east are reported in Fig. 9. The sample area used to obtain the spectra amounts to 2 x 2 km^2.

The Clementine UVVIS data reveal that the dome appears spectrally bluish. It has a rather low 750 nm reflectance of $R_{750} = 0.0933$, a moderate value for the UVVIS colour ratio of $R_{415}/R_{750} = 0.6243$, indicating a moderate TiO_2 content, and a weak mafic absorption with $R_{950}/R_{750} = 1.0857$.

The pyroclastic deposit displays a significant component of high-TiO_2 materials in the form of ilmenite-rich black beads. It is darker ($R_{750} = 0.0790$) and shows a stronger mafic absorpion ($R_{950} = 0.0860$) than the dome regarded in this study ($R_{950}/R_{750} = 0.1014$). According to Gaddis et al. (2003), the spectral signatures of lunar pyroclastic deposits likely represent a complex combination of the degree of crystallinity (i. e. ilmenite content) and of the iron-titanium content. Weitz and Head (1999) explain the differences between orange and black bead deposits by variations in cooling time in a fire fountain probably resulting in quenched, crystallized, and composite droplets.
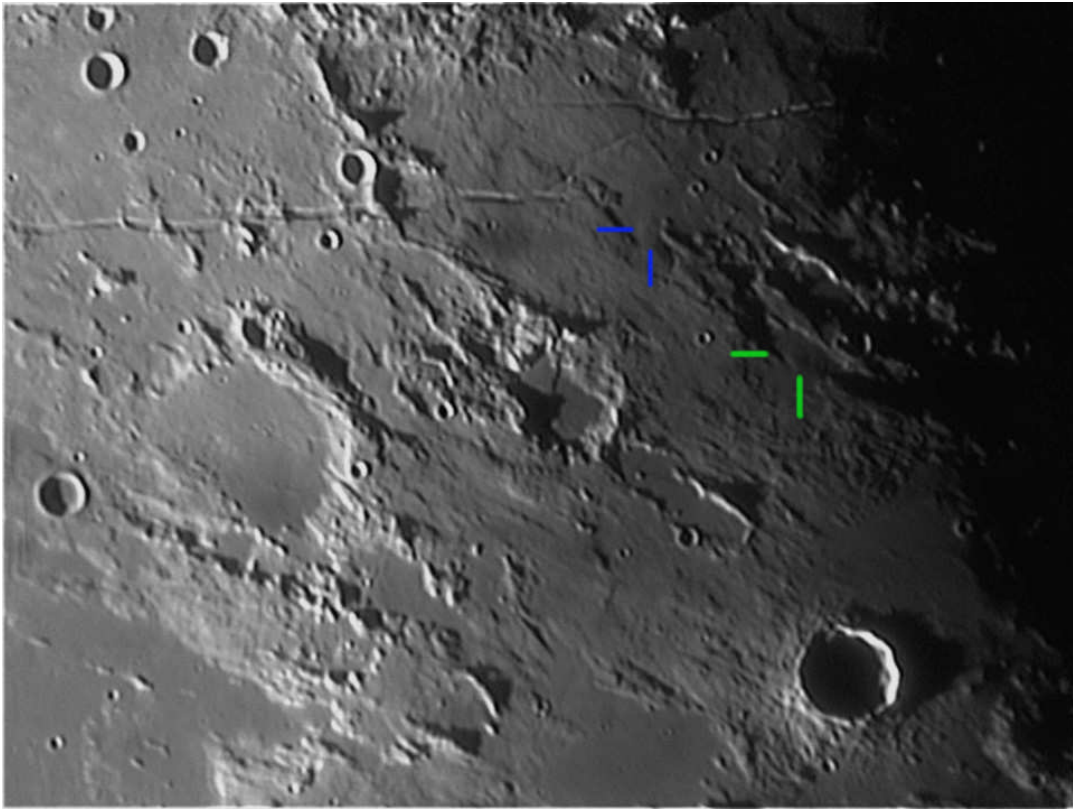
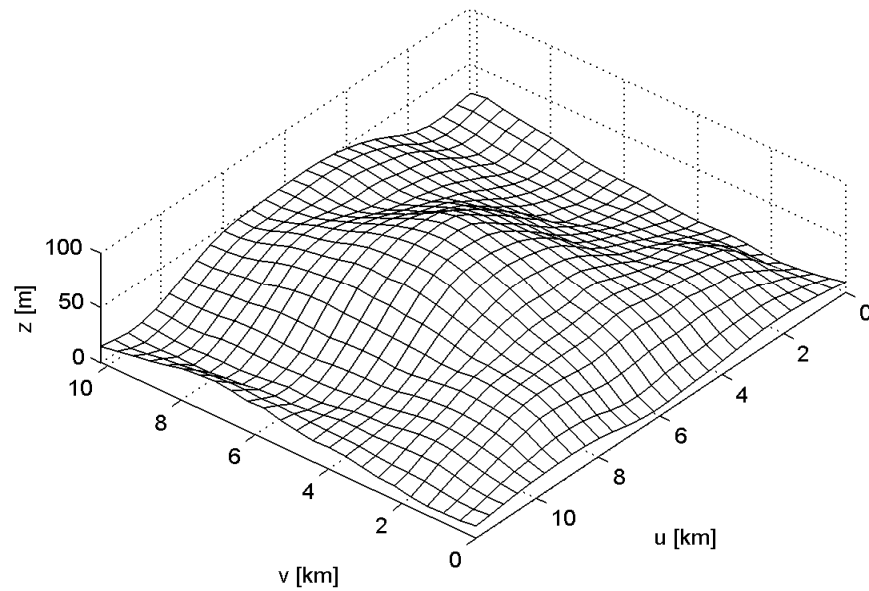*Fig. 4: Raffaello Lena on January 6, 2006,
at 18:36   UT*

*Fig. 5: Digital elevation map of the dome
located at 08.26º E and 10.52 º N*

Table 1: Properties of the dome located at 08.26º E and 10.52º N, derived from the image shown in Fig. 2.

Longitude	Latitude	Diameter [km]	Height [m]	Slope [°]	Volume [km^3]
08.26°	10.52°	9.3± 0.5	70 ± 10	0.86 ± 0.2	2.2

Table 2: Spectral and morphometric properties characterising the dome classes introduced by Wöhler et al. (2006).

Class	TiO$_2$ content	Slope [°]	D [km]	V [km^3]
A	high	0.3-1.0	5-13	<3
B$_1$	moderate	2.0-5.4	6-15	5-32
B$_2$	low to moderate	1.3-1.9	8-15	2-21
C$_1$	low to moderate	0.6-1.8	13-20	7-33
C$_2$	moderate to high	1.0-2.5	8-17	4-17
D	high	1.3-2.5	?25	40-67

Table 3: Morphometric and rheologic properties of the dome Hyginus 3 and the domes A4-A6 near Arago

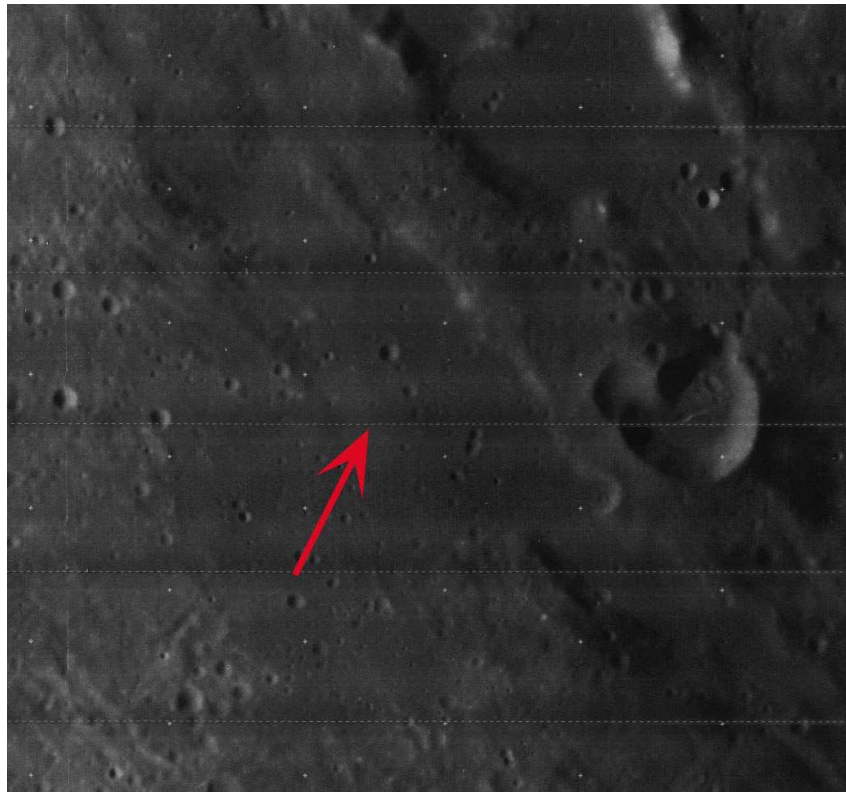| dome	Heigth [m]	Slope [°]	D [km]	V [km^3]	η [Pa s]	E [m^3 sec-1]	T [years]
Hyginus 3	70	0.86	9.3	2.2	1.2 x 10^4	218	0.32
A4	65	0.66	11.1	3.2	5.6 x 10^3	329	0.31
A5	45	0.59	8.4	1.4	1.9 x 10^3	273	0.16
A6	50	0.58	9.5	1.8	2.3 x 10^3	314	0.18

Fig.6: Lunar Orbiter frame IV-097-H2

Fig.7: Clementine 750 nm albedo: the pyroclastic deposit characterised by Gaddis et al. (2003) is marked in red, the dark and smooth terrain in green, the dome in blue, and the nearby hummocky terrain in violet
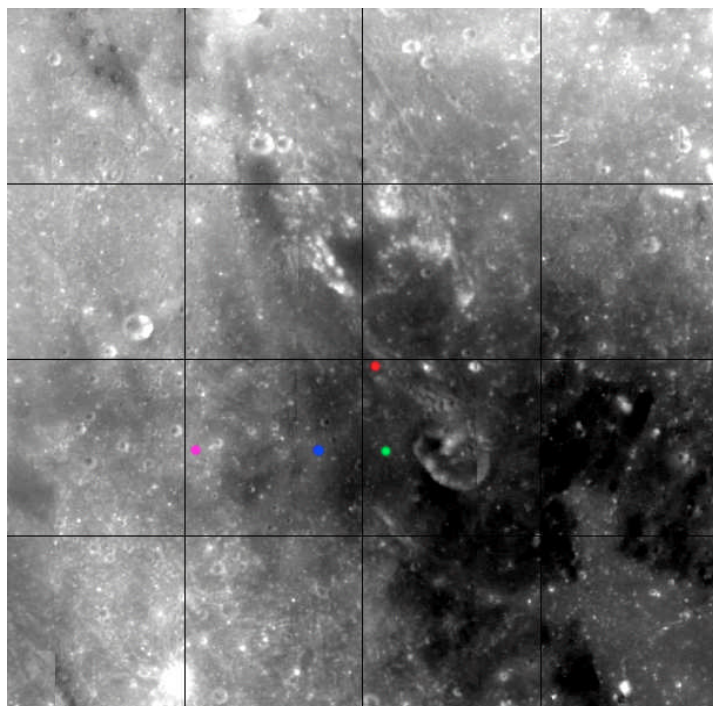
6. Results and discussion

Mare Vaporum is a volcanic region, and the volcanic activity produced flat effusive flows. The spectral appearance of the southeast region of Mare Vaporum is different from the remainder of the mare, since it displays a lower albedo. Hence, this region has presumably undergone two subsequent volcanic phases: a phase of effusive volcanism building up the volcanic edifice and a phase of eruptive volcanism generating the pyroclastic deposit.

The dome Hyginus 3, located at 08.26º E and 10.52º N, is an effusively constructed edifice with a summit crater pit. Terrestrial formations of this type produce basaltic shields, which is the form most lunar domes take. Thus, in the final states of lunar volcanism, there was a switch from extensive sheet flows to the construction of domes. Initially, lavas were very fluid due to their high temperature and massive volumes. Over time, the erupting lavas cooled, decreased in flow rate, and began to crystallize. This changed the characteristics of the lava, decreasing its fluidity so that it began to "pile up" around the effusion vent, forming a dome (Basaltic Volcanism Study Project, 1981).

In the GLR classification scheme, several classes of lunar domes are defined according to their spectral and morphometric properties (Table 2). An approximate dome classification can already be inferred from the diameter vs. flank slope diagram shown in Fig. 10, where the domes of the set examined by Wöhler et al. (2006) are labelled according to their respective class. In this diagram, however, an unambiguous class assignment cannot be obtained for all domes due to the overlap between classes B and C. In the GLR scheme, classes A-C denote morphologically simple and likely monogenetic edifices which do not show individual lava flows or other traces of several eruption events. The dome regarded in this study is of Class A. Domes of this class display small to moderate diameters between 5 and 13 km with very low flank slopes and volumes and were formed by spectrally blue lavas of high R_{415}/R_{750} spectral ratio. The inferred low lava viscosity, high effusion rate, and short duration of the effusion process are rheologic properties which are typical of class A domes.

Lunar mare domes that come close to Hyginus 3 in their morphometric and rheologic properties are a group of three aligned domes near Arago, termed A4-A6 by Wöhler et al. (2006). The domes are located north of Arago crater (marked in green in Fig. 11) with a base diameter of 11.1, 8.4, and 9.5 km, respectively, and with very low flank slopes. The morphometric and rheologic properties are reported in Table 3. Note that the dome Hyginus 3 formed from lava of somewhat higher viscosity than the domes A4-A6. The soil of the dome is spectrally bluish but probably with a lower TiO_2 content than that of the domes A4-A6.

The reflectance spectrum of the dome is intermediate between the dark and smooth mare unit to the west and that of the hummocky terrain, which is of higher reflectance. A possible explanation for this observation is that mixing of basaltic

*Fig.8:
Clementine
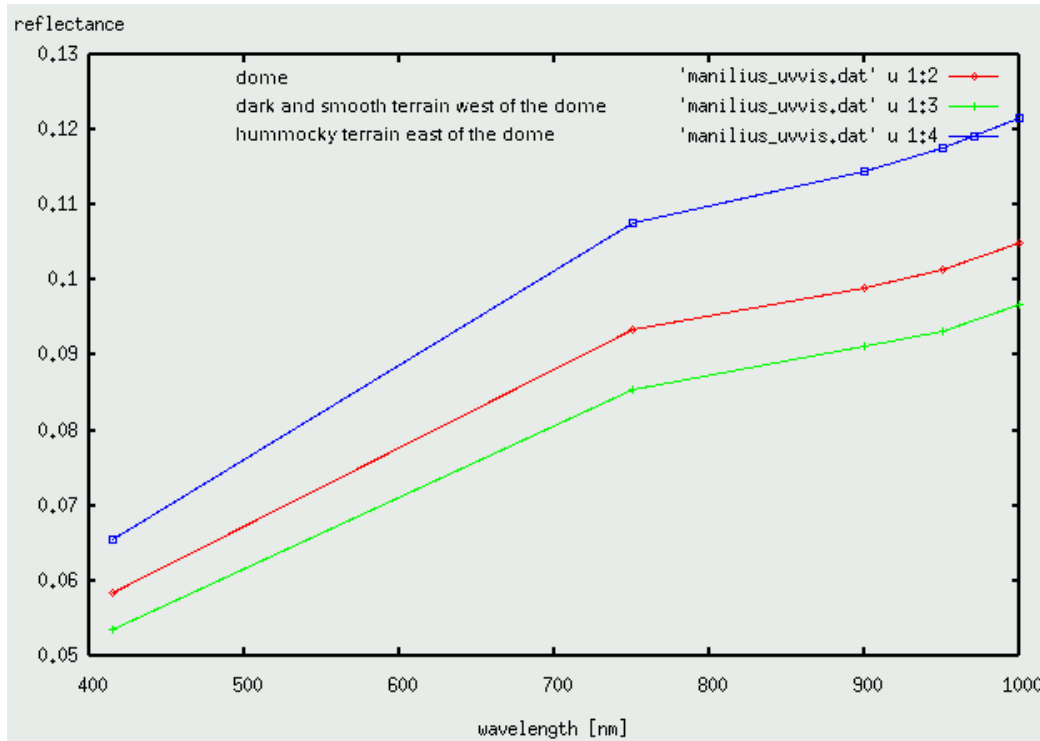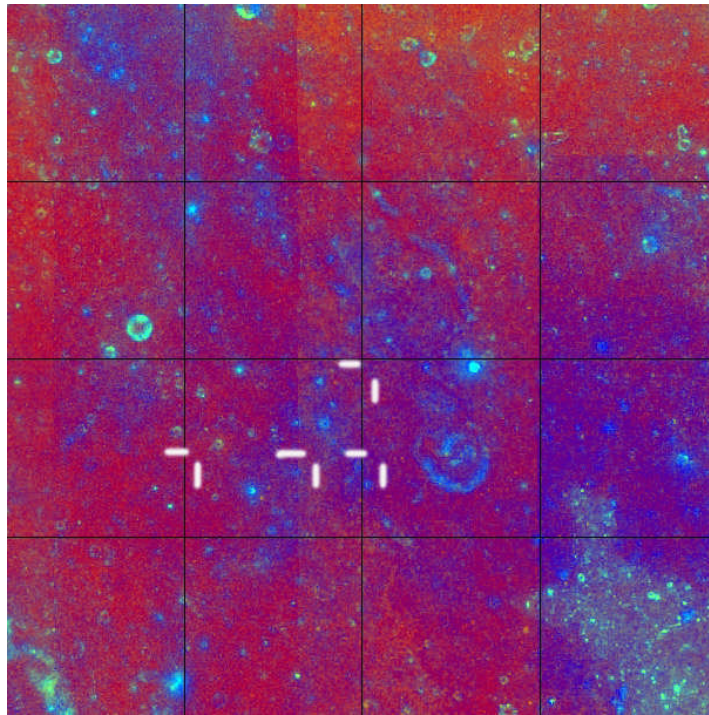UVVIS
imagery,
color ratio*

Fig. 9: Reflectance spectra for the dome examined in this study and further geologic units including the dark and smooth terrain west of dome and the nearby hummocky terrain located just to its east.

mare lava and crustal wallrock occurred. Such mixing may have taken place by assimilation of wallrock, i. e. its melting by and subsequent incorporation into the hot magma at larger depth, producing an erupting lava with intermediate spectral properties. Usually, however, assimilation is especially favoured by long durations of the eruption process (Spera, 2000), which is not the case for the dome Hyginus 3. Another possibility is mixing of the basaltic magma with loose crustal wallrock at shallow depth. Due to the presumably large rise speed of the magma, there would not have been sufficient time to melt the crustal material, but it might have been transported to the surface by the basaltic magma, leading to an intermediate spectrum as the surface manifestation of this mixing process. Apart from this kind of vertical mixing, the surface of the dome and its surrounding may also have been contaminated with highland material by lateral mixing (Li et al., 1997).

long and oriented roughly radially with respect to Mare Imbrium and is running in parallel to the Ariadaeus rille. This structure was detected in several of our images, demonstrating that it is not a processing artefact. We found that the rille-like feature can be imaged around first quarter Moon while it is not easily detected around last quarter Moon. Possibly this linear feature is a graben formed by the stress field built up by a pressurised dike that did not reach the surface but ascended through a crustal fracture to a shallow depth, a mechanism suggested by Petrycki and Wilson (1999) for narrow linear rilles like Rima Sirsalis or Rima Parry V. Future work will include an extension of our analysis to this structure.
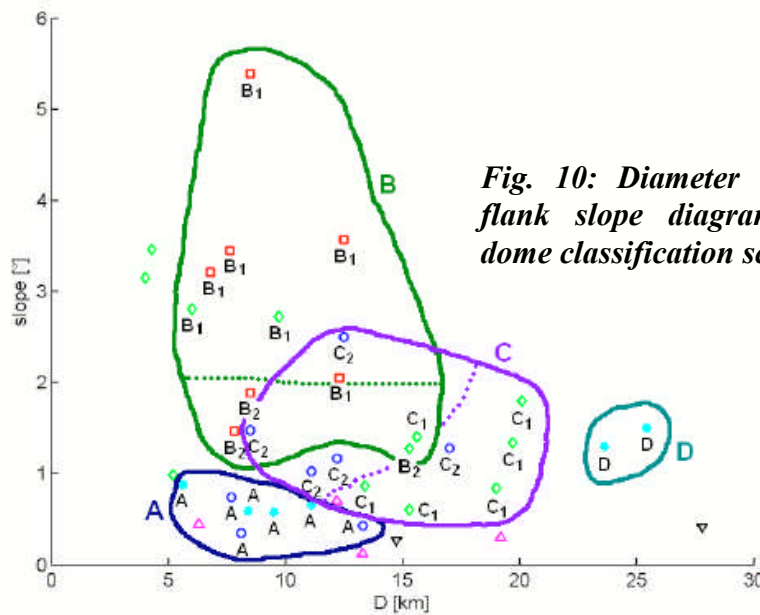

Fig. 10: Diameter versus flank slope diagram for dome classification scheme

In our images, a narrow rille-like feature is apparent just south of the crater Manilius. Clementine imagery, taken under high solar elevation angle, shows a hint of this feature, which looks like a degraded structure (Fig. 12). It is 80 km
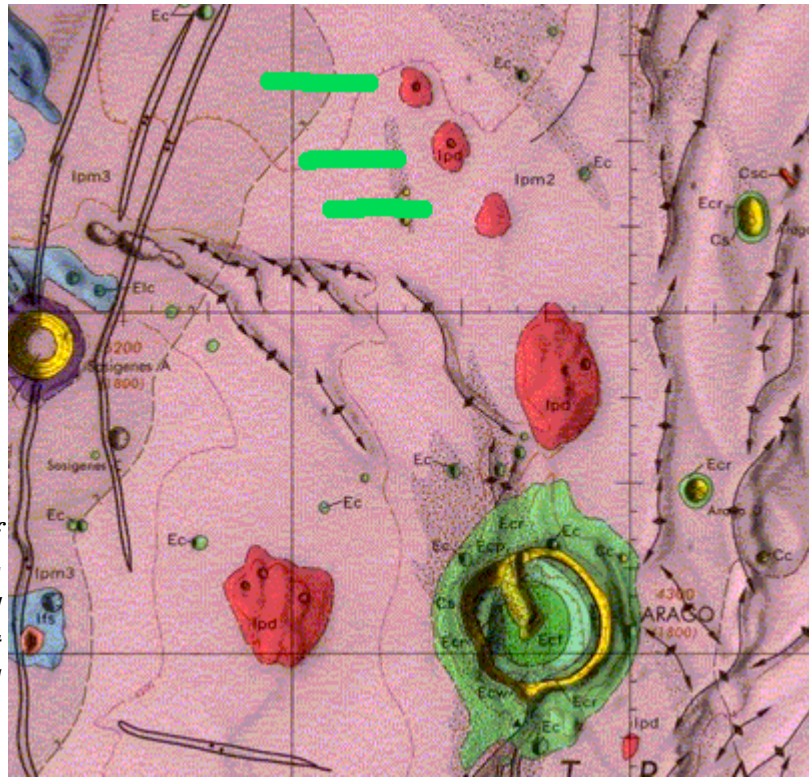
Fig. 11: Position of three aligned domes near Arago, termed A4-A6 by Wöhler et al. (2006). USGS geologic map I510
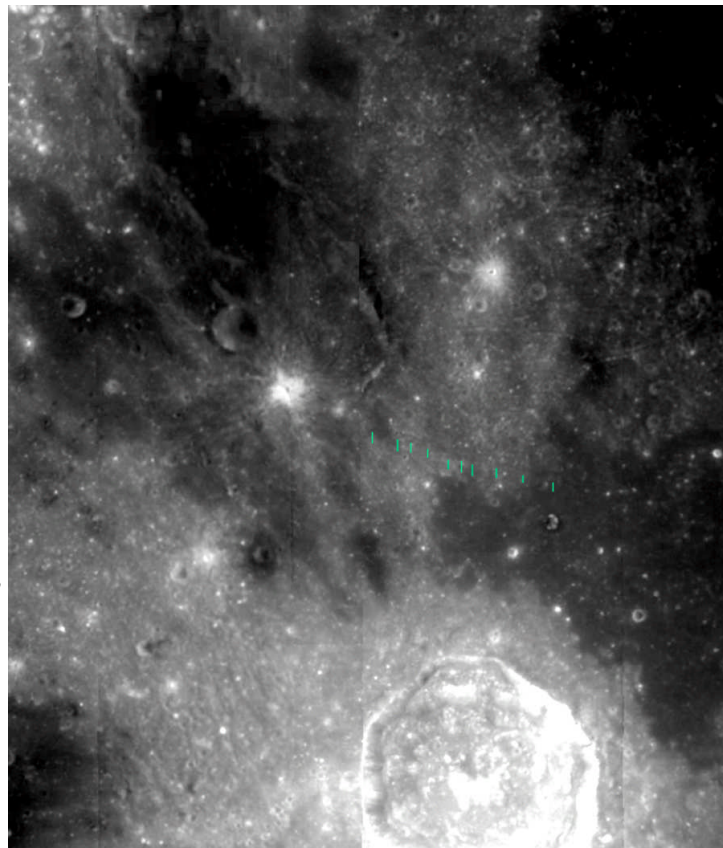

Fig. 12: Clementine imagery showing a narrow rille-like feature described in the text

References

[1] Basaltic Volcanism Study Project. *Basaltic Volcanism on the Terrestrial Planets*. Pergamon Press, Inc., New York, 1981.

[2] Charette, M. P., McCord, T. B., Pieters, C. M., Adams, J. B., Application of remote spectral reflectance measurements to lunar geology classification and determination of titanium content of lunar soils, *J. Geophys. Res.*, vol. 79, pp. 1605-1613, 1974.

[3] Eliason, E., Isbell, C., Lee, E., Becker, T., Gaddis, L., McEwen, A., Robinson, M., Mission to the Moon: the Clementine UVVIS global mosaic, *PDS Volumes USA NASA PDS CL 4001 4078,* 1999 http://pdsmaps.wr.usgs.gov

[4] Gaddis, L. R., Staid, M. I., Tyburczy, J. A., Hawke B. R., Petro, N. E., Compositional analyses of lunar pyroclastic deposits, *Icarus*, vol. 161, no. 2, pp. 262-280, 2003.

[5] Gillis, J. J., Lucey, P. G., 2005. Evidence that UVVIS ratio is not a simple linear function of TiO2 content for lunar mare basalts. *Lunar Planet. Sci. XXXVI*, abstract #2252.

[6] Head, J. W., Gifford, A., Lunar mare domes: classification and modes of origin, *The Moon and Planets* 22, 235-257, 1980.

[7] Horn B. K. P., Height and Gradient from Shading, MIT technical report, AI memo no. 1105A, 1989. http://people.csail.mit.edu/people/bkph/AIM/AIM-1105A-TEX.pdf

[8] Kapral, C., Garfinkle, R., 2005. GLR Lunar Dome catalog. http://www.glrgroup.org/domes/kapralcatalog.htm

[9] Lena, R., Douglass, E., Observations of a dome near crater Hyginus, *The Strolling Astronomer* 48(2), pp. 18-23, 2006.

[10] Lena, R., Wöhler, C., Bregante, M. T., Fattinnanzi, C., A combined morphometric and spectrophotometric study of the complex lunar volcanic region in the south of Petavius, *JRASC* 100 (1), pp. 14-25, 2006.

[11] Li, L., Mustard, J. F., He, G., 2005. Compositional gradients across mare-highland contacts: The importance of lateral mixing, Lunar Planet. Sci. XXVIII, abstract #1724.

[12] Lucey, P. G., Blewett, D. T., Hawke, B. R., Mapping the FeO and TiO_2 content of the lunar surface with multispectral imagery, *J. Geophys. Res.*, vol. 103, no. E2, pp. 3679-3699, 1998.

[13] Petrycki, J. A., Wilson, L., 1999. Volcanic Features and Age Relationships Associated with Lunar Graben. *Proc. 30th Lunar Planet. Sci. Conf.*, abstract #1335.

[14] Pike, R. J., Depth/Diameter relations of fresh lunar craters: Revision from Spacecraft Data, *Geophys. Res. Lett.*, vol. 1, pp. 291-294, 1974.

[15] Rükl, A., 1991. Atlas of the Moon. P. Hamlyn publishing, London.

[16] Spera, F. J., 2000. Physical properties of magma. In: Sigurdsson, H. (Ed.), Encyclopedia of Volcanoes. Academic Press, San Diego.

[17] Weitz, C. M, Head, J. W., Spectral properties of the Marius hills volcanic complex and implication for the formation of lunar domes and cones, *J. Geophys. Res.*, vol. 104, no. E8, pp. 18933-18956, 1999.

[18] Wilhelms, D., Geologic Map of Mare Vaporum Quadrangle of the Moon, *USGS Lunar Geologic Map I- 548,* 1968.

[19] Wilhelms, D., The geologic history of the Moon, *USGS Prof. Paper* 1348, 1987.

[20] Wilson, L., Head, J. W., Lunar Gruithuisen and Mairan domes: Rheology and mode of emplacement, *J. Geophys. Res.* 108(E2), pp 5012-5018, 2003.

[21] Wöhler, C., Lena, R., Lazzarotti, P., Phillips, J., Wirths, M., Pujic, Z., A combined spectrophotometric and morphometric study of the lunar mare dome fields near Cauchy, Arago, Hortensius, and Milichius, *Icarus*, Vol.183, 2, pp. 237-264, 2006.

TWO DOMES IN MARE FECUNDITATIS NEAR MESSIER CRATER

Raffaello Lena, Christian Wöhler, Maria Teresa Bregante, Jim Phillips, Davide Zompatori, Gerardo Sbarufatti

Geologic Lunar Research (GLR) Group

Abstract

In this study we examine Mare Fecunditatis, a lunar region poorly shown in spacecraft imagery. Morphometric details were established for two lunar domes. The first dome, named Messier 13, is located at longitude 43.47° E and latitude 1.95° S. It is a previously unreported dome with a diameter of 7.7 km. Its height was determined to 85 m with an average slope of 1.26°. We determined morphometric data of another dome, named Messier 10, located at longitude 50.42° E and latitude 2.5° S. This dome has a diameter of 8.7 x 6.4 km, a height of 80 m and an average slope of 1.12°. Rheologic modelling of the two domes suggests that they were built by lava of moderate viscosity, erupting at a moderate effusion rate over a short period of time of about seven months. According to the GLR classification scheme both domes belong to class C_2, with a tendency towards class C_1.

1. Introduction

Fecunditatis is a pre-Nectarian impact basin which was filled by ejecta material from neighbouring younger basins, Nectaris (the oldest), Crisium, and Imbrium (youngest), ranging in age from 3.7-3.5 Ga to 3.4 Ga in the late Imbrium period (Rajmon and Spudis, 2000). The Fecunditatis basalts are mostly poor in titanium, but in some regions intermediate to high titanium lava flows occur. Most of Mare Fecunditatis is filled with lavas that reach thicknesses of a few hundred metres, while in central Fecunditatis the basalts are over 1000 metres thick (Rajmon and Spudis, 2000; de Hon, 1976). The samples returned by the Luna 16 spacecraft were different in composition, including both titanium-rich and alumina-rich basalts. The high alumina basalts have radiometric ages of about 3.41 Ga (Whitford-Stark, 1986 and references therein).

The exact size and location of the impact basin that has been filled by the Fecunditatis lavas is poorly defined. Wilhelms (1984) indicates that it was centred on the northern portion of the area where the basalts infilling is thickest. Furthermore, many craters are buried by lava flows (ghost craters), while graben and long wrinkle ridges formed on the shallow surface of the basin. Also prominent in Fecunditatis is Dorsa Geikie, more than 200 km long, and Rima Goclenius, a prominent set of arcuate rilles.

In Mare Fecunditatis the crater Messier is situated. This unique crater, located at 47.6° E and 1.9° S, has a shape remarkably

Fig. 1: Clementine 750 nm albedo image of the region around Messier.

different from the usual circular one, and it is the source of two bright and conspicuous rays (cf. Clementine imagery as shown in Fig. 1). Messier is about 1250 m deep with an elongated shape. It is a double crater: the smaller and older crater was superimposed by a larger crater.

This crater and the rays were created by a very narrow angle grazing impact (1-5°) from a pair of meteoroids that were gravitationally bound (Wilhelms, 1987). The main impact projectile created Messier, another part of the projectile Messier A and the rays. On the basis of the asymmetric crater shapes and ejecta patterns it has been concluded that these lunar craters were produced by a projectile

travelling at a high estimated speed of 1.7 km/s from the east to west. Furthermore, the elongated shape and the unusual ejecta pattern has been reproduced in laboratory impact simulations by Gault and Wedekind (1978).

Mare Fecunditatis is a lunar region poorly shown in Lunar Orbiter and other spacecraft imagery. The lunar domes are not easy to image from the Earth as the mare is close to the lunar limb. In this study we will describe a previously unreported dome located at 43.47° E and 1.95° S. It has been added under the name "Messier 13" to the revised catalogue of lunar domes by Kapral and Garfinkle (2005). Furthermore, we perform a detailed examination of another shallow dome, first reported by Wood (2004) and also by Braga (2005), located at 50.42° E and 2.5° S and here denoted by "Messier 10" according to the catalogue of Kapral and Garfinkle (2005). Several further dome-like features are located near Messier crater. They could be very gentle intrusive swells or shallow domes, but a different origin cannot be excluded at this stage of our survey.

We will examine the morphometric characteristics of the two domes by making use of a combined photoclinometry and shape from shading approach described by Wöhler et al. (2006) and by Lena et al. (2006). The obtained values are utilised to derive information about the physical parameters of dome formation (lava viscosity, effusion rate, duration of the effusion process), employing the rheologic model by Wilson and Head (2003). We provide a geological interpretation of our spectrophotometric,

morphometric, and rheologic modelling results, comparing them to the corresponding parameters typically observed for lunar mare domes.

2. Observations

For each of the observations, the local solar altitude (Alt.) and the Sun's selenographic colongitude (Col.) were calculated using the Lunar Observer's Toolkit by H. D. Jamieson. All images are oriented with north up and east (IAU) to the right. The dome Messier 13, located at 43.47° E and 1.95° S, was imaged by J. Phillips on May 02, 2006, at 01:04 UT (Alt. 1.40°, Col. 317.96°), using a 200 mm TMB apochromatic refractor and an Atik B&W camera (Fig. 2). Another image (Fig. 3) was taken by D. Zompatori on September 11, 2006, at 00:50 UT using a Schmidt-Cassegrain 280 mm f/20 and a DMK31AF03 CCD camera (Alt. 6.33°, Col. 130.18°). The diameter of the dome Messier 13, corrected for foreshortening, is 7.7 ± 0.3 km.

The image shown in Fig. 4 displays another shallow dome located to the east of Messier pair at 50.42° E and 2.5° S, named Messier 10. This image was made by G. Sbarufatti on October 02, 2004, at 00:07 UT (Alt. 2.81°, Col. 126.74°) using

Fig. 2: Dome Messier 13 as imaged by J. Phillips on May 02, 2006, at 01:04 UT.

a Schmidt-Cassegrain 200 mm f/10 and a Vesta Pro webcam. The dome, situated at the inner rim of an unnamed ghost crater, shows a summit crater pit. Another image (Fig. 5) was taken by C. Wöhler on October 10, 2006, at 01:49 UT (Alt. 5.21°, Col. 124.39°) using a 200 mm Newtonian reflector and a Lumenera LU75M CCD camera. Fig. 6 was taken by G. Sbarufatti at the same UT date and time using a Schmidt-Cassegrain 200 mm f/10 and a KamPro02 CCD camera. Regarding the images of Figs. 4-6, the dome diameter is 8.7 x 6.4 km (where the

accuracy amounts to ± 0.4 km).

3. Morphologic, morphometric, and spectral properties

The height values for the two domes as reported in Table 1 were derived by a combined photoclinometry and shape from shading analysis (Horn, 1989; Wöhler et al, 2006; Lena et al., 2006, and references therein). The resulting digital elevation maps (DEMs) are shown in Fig. 7. Based on the image shown in Fig. 2, the height of dome Messier 13 was determined to 85 ± 10 m, resulting in an average slope of $1.26° \pm 0.10°$. The height of the dome Messier 10 located at $50.42°$ E and $2.5°$ S shown in Figs. 5 and 6 was determined to 80 ± 10 m and 85 ± 10 m, respectively, yielding a slope of $1.12° \pm 0.10°$.

The dome volume V was computed by integrating the reconstructed 3D profile over an area corresponding to a circular region of diameter D around the dome summit. A rough quantitative measure for the shape of the dome is given by the form factor $f = V/[\pi h(D/2)^2]$, where we have $f = 1/3$ for domes of conical shape, $f = 1/2$ for parabolic shape, $f = 1$ for cylindrical shape, and intermediate values for hemispherical shape. For the domes examined in this study, we thus obtain an edifice volume of 4.1 km³ ($f = 0.54$) and 2.8 km³ ($f = 0.66$) for Messier 13 and Messier 10, respectively.

We furthermore determined a UVVIS five-band spectrum of the dome based on Clementine imagery. The Clementine UVVIS multispectral image data were obtained the wavelengths 415, 750, 900, 950, and 1000 nm. The reflectance values were derived relying on the calibrated and normalised Clementine UVVIS reflectance data as provided by Eliason et al. (1999). The extracted Clementine UVVIS data were examined in terms of 750 nm reflectance (albedo) and the R_{415}/R_{750} and R_{950}/R_{750} colour ratios. Albedo at 750 nm is an indicator of variations in soil composition, maturity, particle size, and viewing geometry. The R_{415}/R_{750} colour ratio essentially is a measure for the TiO_2 content of mature basaltic soils, where high R_{415}/R_{750} ratios correspond to high TiO_2 content and vice versa (Charette et al. 1974). However, for many lunar regions the relation between R_{415}/R_{750} ratio and TiO_2 content displays a significant scatter (Gillis and Lucey, 2005). The R_{950}/R_{750} colour ratio is related to the strength of the mafic absorption band, representing a measure for the FeO content of the soil, and is also sensitive to the optical maturity of mare and highland materials (Lucey et al. 1998).

The Clementine UVVIS spectral data reported in Table 2 reveal for the dome Messier 13 a 750 nm reflectance of $R_{750} = 0.1047$, a moderate value for the UV/VIS colour ratio of $R_{415}/R_{750} = 0.6007$, indicating a moderate TiO_2 content, and a weak mafic absorption with $R_{950}/R_{750} = 1.0458$ suggesting a high soil maturity. The Clementine UVVIS spectral data reveal similar spectral properties for the dome Messier 10 with a 750 nm reflectance of $R_{750} = 0.1004$, a moderate value for the UV/VIS colour ratio of $R_{415}/R_{750} = 0.6138$, indicating a moderate TiO_2 content, and a weak mafic absorption with $R_{950}/R_{750} = 1.0404$.
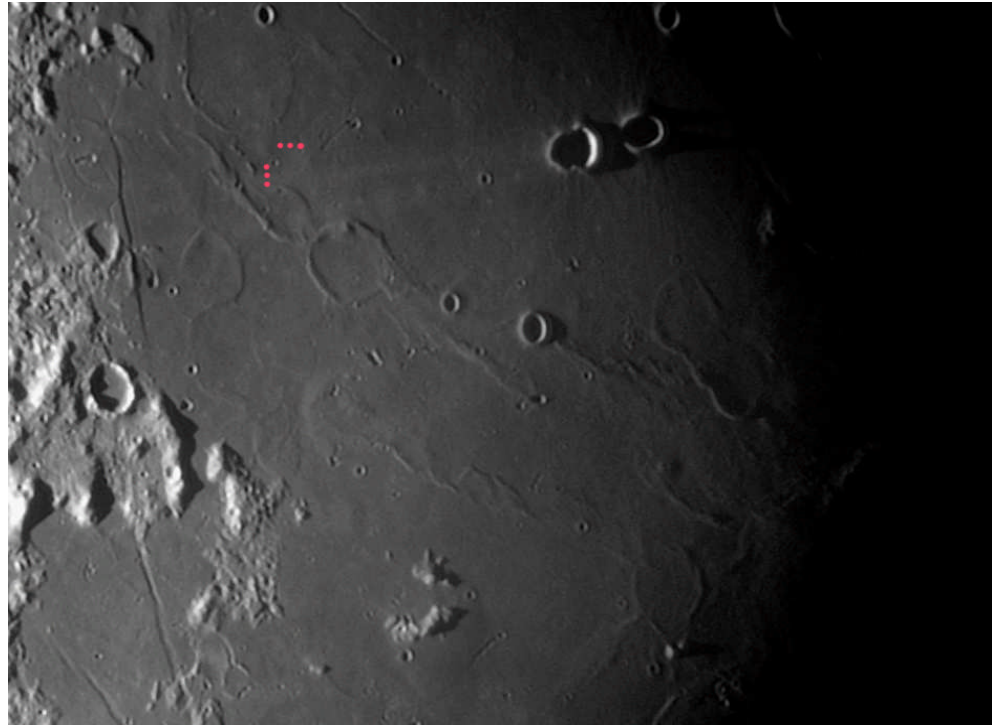
Fig. 3:

Dome Messier 13 as imaged by D. Zompatori on September 11, 2006, at 00:50 UT.

Fig. 4: Dome Messier 10. Image taken by G. Sbarufatti on October 02, 2004, at 00:07 UT.

Table 1: Morphometric and rheologic properties of the domes examined in this study.

dome	Heigth [m]	Slope [°]	D [km]	V [km³]	η [Pa s]	E [m³ sec⁻¹]	T [years]
Messier 13	85	1.26	7.7	4.1	4.9×10^4	122	0.55
Messier 10	80	1.12	8.7 x 6.4	2.8	3.1×10^4	148	0.60

Table 2: Spectral properties of the domes examined in this study.

dome	R_{750}	$R_{415/750}$	$R_{950/750}$
Messier 13	0.1047	0.6007	1.0458
Messier 10	0.1004	0.6138	1.0404

Table 3: Approximate spectral and morphometric properties characterising the dome classes A-D introduced by Wöhler et al (2006).

Class	TiO_2 content	R_{415}/R_{750}	Slope [°]	D [km]	V [km³]
A	high	> 0.64	0.3-1.0	5-13	< 3
B_1	moderate	0.55-0.64	2.0-5.4	6-15	5-32
B_2	low to moderate	0.55-0.64	1.3-1.9	8-15	2-21
C_1	low to moderate	0.55-0.60	0.6-1.8	13-20	7-33
C_2	moderate to high	0.60-0.64	1.0-2.5	8-17	4-17
D	high	> 0.64	1.3-2.5	? 25	40-67
G	low to moderate	0.55-0.60	> 6.0	7-30	20-390

4. Rheologic modelling

We assume that the examined domes were formed by extrusion of magma onto a flat plane spreading in all directions from the vent, in contrast to lava flows resulting from lava extrusion onto an inclined surface. Wilson and Head (2003) provide a quantitative treatment of such dome-forming eruptions. This model estimates the yield strength τ, i. e. the pressure or stress that must be exceeded for the lava to flow, the plastic viscosity η, yielding a measure for the fluidity of the erupted lava, the effusion rate E, i. e. the lava volume erupted per second, and the duration $T = V/E$ of the effusion process. This model is applied to a large set of representative lunar mare domes by Wöhler et al. (2006). It relies on the morphometric dome properties (diameter, height, volume) and several physical constants such as the lava density, the acceleration due to gravity, and the thermal diffusivity of the lava. The rheologic model by Wilson and Head (2003) yields for the domes Messier 13 and Messier 10 an effusion rate of 122 and 148 m^3/s, respectively.

They were formed from lava of moderate viscosities of 4.9×10^4 and 3.1×10^4 Pa s over a period of time of 0.55 and 0.60 years (about seven months).

5. Results and discussion

The earliest lavas erupted during the "main phase" of mare volcanism were the high titanium basalts of Maria Tranquillititas and Serenitatis (basalts returned from the Apollo 11 and 17 missions, respectively), characterised by ages between 3.8 and 3.6 Ga. Lower titanium basalts erupted between about 3.6 and 3.1 Ga in Mare Crisium and Fecunditatis (Luna 16 and 24 sample-return missions), 3.3 Ga in Mare Imbrium (Apollo 15), and 3.1 Ga in Oceanus Procellarum (Apollo 12). The Fecuditatis basin formed in the Pre-Nectarian epoch, while the basin material surrounding the mare is of the Nectarian epoch.

The mare material is of the late Imbrian epoch and is relatively thin compared to Mare Crisium or Mare Tranquillitatis (Rajmon and Spudis, 2000). Like Mare Tranquillitatis, Mare Fecunditatis occupies a large fraction of the basin diameter but is relatively thin and an intense volcanic activity occurred, and domes were formed during the last phases of volcanic eruptions.

Lunar domes are formed either by outpouring of magma from a central vent or by a subsurface accumulation of magma that causes an up-doming of the bedrock layers, creating a smooth, gently sloping positive relief. Domes representing volcanic sources are smooth surfaced and usually have a summit crater pit. Most vents related to domes appear to be associated with surrounding lava plains of known volcanic origin or in association with pyroclastic deposits (Head and Gifford, 1980). Several patches of dark material are visible to the northwest shores of Fecunditais, and some of these dark regions have been characterised as lunar

Fig. 5: Dome Messier 10. Image taken by C. Wöhler on October 10, 2006, at 01:49 UT

pyroclastic deposits by Gaddis et al (2003), named Taruntius and Taruntius NW.

However, recent impact events (e. g. Langrenus, Taruntius, and Messier craters) affected the surface of Mare Fecunditatis, redistributing surface materials over a large area, thereby obscuring the nature of the underlying basaltic terrain (Whitford-Stark, 1986). Clementine UVVIS imagery reveals that the two domes examined in this study, like the surrounding mare, formed in basalts of moderate TiO_2 content.

For a set of 38 effusive lunar mare domes, Wöhler et al. (2006) examined four important fields of lunar mare domes in terms of the spectral properties and 3D shapes of the volcanic edifices and developed a classification scheme. An approximate dome classification can already be inferred from Table 3, outlining the spectral and morphometric properties of each dome class. Both domes, which are similar to each other with respect to their morphometric, rheologic, and spectral properties, belong to class C_2, with a tendency towards class C_1 due to their somewhat moderate R_{415}/R_{750} value.

According to the GLR classification scheme, class C domes have diameters between 8 and 20 km, with relatively low flank slopes typically below 2°. Domes formed from spectrally red lavas of low to moderate $R_{415/750}$ ratio with large diameters between 13 and 20 km and large edifice volumes of several tens of km^3 are assigned to subclass C_1, while spectrally bluer domes of moderate to high $R_{415/750}$ ratio, smaller diameters between 8 and 13 km, and lower edifice volumes are assigned to subclass C_2. The two domes examined in this study, located at the western and eastern shores of Mare Fecunditatis, display similar morphometric properties and rheologic modelling results and were formed by lavas of moderate titanium content. Future work will include an extension of our analysis to other possible effusive mare domes in Mare Fecunditatis.

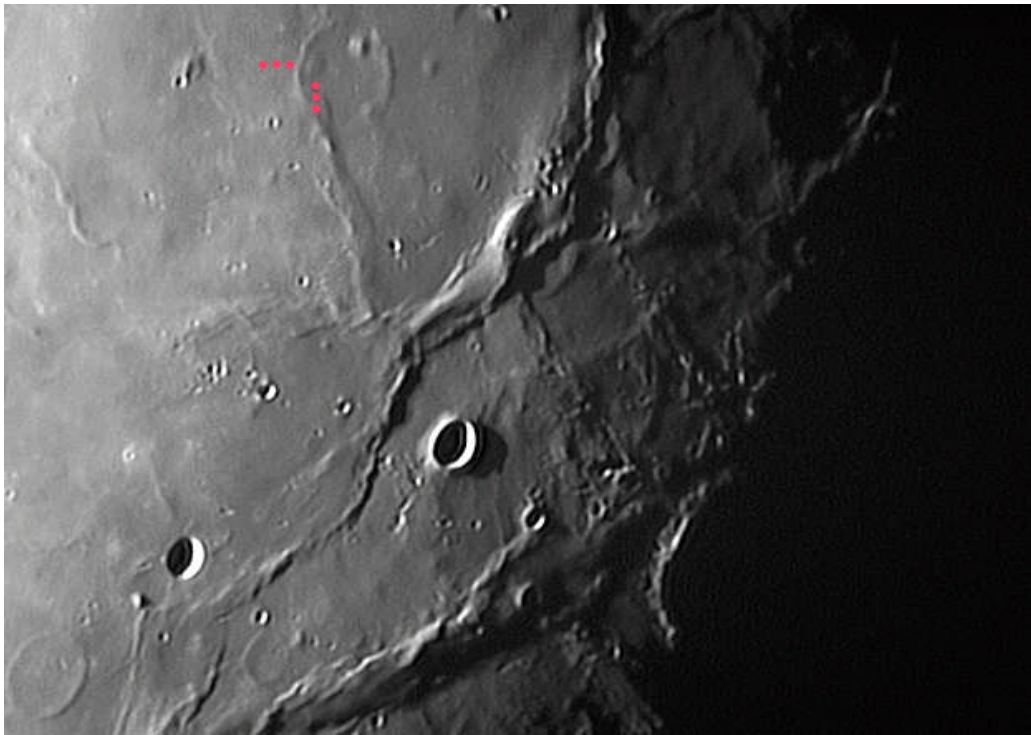*Fig. 6: Dome Messier 10. Image taken by G. Sbarufatti on October 10, 2006, at 01:43 UT.*
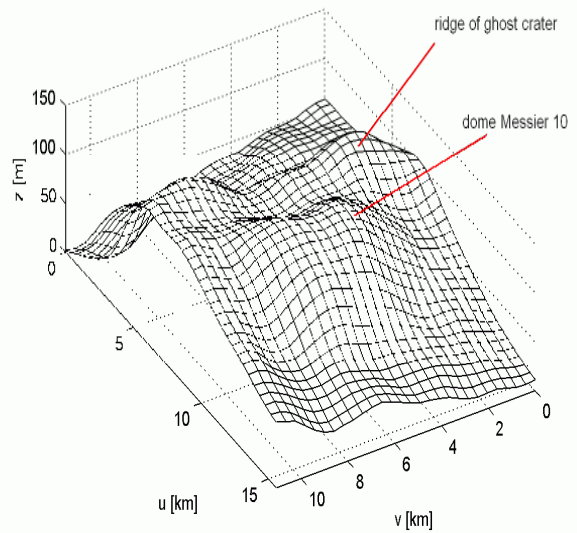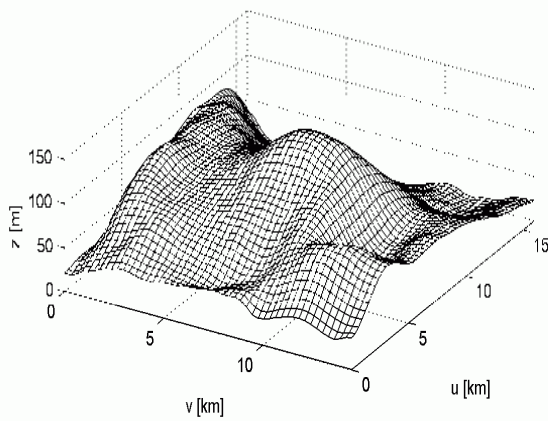
Fig. 7: Left: DEM of Messier 13, obtained based on the image shown in Fig. 2, viewed from south-western direction. Right: DEM of Messier 10, obtained based on the image shown in Fig. 5, viewed from south-eastern direction. The dome is apparent in the foreground, situated in the immediate vicinity of the ridge-like ghost crater rim west of it.

References

[1] Braga, R., Domes in Mare Fecunditatis, The Lunar Observer, April 2005, pp. 4-5.

[2] Charette, M. P., McCord, T. B., Pieters, C. M., Adams, J. B., Application of remote spectral reflectance measurements to lunar geology classification and determination of titanium content of lunar soils, *J. Geophys. Res.*, vol. 79, pp. 1605-1613, 1974.

[3] De Hon, R.A, Waskom, J. L., *Proc. Lunar Sci. Conference VII*, pp. 2729-2746, 1976.

[4] Eliason, E., Isbell, C., Lee, E., Becker, T., Gaddis, L., McEwen, A., Robinson, M., Mission to the Moon: the Clementine UVVIS global mosaic, *PDS Volumes USA NASA PDS CL 4001 4078,* 1999 http://pdsmaps.wr.usgs.gov

[5] Gaddis, L. R., Staid, M. I., Tyburczy, J. A., Hawke B. R., Petro, N. E., Compositional analyses of lunar pyroclastic deposits, *Icarus*, vol. 161, no. 2, pp. 262-280, 2003.

[6] Gault, D. E., Wedekind, J. A., 1978. Experimental studies of oblique impact. *Lunar Planet. Sci. IX*, pp. 3843-3875.

[7] Gillis, J. J., Lucey, P. G., 2005. Evidence that UVVIS ratio is not a simple linear function of TiO2 content for lunar mare basalts. *Lunar Planet. Sci. XXXVI*, abstract #2252.

[8] Head, J. W., Gifford, A., Lunar mare domes: classification and modes of origin, *The Moon and Planets* 22, 235-257, 1980.

[9] Horn, B. K. P., Height and Gradient from Shading, MIT technical report, AI memo no. 1105A, 1989. http://people.csail.mit.edu/people/bkph/AIM/AIM-1105A-TEX.pdf

[10] Kapral, C., Garfinkle, R., 2005. GLR Lunar Dome catalog.

http://www.glrgroup.org/domes/kapralcatalog.htm

[11] Lena, R., Wöhler, C., Bregante, M. T., Fattinnanzi, C., A combined morphometric and spectrophotometric study of the complex lunar volcanic region in the south of Petavius, *JRASC* 100 (1), pp. 14-25, 2006.

[12] Lucey, P. G., Blewett, D. T., Hawke, B. R., Mapping the FeO and TiO_2 content of the lunar surface with multispectral imagery, *J. Geophys. Res.*, vol. 103, no. E2, pp. 3679-3699, 1998.

[13] Rajmon, D., Spudis, P., 2000. Geology and Stratigraphy of Mare Fecunditatis, *Lunar Planet. Sci. XXI*, abstract # 1913.

[14] Whitford-Stark, J. L., The Geology of the Lunar Mare Fecunditatis, 1986, *LPI XVII*, pp. 940-941.

[15] Wilhelms, D., The geology of the terrestrial planets, NASA SP-469, pp. 107-205, 1984.

[16] Wilhelms, D., The geologic history of the Moon, *USGS Prof. Paper* 1348, 1987.

[17] Wilson, L., Head, J. W., Lunar Gruithuisen and Mairan domes: Rheology and mode of emplacement, *J. Geophys. Res.* 108(E2), pp 5012-5018, 2003.

[18] Wöhler, C., Lena, R., Lazzarotti, P., Phillips, J., Wirths, M., Pujic, Z., A combined spectrophotometric and morphometric study of the lunar mare dome fields near Cauchy, Arago, Hortensius, and Milichius, *Icarus*, Vol.183, 2, pp. 237-264, 2006.

[19] Wood, C.A. 2004, Lunar Photo of the Day, October 11, 2004,

www.lpod.org/LPOD-2004-10-11.htm

EXPLORING FALSE COLOR AND RATIO IMAGES USING CLEMENTINE UVVIS/NIR DATA

By Richard Evans

Geologic Lunar Research (GLR) group

This paper demonstrates a methodology that amateur astronomers can use to create false color and ratio images of lunar features. These images, which are used to understand lunar geology and mineral composition, are based on image sets taken at particular wavelengths. The most commonly used being 415 nm, 750 nm, 900 nm, 950 nm and 1000 nm. These image sets can be created using broadband filters with amateur instruments or they can be created from the Clementine UVVIS image archive. The methodology is essentially the same for both types of image sets. However, in order to be useful for both qualitative and quantitative work, raw image sets must be calibrated. Specifics on the calibration of Clementine UVVIS images are beyond the scope of this paper but are discussed in detail in Malaret, E. et al. 1999.This paper compares results obtained with calibrated UVVIS Clementine image sets available from the USGS with results obtained from raw uncalibrated Clementine image obtained from raw uncalibrated Clementine image sets. The goal of this comparison was to determine whether any useful geologic information could be obtained from an uncalibrated data set. In addition to the UVVIS image sets, near infrared (NIR)wavelengths also provide useful geologic information. The 1500 nm and 2000 nm wavelengths that that are part of the Clementine data are particularly useful in discrimination between pyroxenes and olivines. Unfortunately, calibrated NIR images for these wavelengths are not yet generally accessible. By learning to create false color and ratio images, amateur astronomers can explore the geology of any part of the moon that interests them. It is hoped that this paper will provide a basic understanding of the methodology involved in the creation and interpretation of these images. Calibration of amateur telescope broadband lunar images and creating of false color and ratio images using them will be discussed in a follow-up. paper.

I. Brief Primer on Lunar Geology

Ninety-Eight percent of the lunar crust (excluding glasses) is composed of just four minerals: plagioclase feldspar, pyroxene, olivine and ilmenite. The lunar crust appears to have arisen from a stratified global magma ocean in which light weight felsic minerals (plagioclase

feldspar) floated on top of the heavier mafic minerals (Wieczorek et al., 2006). After solidification of the crust, basin forming impacts created vast depressions and fractured the underlying crust. Perhaps hundreds of millions of years after the basins formed, radioactive heating led to oooutpouring of mafic basalt forming the lunar maria. The lunar highlands are composed of 70-99% plagioclase feldspar with by far the most common mineral being anorthosite (plagioclase feldspar). Crater impacts caused deeper crust materials to rebound to the surface within central peaks and crater rims. Minerals present in these features often contain mixtures of plagioclase feldspar and mafic components (Pieters and Englert, 1993; Tompkins 2000). Examples of rocks with these minerals include noritic anorthosite, anorthositic gabbro, troctolitic anorthosite, norite, gabbro, troctolite, and dunite (Heicken et al., 1991). All of these contain plagioclase feldspar but they are differentiated by their mafic components. Norite contains orthopyroxene (low in calcium). Gabbro contains clinopyroxene (higher in calcium). Troctolite contains some olivine while dunite is composed primarily of olivine.

The lunar maria are composed of heavier and darker basalts rich in such mafic components as pyroxenes (with clinopyroxene predominating in the maria while orthopyroxene predominates in highland mafic rocks), olivine and ilmenite ($FeTiO_3$). Basalts can be classified as low titanium, high titanium and iron rich. High titanium basalts were deposited between 3.85 and 3.55 billion years ago while low titanium basalts were deposited 3.45 to 3.15 billion years ago. In composite ratio images based on 415, 750 and 1000 nm, the iron rich basalts have a strong absorption signal at 1000 nm and appear greenish. Low titanium basalts appear purplish blue while high titanium basalts like ilmenite basalts appear lighter blue due to titanium absorption at 415 nm. Titanium rich areas of the mare appear more blue and titanium poor areas appear more red in maturation ratio images (Pieters and Englert, 1993). These mafic components are mixed with plagioclase. They can be subtyped as being rich or poor in calcium, titanium and aluminum. Ilmenite contains iron but is rich in a titanium oxide. Older lunar features such as the lunar highlands have been exposed to micrometeorite bombardment for eons and have what is termed a "mature" surface soil containing glasses. This mature soil produces the distinctive red orange appearance on ratio images taken at 415, 750 and 1000 nm as described above. Micrometeorite bombardment also converts the iron in lunar soils to the Fe+2 state which absorbs at 1000 nm. However, mature highland soils, being rich in anorthosite, contain less than 5% iron and do not show significant absorption at this wavelength. However, other mature lunar soils that do have a significant mafic component (i.e. which contain in excess of 5% iron) may show stronger absorption at 1000 nm than would otherwise be expected because of the effects of prolonged micrometeorite bombardment which tends to increases the amount of Fe+2 present.

II. Introduction

The Clementine probe took millions of

lunar images between February and May of 1994. Of the cameras used, the UVVIS camera provided image sets at 415, 750, 900, 950 and 1000 nm that are particularly useful in the creation of false color and ratio images of geologic significance. It took nearly 5 years for this data set to be fully calibrated (Malaret et al., 1999). However, fortunately, fully calibrated and co-registered Clementine UVVIS 5 band (415, 750, 900, 950, and 1000 nm) images are now available for public use at the USGS PDSMAPS website (see http://pdsmaps.wr.usgs.gov/PDS/public/explorer/html/moonpick.htm).

In addition, raw uncalibrated Clementine data is also available from the National Space Science Data Center (see http://nssdc.gsfc.nasa.gov/nssdc/obtaining_data.html) in the form of a set of CD-ROM disks. The disks archive the raw UVVIS images by lunar orbital revolution number, the imaging wavelength and the lunar longitude and latitude of the feature imaged. Images are stored in a compressed format and are converted to tif format using a DOS utility program (clemdcmp.exe) which is provided. It must be noted here, however, that the raw uncalibrated Clementine data used to produce ratio images in this paper are suitable only for qualitative work in studying mineral compositions. They are not at all suitable for quantitative work in this area and ratio images made from them here are intended only for purposes of comparison with results obtained from fully calibrated images. The channels of ratio and false color images created from raw Clementine images used in this paper were balanced according to the methodology outlined in Appendix 2.

False Color and Ratio Images

Creation of false color images by assignment of a single wavelength to a particular color channel can provide some useful geologic information about the iron and titanium content of the surface (Flor et al., 2003; Gillis et al., 2004; Goguere et al., 2000). Iron preferentially absorbs at 1000 nm while titanium absorbs at 415 nm (Lucey et al., 1998; Lucey et al,1995). However, it is usually more informative to assign ratio images to color channels since this has the effect of reducing the effects of albedo and (depending on the ratios selected) providing information on mafic composition. Ratio images are created by dividing the pixel values of an image taken at one wavelength by those of a second co-registered image taken at a different wavelength. Assigning different ratio images to the red, green and blue color channels of a single image produces a single combined ratio image.

Combined ratio images created from an image set taken at 415, 750 and 1000 nm provides basic information on lunar surface maturation and limited information about mafic composition (Tompkins et al., 2000; Spudis et al., 1994). Maturation refers to a soil that has sat on the lunar surface long enough for space weathering to coat it with impact glass. Determining maturity allows identification of lunar soils that are relatively young or old. Mafic minerals are iron, magnesium, and titanium. Determining their abundances allows lunar lavas to be classified.

To create a standard ratio image the 750/415 nm ratio image is assigned to the red channel. The 750/1000 nm ratio

image is assigned to the green channel and the 415/750 nm ratio image is assigned to the blue channel. I will refer to this composite ratio image as a **maturation ratio image**. When the RGB image is viewed, mature highland soils (those that are old) appear red or orange due to the high glass content that results from eons of micrometeorite bombardment. Surfaces low in titanium also have a reddish color and pyroclastic orange glass deposits have a very deep red color (Gaddis et al., 2003). Freshly excavated lunar features appear blue as do mare surfaces having a high titanium content (ilmenite rich). Mafic components, typically rich in iron, absorb at 1000 nm and appear yellowish green (due to mixture of the reddish orange of mature soil with the green characteristic of mafic absorption) or deep indigo blue (titanium poor basalt). Mature mare soils appear reddish or purplish while freshly exposed mare surfaces appear yellowish. The basalts of the maria give the strongest signals, but weaker mafic components in certain highland features can also give a response. Yellow color often indicate freshly excavated basalt features, especially when found in crater and rille walls. Bright blue signals indicate a freshly exposed non-mafic terrain (i.e. such as freshly exposed anorthosite, a common rock of the lunar highlands).

Combined image ratios created from 415, 900, 950 and 1000 nm images provide additional information on surface mafic constituents. A mafic ratio image is constructed by assigning 750/900 nm to the red channel, 750/1000 nm to the green channel and 750/950 to the blue channel (Tompkins et al., 2000). Using this scheme low calcium pyroxenes (orthopyroxenes as in norite or noritic anorthosite) appear reddish. Olivines (as in dunite, troctolitic anorthosite, and troctolite) appear brighter green, and high calcium pyroxenes (clinopyroxenes like gabbro or anorthositic gabbro) appear bright blue. Anorthosite doesn't absorb and appears dull grayish blue to dull greyish green which can be compared geographically to its blue appearance on ratio images taken at 415, 750 and 1000 nm (see above). This response is useful in subtyping mare basalts and also for detecting and subtyping the weaker mafic constituents found in pyroxene bearing plagioclase in the lunar highlands. In addition, comparison of an albedo image with a single ratio image taken at 750/1000 nm can assist in differentiating anorthositic features from other high albedo features such as recently formed craters and their ejecta.

III. Methodology

Preparation of the Maturation Ratio Image

If raw uncalibrated data is used, then a three image set (i.e. the 415, 750 and 100 nm images) of a selected lunar feature is identified and converted to 8 bit tif format using clemdcmp.exe (provided with the raw images). The image files must then be co-registered (i.e. aligned to each other). I use a Windows based freeware program, Blink Comparator for image co-registration (see www.crysania.co.uk/trefach/trefach.pl).

Calibrated image band sets available from the USGS have already been co-aligned

and can be downloaded in many file formats. False color composites are created by copying each image to a particular channel in a blank color photograph. Typical channel assignments include 1) red=750 nm, green=1000 nm, blue=415 nm; and 2) red=1000 nm green=900 nm, blue=415 nm. The channels are then balanced for brightness and contrast.

Creation of composite ratio images is slightly more complex. The 750 nm image is divided by the 415 nm image using software designed for this purpose. I use a Windows based freeware program, Image Arithmetic (see www.t3i.nl). Similarly, the 750 nm image is divided by the 1000 nm image and the 415 nm image is divided by the 750 nm image. This process creates three separate ratio image files: 750/415 nm, 750/1000 nm and 415/750 nm. These files are then respectively assigned to the red, green and blue channels of a blank color image. The channels are then balanced for brightness and contrast.

Preparation of the Mafic Ratio Image

Using the same techniques as described for **maturation ratio image** creation above, a combined **mafic ratio image** is created in which the channel assignments are: red=750/900 nm, green=750/1000 nm and blue=750/950 nm. Creative individuals can also try combining single wavelength channel assignments with ratio image assignments. One scheme of this nature that is sometimes used has the following channel assignments: red=750 nm, green=950/750 nm, and blue=415/750 nm.

IV Example: False Color and Ratio Image Study of Tycho Central Peaks.   Results Obtained from Fully Calibrated Clementine UVVIS Images:

Clementine UVVIS calibrated images of the Tycho central peak area for five wavelength bands were downloaded from the USGS PDSMAPS server in 8 bit jpg format. Although 16 bit tiff format could be used, freeware is not presently available to perform pixel divisions using these images. The bands are downloaded as co-aligned channels. Images at 415, 750, 900, 950 and 1000 nm were obtained for creation of ratio and false color images using the methodology described above. Ratio images produced were fine tuned using the AutoColor function in Photoshop CS2. Comparison of the 750 nm image with the single ratio 750/1000 nm image shows good albedo compensation (the ratio image is is not saturated by bright albedo features) and the image is free of areas of deep shadow, which can also cause artifacts in ratio images. There is possible mafic
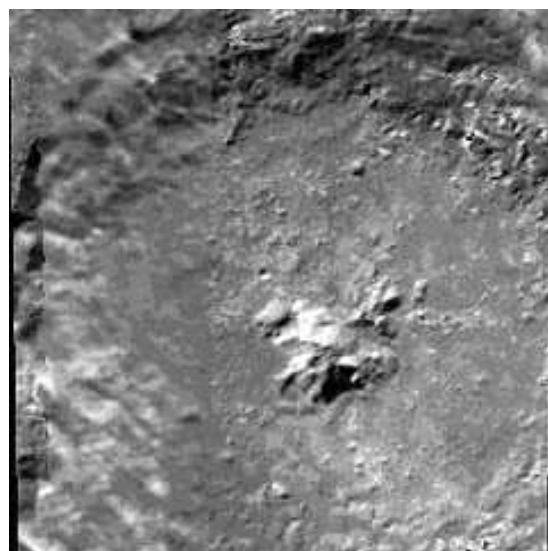
Fig. 1a 750 nm
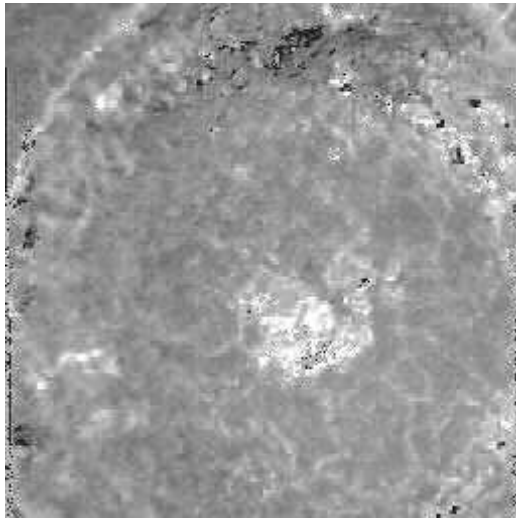
Fig 1b 750/1000 nm

material in the central peak and rim area which is best seen in the 750/1000 nm single ratio image as areas of brighter material. There is also a reticular pattern evident on the floor of the crater which is not evident in the 750 nm image, but is clearly seen in the single ratio image.

and the second with red=1000, green=900 and blue=415 nm.

Fig. 2b r/g/b=1000/900/415

These false color images emphasize the mafic materials present in the central peaks and crater walls. The mafic material appears in a purplish hue in the left image, and a deep garnet brown in the above image.

Next, two sets of ratio images were created. The first with channel assignments of red=750/415, green=750/1000 and blue=415/750 nm; and the second with red=750/900, green=750/1000 and blue=750/950 nm. The first type of ratio image emphasizes soil maturation and is sometimes called a maturation ratio image. The second type of ratio emphasizes mafic components and is sometimes called a mafic ratio image.

Fig.2a r/g/b=750/1000/415

Two different false color images were created, the first with channel assignments of red=750, green=1000 and blue=415 nm;

The maturation ratio image shows recent resurfacing of the lunar soils of the crater caused by the impact. Fresh surfaces appear greenish blue in this image while older mature soils appear reddish. Some artifact resulting from the pixel divisions used to produce this ratio image is noticable in the

image as hot red and hot blue pixels. This was felt to be due to the overall dark
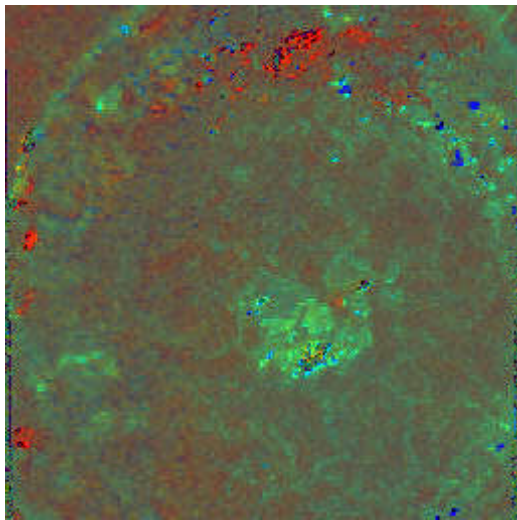
Fig. 3a Maturation Ratio
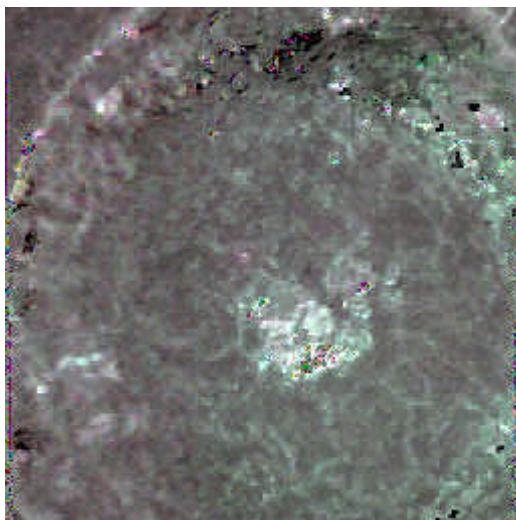
Fig.3b Mafic Ratio

appearance of the ratio image. A second mafic ratio image was therefore created using calibrated 415, 750 and 950 nm images of Tycho downloaded from the Fig.
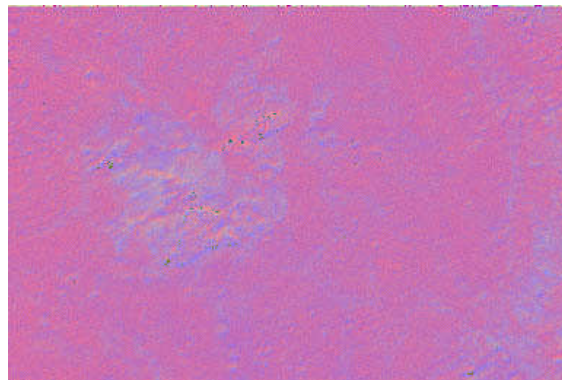
Fig.4a Unadjusted Calibrated Maturation Image
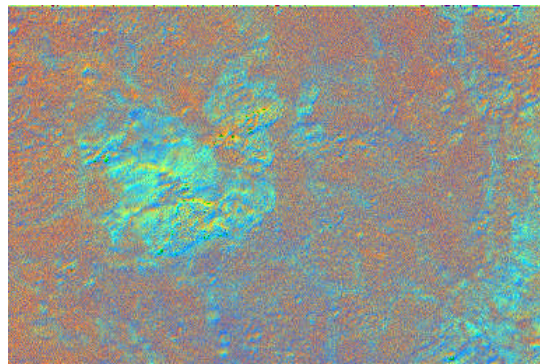
Fig. 4b RGB balanced Maturation Image

Clementine Lunar Image Browser 1.5 website (see http://www.cmf.nrl.navy.mil/clementine/clib/). The channels of the right image were balanced as described in Appendix 2.

The mafic image emphasizes the location of the iron absorption band center. When the bandcenter is close to 1000 nm, iron containing mafic materials appear bluish green. When the bandcenter is shifted closer towards 900 nm, the mafic materials appear reddish. The bright bluish green color in a mafic ratio image favors a high calcium pyroxene such as clinopyroxene which is found in gabbro. A bright reddish color in a mafic ratio image favors a low

calcium pyroxene such as orthopyroxene which is found in norite. Brilliant green coloration in this type of ratio image can suggest very high iron content as is found in olivines such as troctolite. The interpretation of the mafic image above would favor the presence of a gabbro as the mafic material.

Results Obtained from Raw Uncalibrated Clementine UVVIS/NIR Images:

It is of interest to compare the results obtained using fully calibrated images above with the raw Clementine UVVIS/NIR data set to determine the effect of calibration on ratio image appearance and to assess whether uncalibrated images have any limited value in the qualitative assessment of lunar mineral composition. The best Clementine images of Tycho's central peak area were identified within the Clementine raw image database. The following image set from orbit 40 was selected: LUA1786E.040, LUB1781E.040, LUC1778E.040, LUD1774E.040, and LUE1771E.040. A good way to begin the analysis of a lunar feature using these techniques is to compare an image at 750 nm with a single ratio image at 750nm /1000 nm. The first step in this example was to select set of raw UVVIS images from Clementine orbit 40 taken at 415, 750, 900, 950 and 1000 nm. The images were decompressed and converted to tif files using the clemdcmp.exe utility provided with the raw data on CD-ROM. The tif images were examined and converted to bmp files for co-registration using *Blink Comparator*. A single small bright feature common to all of the images was

selected to align on and the alignment was checked using the blink function in the program to rapidly view all of the files in succession. The aligned files were converted to jpg format and imported into *Image Arithmetic*. The following image pixel divisions were performed: 750/415, 750/1000, 415/750, 750/900, and 750/950 nm. The 750 nm image was compared to the 750/1000 nm image.

Fig. 5a 750 nm
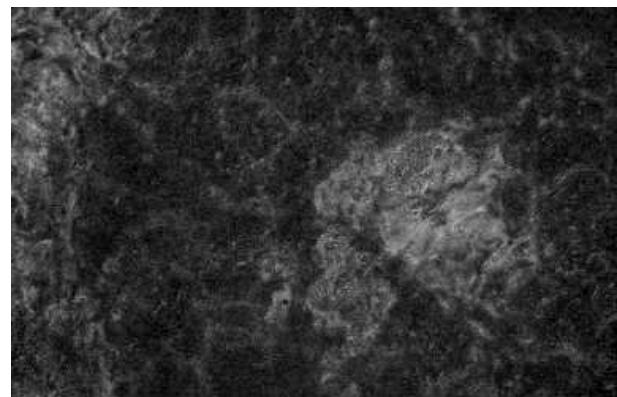
Fig.5b 750/1000 nm

The images are of good quality and are not over saturated by albedo features. The 750/1000 nm image removes what little albedo problems exist in the 750 nm

image. The brighter areas on the 750/1000 nm image have the potential to be mafic materials. The images show enough promise to warrant further processing of the image set.

The next step involves the creation of two false color images. The first was created by assigning 750, 1000, and 415 nm images to red, green and blue color channels. The second was created by assigning 1000, 750 and 415 nm images to red, green and blue color channels.

The next step involves creation of a "maturation" and a "mafic" composite ratio image. The maturation image is created by assigning the 750/415, 750/1000, and 415/750 nm images to the red, green and blue channels respectively. The mafic image is created by assigning 750/900, 750/1000, and 750/950 nm images to the red, green and blue channels.

Fig. 6a R=750 G=1000 B=415

Fig. 7a "Maturation" Ratio Image

Fig. 6b R=1000 G=900 B=415

Fig. 7b "Mafic" Ratio Image

The images begin to reveal a high likelihood that the central peaks are composed of mafic materials. The peaks are darker than the surrounding crater floor and show subtle compositional variation.
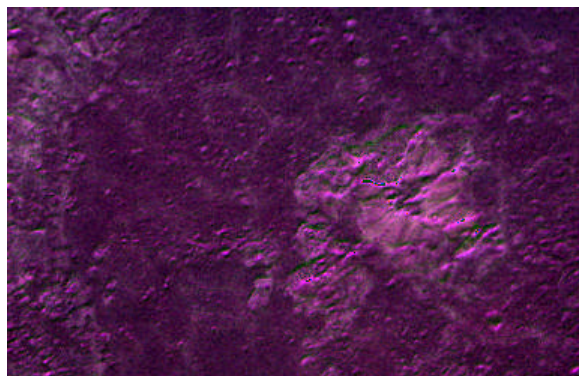
The strong green coloration in the maturation image confirms the mafic nature of the central peaks and adjacent crater wall. The floor of the crater consists of mature regolith with a reticulated pattern of mafic material spread on it. Although it has a strong mafic signature,

the mafic element composing the central peak is not olivine. If it were present olivine would have a green signature on the mafic ratio image. Rather, the mafic image coloration supports the mafic element being a pyroxene. It is sometimes possible to differentiate high calcium from low calcium pyroxenes (Yong-Liao et al., 2004; Tompkins, S., 2000). Raw uncalibrated images are poorly suited to this determination, however, my general experience has been that the color signature of the high calcium pyroxenes (clinopyroxenes) is bluish green through bluish violet on uncalibrated mafic ratio images whereas it is more distinctly blue green when fully calibrated images are used. I have also generally found that the signature of a low calcium pyroxene (orthopyroxene) is distinctly red in ratio images made from both calibrated and uncalibrated images. On that basis, it appears that the mafic ratio image above would hint at a high calcium pyroxene as the principal mafic component. If that is true, then the leading mineral contender might be clinopyroxene which is commonly found in gabbros. This is consistent with results obtained above using calibrated images and is consistent with current knowledge of the composition of the central peaks (Tompkins et al., 2000; Pieters & Englert, 1993). Creation and interpretation of mafic ratio images can be rewarding, but it is difficult.

Clementine also took NIR (near infrared) images at 1100, 1250, 1500, 2000, 2600, and 2780 nm. Unfortunately, to the best of the author's knowledge, these images were not generally available in fully calibrated form as this paper was being written, but they are expected to be available on the USGS PDS website

(http://pdsmaps.wr.usgs.gov/maps.html) in the near future. Of the near infrared images the most useful for the analysis of Tycho are the 1500 nm and 2000 nm images. A single ratio image of 2000 nm/1500 nm has been shown to be very useful in the discrimination between the pyroxenes and olivine. If the feature in question is bright in this ratio image then the presence of olivine is favored (Le Mouelic et al., 1098.pdf). This is because pyroxenes absorb at both 1000 nm and 2000 nm but olivine does not absorb at 2000 nm.
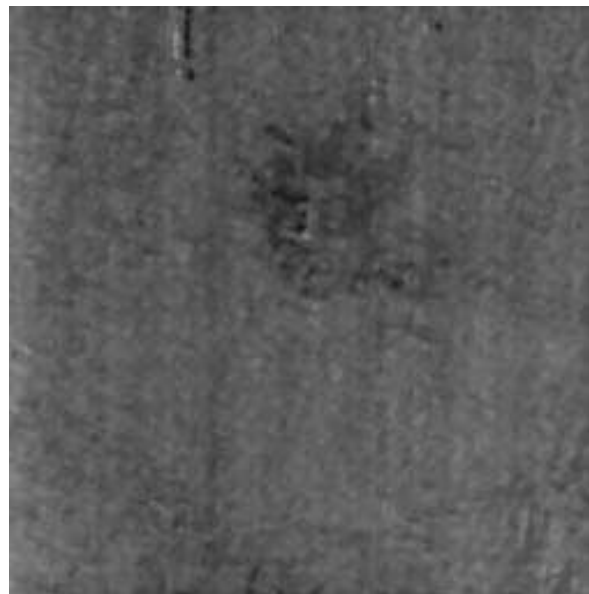
Fig. 7c 2000/1500

Since the central peak area is quite dark in the 2000/1500 nm ratio image, there is no indication of the presence of olivine, although it must be kept in mind that the images used were not calibrated.

Comparison of Calibrated and Uncalibrated Image Results:

The study of Tycho above appears to

indicate that some useful qualitative information can be extracted from false color and ratio images created from uncalibrated Clementine images. While the presence of mafic materials and the degree of soil maturation appear to be interpretable in uncalibrated images, more subtle determinations such as the presence of specific mafic materials (low calcium vs high calcium pyroxenes, and olivine containing minerals) that require interpretation of shifts of the center of the 1000 nm absorption band are much riskier to interpret using uncalibrated material.

V. Conclusions

Professional astronomers have long used false color and composite ratio images to study the geography and mineral composition of lunar features. The method described above provides a simple means for amateur astronomers to create their own false color and composite ratio images. Calibrated Clementine images should be used, but even uncalibrated images can provide some basic geologic and mineralogic information. Amateurs need no longer be constrained by the limited number of mafic ratio images currently accessible, but can use this technique to create such images as well as other false color and ratio images of lunar features of particular interest to them. The ratio images suggested in this paper are in common use, but other ratios can be employed. There is plenty of room for experimentation in this area. For example, Hiesenger et al. suggest the following channel assignments for improved differentiation of lunar basalts: red=750-400/750+400 green=750/990 blue=400/750 (Hiesinger et al., 2001)

Interested amateurs can be somewhat creative in their channel assignments after learning what the standard channel assignments have to offer. It is hoped that this will lead to a better understanding of lunar geology and mineral composition by amateur astronomers and perhaps open up a new and exciting area of research in the amateur astronomy community. Interesting projects worth pursuing also include obtaining and analyzing images of lunar features with amateur equipment using a series of broadband filters that match the specifications of Clementines UVVIS filters. Lunar features of interest due to their mineral composition or their reputation as sites of frequent transient lunar phenomena are well worth exploring with this technique.

Acknowledgements:

Appendix 1: Additional Examples

1. Aristarchus Crater

False Color and Ratio Images Created from fully calibrated Clementine UVVIS image set

Clementine UVVIS calibrated images of Aristarchus for five wavelength bands were downloaded from the USGS PDSMAPS serve in 8 bit jpg format. Images at 415, 750, 900, 950 and 1000 nm

were obtained for creation of ratio and false color images using the methodology described above. Ratio images produced were fine tuned using the AutoColor function in Photoshop CS2.
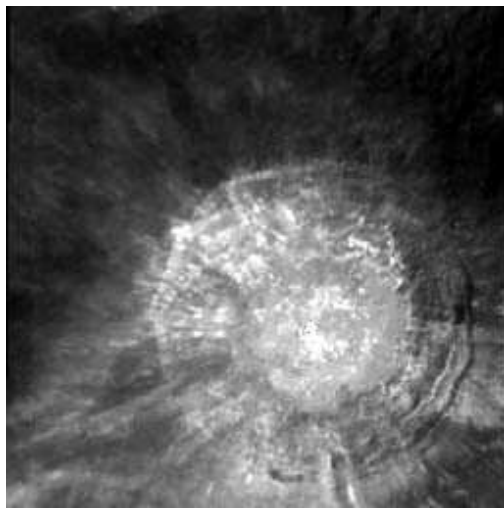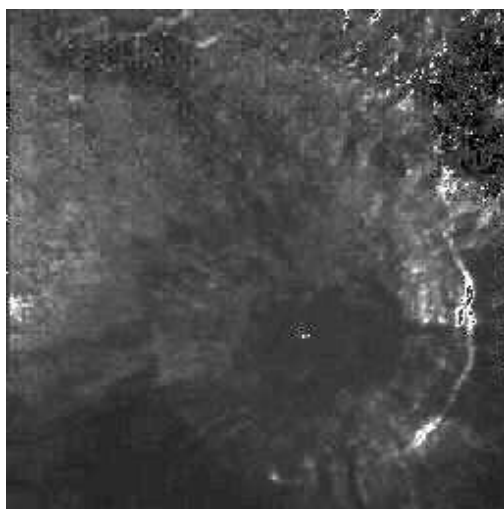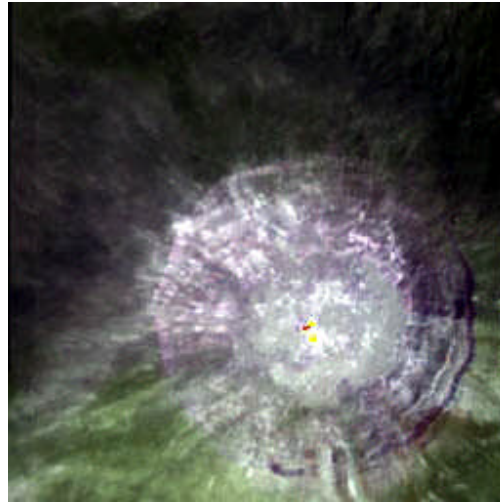

Fig 9a Red=750 Green=1000 Blue=415

compensates well for the excessive albedo present in the 750 nm image. There is an indication of some mafic materials in crater wall. Paired false color images created at red=750, green=1000, blue=415 and red=1000, green=900 and blue=415 shown below, indicate the presence of probable mafic materials in the crater wall which have a distinctly purplish hue.

Fig. 8a   750 nm

Fig. 9b   Red=1000 Green=900 Blue=415

Fig. 8b 750/1000 nm

The single ratio image at 750/1000 nm
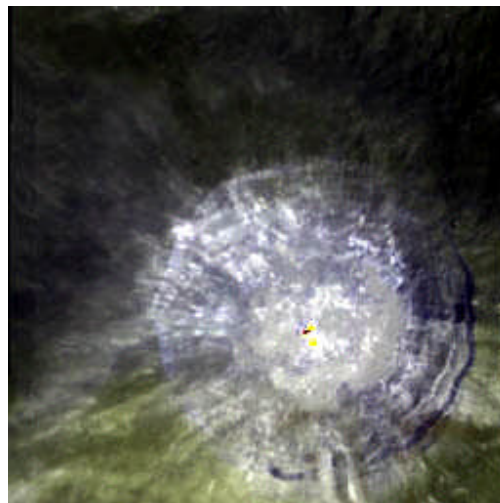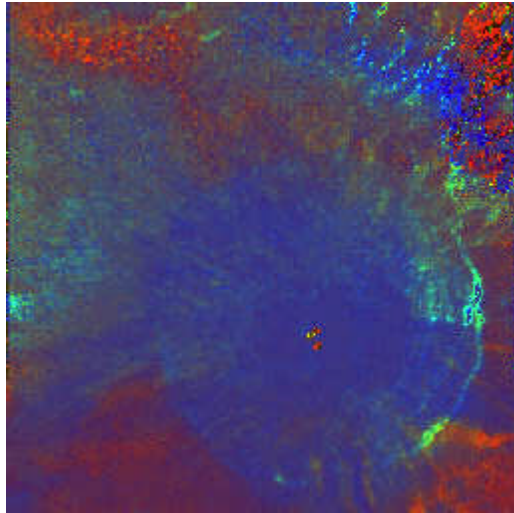
Fig. 10a Maturation Ratio

Fig 10b Mafic Ratio

False Color and Ratio Images Created from a Raw Uncalibrated Clementine UVVIS image set

It is important to select the best available image set and to minimize oversaturation by albedo as much as possible when choosing the image set. For this study of Aristarchus, Clementine orbit 053 was selected and a five image set converted to tif format. The original raw images were LUA4163L.053, LUB4158L.053, LUC4155L.053, LUD4151L.053 and LUE4148L.053. The images were examined for quality, converted to bmp format and co-registered using *Blink Comparator*. The 1000 nm image was then compared to the single ratio image 750 nm/1000 nm.

Fig. 11a 750 nm

The maturation ratio shows fresh resurfacing of the crater with adjacent lunar soils being mature and red except in areas where ejecta from the crater spill onto the adjacent plain. The mafic image shows bright blue green mafic signatures in the crater wall consistent with a high calcium pyroxene gabbro.
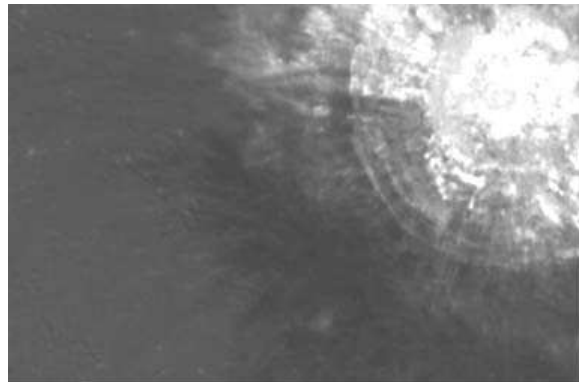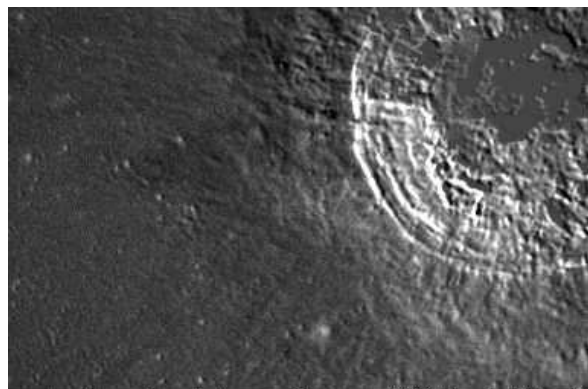
Fig. 11b 750/1000

The albedo variations appear to be manageable and much detail is present in the images. The 750/1000 image indicates the possibility of mafic material especially on the left rim area. The 750/1000 nm ratio image also helps to compensate for albedo problems in the 750 nm image. The next step is to create and examine false color images as in the preceding example. The first false color image had channel assignments of 750, 1000 and 415 nm for the red, green and blue channels respectively. The second false color image had channel assignments of 1000, 900 and 415 nm respectively.

Fig. 12a Red=750 Green=1000 Blue=415
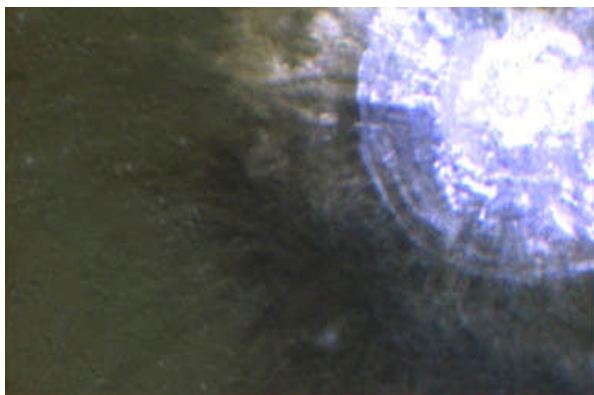
Fig. 12b Red=1000 Green=900 Blue=415

These images also support the possibility of mafic material, especially along the left rim area. Encouraged by these results, the next step was to create "maturation" and "mafic" composite ratio images as in the preceding example.
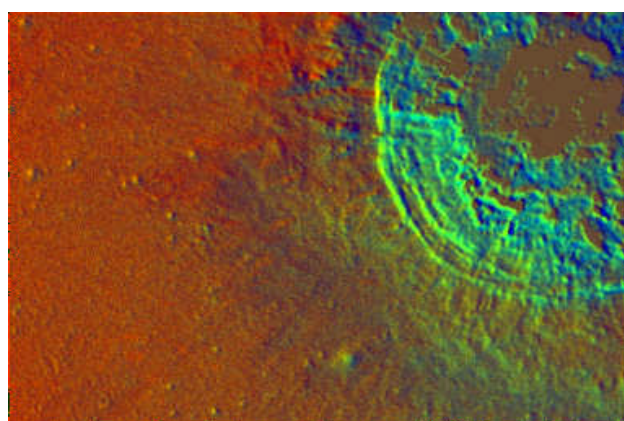
Fig. 13a Maturity Ratio Image
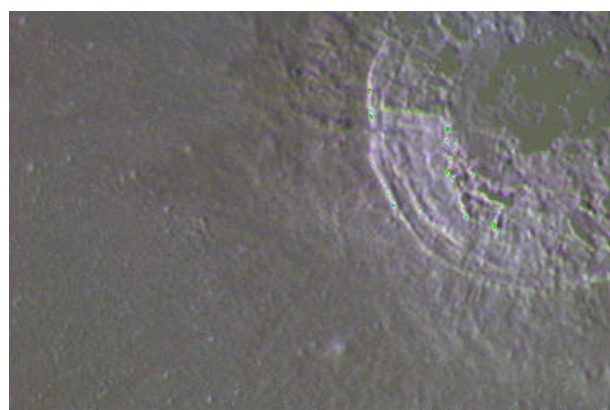
Fig. 13b Mafic Ratio Image

The maturity ratio image had the channel assignments red=750/415, green 750/1000 and blue 415/750 nm. The mafic ratio image had channel assignments

red=750/900, green=750/1000 and blue 750/950 nm. The maturation image shows mature regolith surrounding the crater. Even though the images are uncalibrated, there is a strong mafic signature suggestive of an iron magnesium silicate present in the area of the left rim of the crater. Also, some of this material appears to have spilled over into the adjacent regolith. The predominant color in the crater rim on the mafic image is purplish blue which is consistent with a high calcium pyroxene gabbro (clinopyroxene). These results are consistent with what was observed using the calibrated image set. The dull dark greenish grey material toward the center of the crater floor is consistent with anorthosite and may be impact melt (McEwen et al., 1994; Pieters and Englert, 1993). It is difficult to distinguish between olivines and pyroxenes using only UVVIS wavelengths and a definitive discrimination requires infrared analysis. Pyroxenes absorb both at 1000 and 2000 nm while olivine absorbs at 1000 nm but not at 2000 nm (Le Mouelic et al., 1098.pdf). In general, however, at UVVIS wavelengths olivine gives a brighter, stronger and greener signal than pyroxenes.
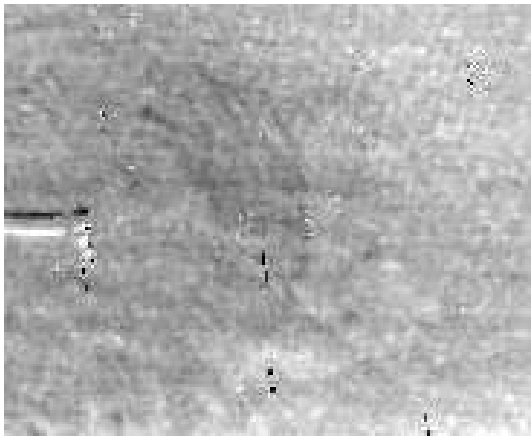
Fig 14a 2000/1500 nm

If we utilize the uncalibrated Clementine NIR images taken at 1500 nm and 2000 nm to create a single ratio image at 2000/1500 nm, this image may help to discriminate between pyroxenes and olivine (De Mouelic et al., 1098.pdf). Since olivine does not absorb at 2000 nm, brightness of the feature indicated by the letter A in the 2000/1500 nm favors the presence of olivine over pyroxenes.
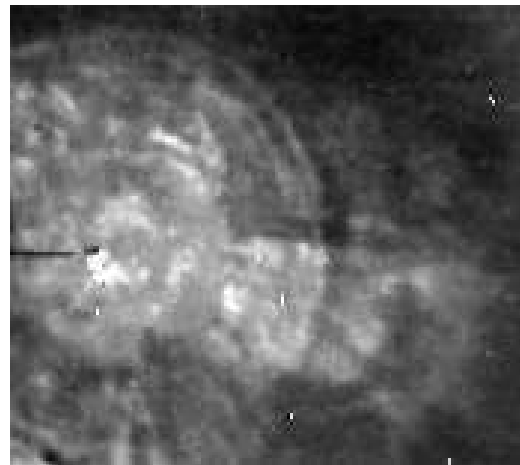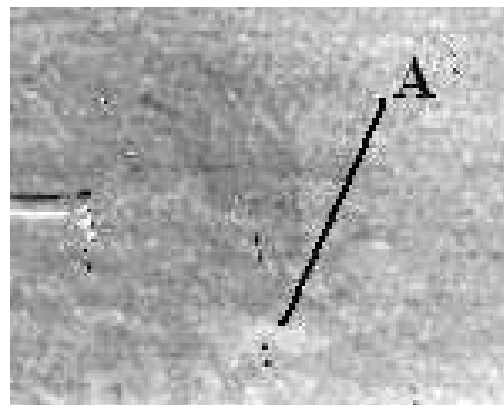

Fig. 14b 1500 nm

Fig. 14c 2000/1500 nm

Although of very poor quality due to noise in the infrared images, the ratio image shows a slight brightening of the crater rim extending to the area of

spillover into the adjacent mare. This is not as bright or as sharply defined as the area of olivine predominance discovered by De Mouelic (De Mouelic et al., 1098.pdf) and might just represent an artifact (particularly since the 2000 and 1500 nm images were uncalibrated). No olivine is detected within the central peak area or adjacent crater floor in this ratio image (only artifacts are present).

2. Bullialdus Crater

False Color and Ratio Images Created from Calibrated Clementine UVVIS Data

Clementine UVVIS calibrated images of Bullialdus for 5 wavelength bands were downloaded from the USGS PDSMAPS serve in 8 bit jpg format. Images at 415, 750, 900, 950 and 1000 nm were obtained for creation of ratio and false color images using the methodology described above. Ratio images produced were fine tuned using the AutoColor function in Photoshop CS2.
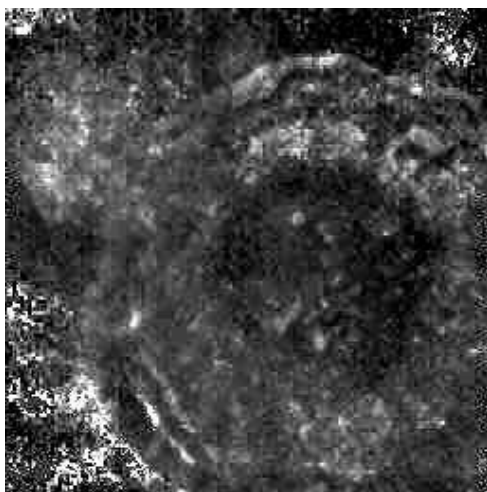
Fig. 15a 750 nm
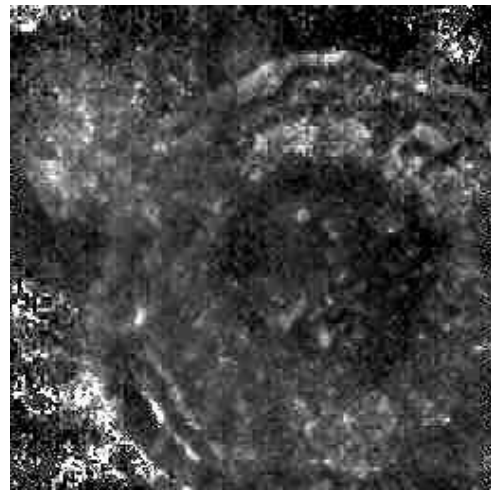
Fig. 15b 750/1000 nm

The 750 nm and 750/1000 nm images above show good albedo compensation by the ratio image and a suggestion of some mafic material in the central peaks and crater wall.
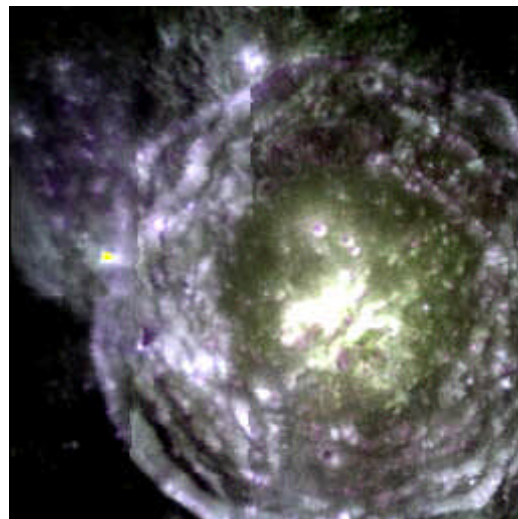

Fig. 16a Red=750 Green=1000 Blue=415

The paired false color images also indicate mafic materials in these locations by the presence of a purplish hue.
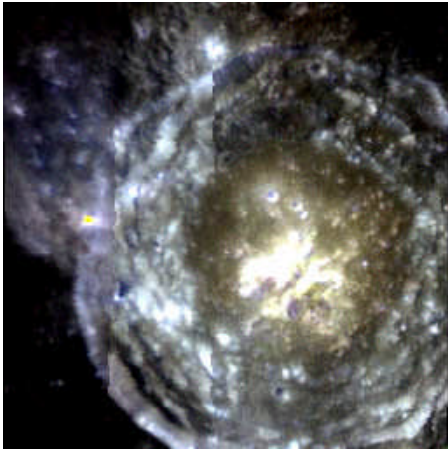
Fig 16b Red=1000 Green=900 Blue=415

Fig 17 Maturation Ratio

Fig 17b Mafic Ratio

The maturation image shows mature reddish soil on the crater floor and fresh re-surfacing of the central peaks and crater wall. Some ejecta is also present. The mafic image shows red coloration of the central peak suggestive of a low calcium orthopyroxene such as norite, but the crater walls show a blue green color characteristic of high calcium pyroxenes such as clinopyroxene, typically found in grabbo.

False Color and Ratio Images Created from Raw Clementine UVVIS Data
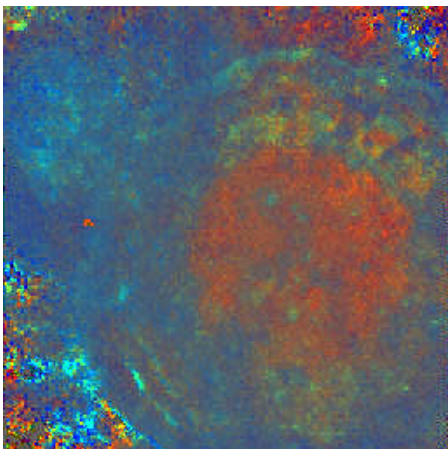
Again, the best possible Clementine images were selected for Bullialdus. These were from orbit 044 and the raw image subset was LUA2779G.044, LUB2774G.044,
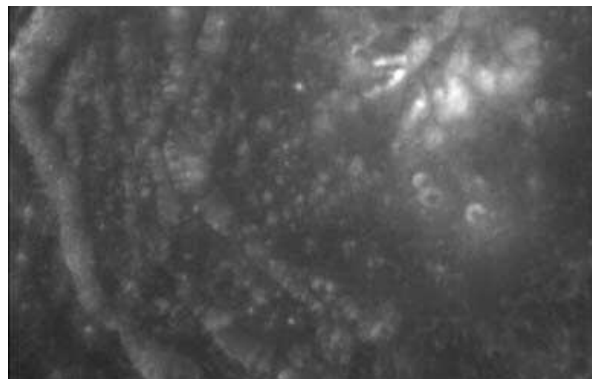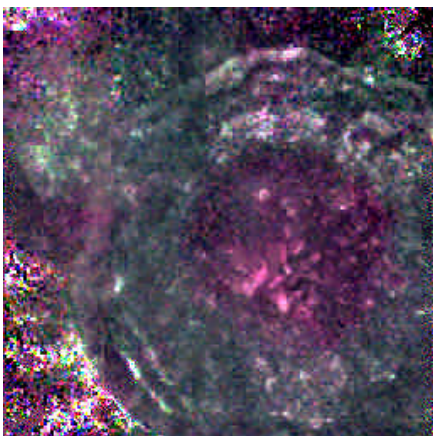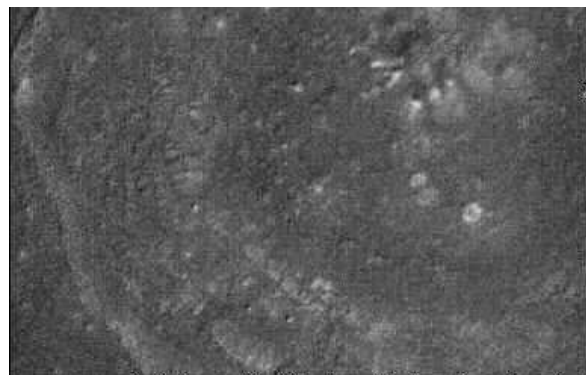

Fig 18a 750nm

Fig 18b 750/1000

LUC2771G.044,LUD2766G.044 and LUE2764G.044. The first step was to compare the 750 nm image with a single ratio image at 750 nm/1000 nm.

Albedo is not a problem in the images and there is an indication of some possible mafic material in the central peaks but most of the peak area is relatively dim and might have a significant component of anorthosite. The 750/1000 image compensates successfully for albedo problems present in the 750 nm image.

The next step is to create two sets of false color images . The first set with red=750, green=1000 and blue=415 nm. The second with red=1000, green=900 and blue=415 nm.
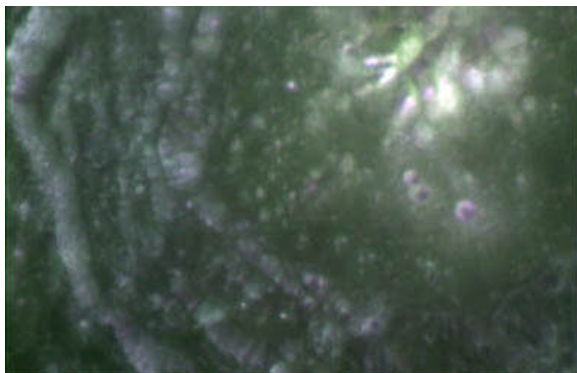

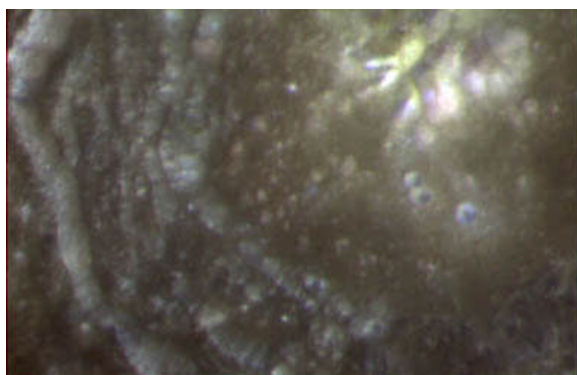*Fig. 19a Red=750 Green=1000 Blue=415*

Fig. 19bRed=1000 Green=900 Blue=415

These images appear to show some variation in central peak composition. The peaks may be composed of a mafic element in some areas and anorthosite in others. Further analysis involves creation of the maturation and mafic ratio images as in previous examples.
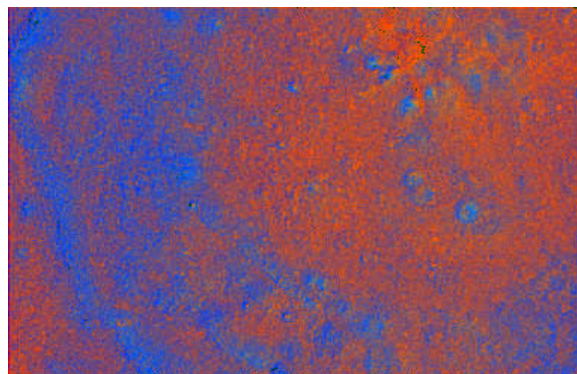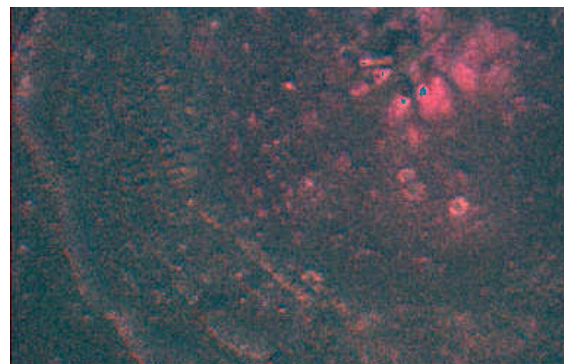

Fig. 20a   Maturation Ratio Image

Fig. 20b Mafic Ratio Image

The maturation image uses channel assignments: red=750/415, green 750/1000, and blue 415/750 nm. The mafic ratio image uses channel assignments: red=750/900 green=750/1000 and blue=750/950. The maturation image shows mature soils on the crater floor and outside the crater. The crater rim and minor portions of the central peaks show blue coloration consistent with "newly" exposed

surfaces. Somewhat surprisingly, the greater central peak area does not show more blue coloration. The mafic image shows strong reddish coloration of the central peaks consistent with substantial concentrations of a low calcium pyroxene such as orthopyroxene. Norite or noritic anorthosite might be considerations for central peak composition (Pieters and Englert, 1993). The peaks probably also contain areas of anorthosite. This interpretation is consistent with observations involving the calibrated image set, however the calibrated images also reveal substantial amounts of gabbro in the crater wall. This gabbro component was not suspected on review false color and ratio images created from the raw uncalibrated image set.

Using uncalibrated NIR images LNC2732G.044 (1500 nm) and LND2735G.044 (2000 nm), a single ratio image at 2000/1500 nm is made and examined. This image ratio selectively discriminates between pyroxenes which absorb at both 1000 nm and 2000 nm, and olivine which absorbs at 1000 nm but not at 2000 nm. In this ratio, areas of brightening suggest olivine while darker areas suggest pyroxenes.
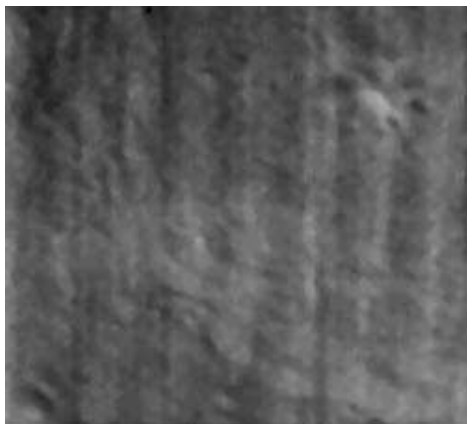

Fig 20c 2000/1500

Clementine ratio images are noisy, but in spite of the poor quality of the ratio image it is possible to identify brightening of a central peak suggesting the presence of olivine. Steutel and Lucey, 2001) identified coarse grained olivine in this central peak of Bullialdus using mid-infrared wavelengths. It appears that the ratio image above has captured essentially the same detail. The presence of olivine had not been suspected based upon the mafic image ratio. It appears that Bullialdus has a complex peak structure with areas of low calcium pyroxene (orthopyroxene), anorthosite, and olivine.

3. Copernicus Central Peaks and Rim

False Color and Ratio Images Created from Calibrated UVVIS Data

Clementine UVVIS calibrated images of Copernicus for 5 wavelength bands were downloaded from the USGS PDSMAPS server in 8 bit jpg format. Images at 415, 750, 900, 950 and 1000 nm were obtained for creation of ratio and false color images using the methodology described above. Ratio images produced were fine tuned using the AutoColor function in Photoshop CS2.

The 750 nm and the 750/1000 nm images show good albedo compensation and the possibility of mafic materials in the central peaks and crater wall (see Fig.21 a and 21 b).
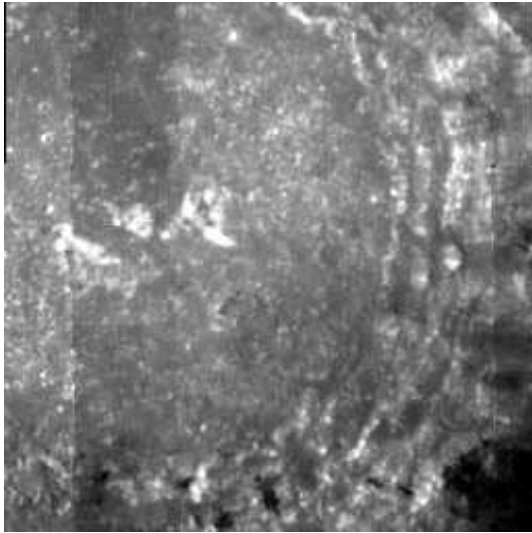
Fig. 21a 750 nm
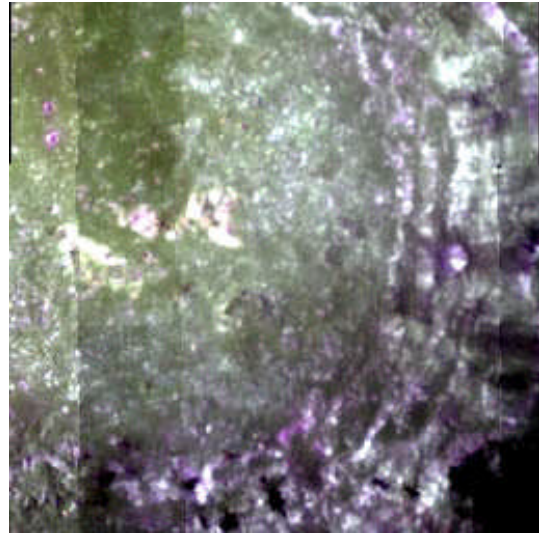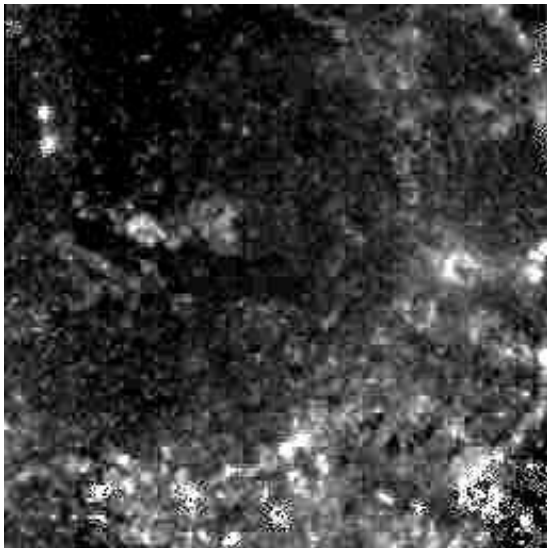

Fig. 22a Red=750 Green=1000 Blue=415
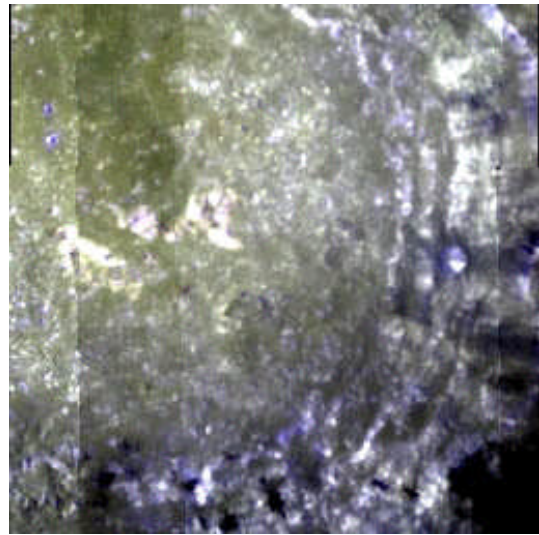

Fig. 21b 750/1000

Fig22b Red=1000 Green=900 blue=415

The paired false color image (Fig 22 a and 22 b) demonstate mafic materials in the central peaks and wall, which have a purplish hue.
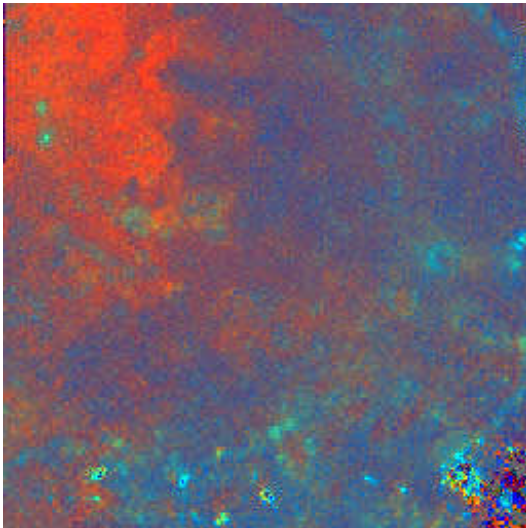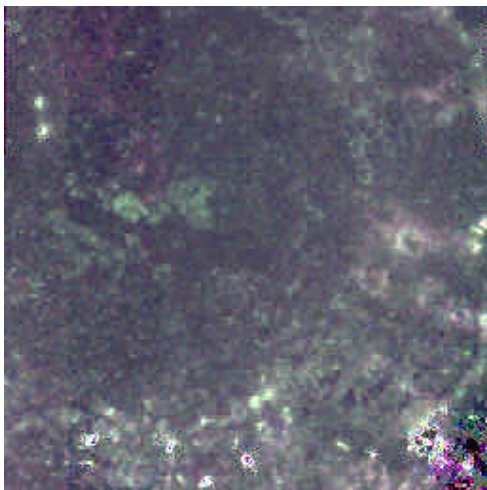
Fig. 23a Maturation Image

Fig. 23b Mafic Image

The maturation image shows both older mature soils and more recent resurfacing of the central peaks and crater walls. The mafic image shows green coloration of the central peaks consistent with mafic materials with a high content of iron. A 2000/1500 nm NIR image would be needed to differentiate clinopyroxene from a mineral like troctolite with a high olivine content.

False Color and Ratio Images Created from Raw UVVIS Data

As always it is important to choose the best images. The set used for this example are from Clementine orbit 176 and are the UVVIS images LUA2356J.176, LUB2351J.176, LUC2348J.176, LUD2344J.176 and LUE2341J.176. These were converted to tiff files using the clemdcmp.exe utility included on each Clementine CD-ROM disk. The tif files were examined for quality and then converted into bmp files and imported into *Blink Comparator* for co-registration. The co-registered files were then converted to jpg files and ratio images were created using *Image Arithmetic.* As usual, the first step in image analysis was to compare a 750 nm image (Fig 24a) with a single ratio image at 750nm/1000nm (Fig.24b).
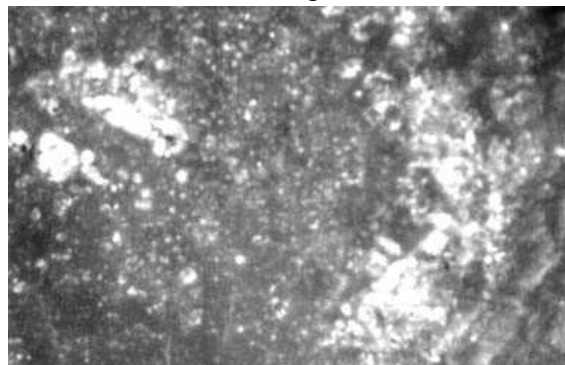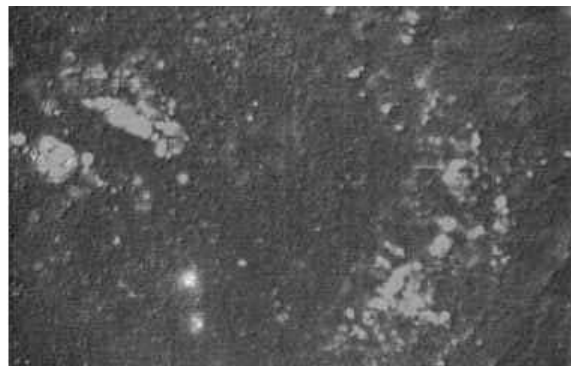

Fig. 24a at the top and Figure 24b at the bottom

The 750/1000 image helps to compensate for albedo oversaturation. Both images show bright areas that could be mafic material. The next step was to prepare two false color images. The first has channel assignments of 750, 1000, and 415 nm. The second has channel assignments of 1000, 900, and 415 nm.
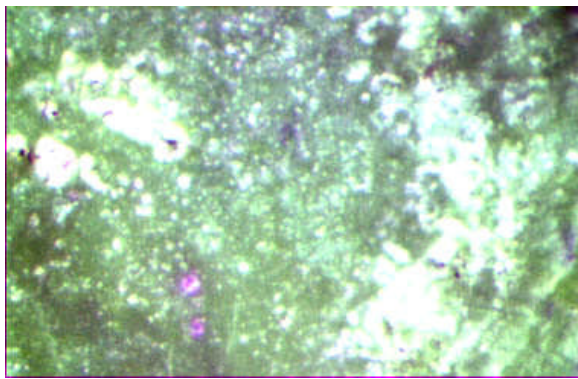
Fig. 25a Red=750 Green=1000 Blue=415
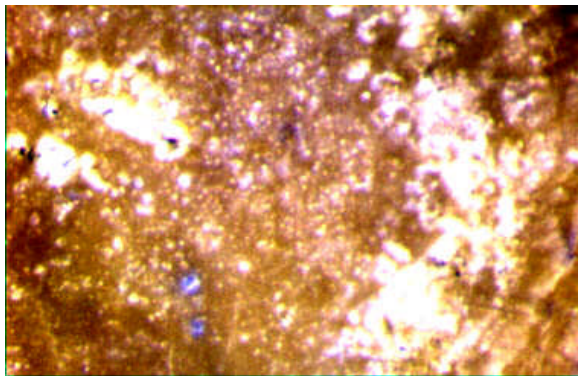
Fig. 25b Red=1000 Green=900 Blue=415

Both false color images show probable mafic materials in the central peaks. The next step was to create a maturation combined image ratio and a mafic combined image ratio as in previous examples. The maturation ratio had channel assignments of red=750/415, green=750/1000 and blue=415/750 nm. The mafic ratio had channel assignments of red=750/900, green=750/1000 and blue=750/950 nm.
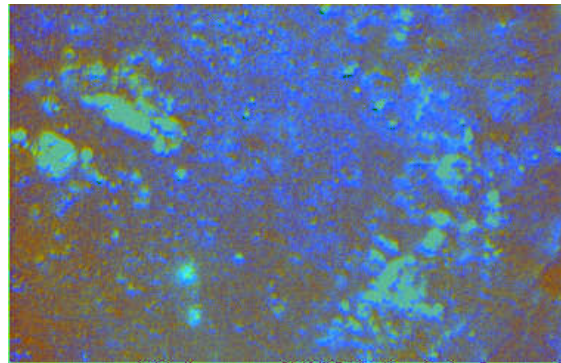
Fig. 26a Maturation Image
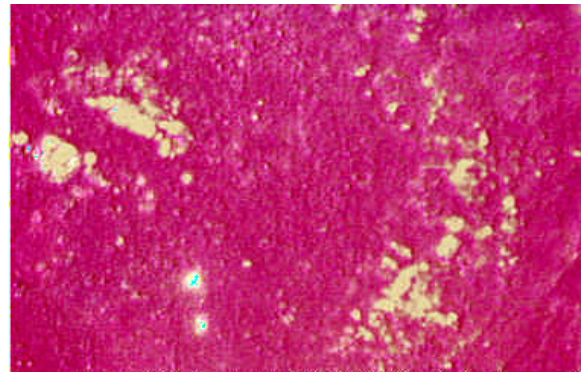
Fig. 26b Mafic Image

The maturation combined ratio image shows mature soil on the crater floor. There are blue signatures of "fresh" surfaces lacking maturity. Most impressive, however, are the strong green mafic signatures in the peaks and a portion of the rim. The mafic image confirms this impression. The bright green signature indicates an iron magnesium silicate (i.e. olivine). The mountains are consistent with being composed of an olivine rich rock like

troctolite (Pieters and Englert, 1993). Troctolite contains 10-60% plagioclase feldspar and the remainder is mostly olivine. Although olivine usually gives a stronger, brighter and greener signal than pyroxenes, definitive identification of olivine should be done at infrared wavelengths at described earlier (Le Mouelic et al., 1093.pdf). Neither the calibrated nor uncalibrated UVVIS image sets are capable of adequately differentiating gabbro from troctolite or olivine.

A single ratio image was created from Clementine NIR raw images LNC2350J.176 (1500 nm) and LND2355J.176 (2000 nm). The ratio 2000 nm/1500 nm ratio image has been shown by De Mouelic (De Mouelic et al., 1999) to discriminate between pyroxenes and olivine. Pyroxenes absorb both at 1000 nm and 2000 nm while olivine absorbs at 1000 nm but not at 2000 nm. As a result, the 1500 nm/2000 nm ratio image shows olivine predominance as bright patches and pyroxene predominance as dark patches.
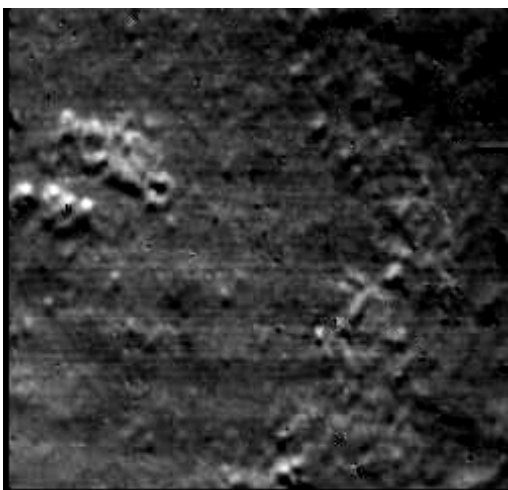
Fig. 26c 2000/1500

This ratio image supports olivine predominance in Copernicus' central peaks. Taken together with the maturation and mafic ratio images, there is a very strong indication of a strong olivine element in the central peaks. However, it must be borne in mind that the NIR images are uncalibrated.

Appendix 2: Channel Balancing

Color Channel Balancing of Raw Uncalibrated False Color and Ratio Images:

Color channel balancing as described in this section is not at all equivalent to image calibration, and it does not confer any ability to perform quantitative analysis using raw Clementine images. This section discusses color balancing of the red, green and blue channels in false color and ratio images made from either calibrated or uncalibrated Clementine images. The aim of color channel balancing, whether applied to single wavelength color channel assignments or ratio color channel assignments, was to allow each color channel to contribute as equally as possible to the final RGB image. In this way, qualitative compositional information present in each of the three color channels was allowed to make its contribution to the final RGB image. This was done by adjusting the brightness of the red, green and blue channels so that they were approximately of equal brightness and contributed equally to the final RGB image. After visually balancing the color channels so that they were of equal brightness to the eye, the AutoColor function in PhotoShop CS2 was used to

further fine tune the channel brightness levels. The contrast of the final RGB image was slightly adjusted when it improved overall image quality. This usually resulted in some dimming of the green channel.

The images of the Tycho central peaks shown below are all produced from raw uncalibrated Clementine images. The channel assignments were red=750, green=1000 and blue=415 nm. Figure 27a is unadjusted. In Figure 27b, the red green and blue color channels were manually adjusted so that they were of approximately equal brightness to the eye.
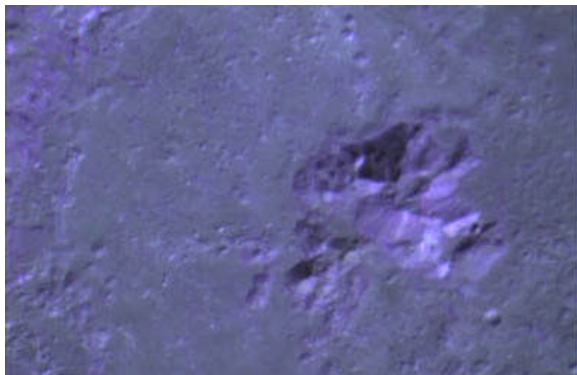
Fig. 27a Unadjusted
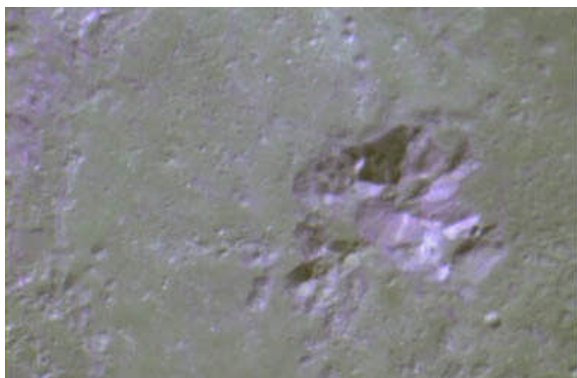
Fig. 27b Channels visually adjusted to equal brightness

In Figure 27c below, the AutoColor function in PhotoShop CS2 was applied to the visually adjusted channel result shown in Figure 27b. Figure 27d shows the result of increasing the contrast of Figure 27c by ten percent.

Fig. 27c AutoColor Function Applied

Fig. 27d Contrast Increased 10%

The final result reveals more geologic qualitative information than the original unprocessed raw image shown in Figure 27a.

Now a maturation ratio image will be processed by the identical procedure as that described above. Figure 28a shows an unadjusted maturation image with the following channel assignments: red=750/415, green=750/1000 and blue=415/750 nm. In Figure 28b, the

red, green and blue channels have been visually adjusted to approximately equal brightness levels.
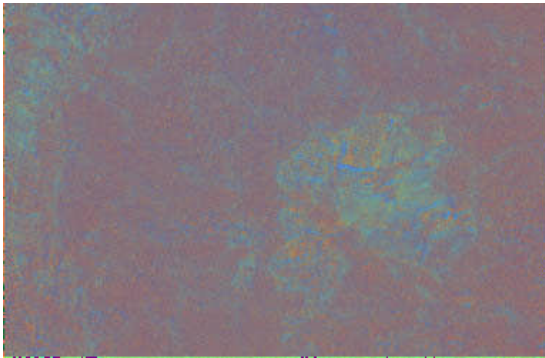
Fig. 28a Unadjusted
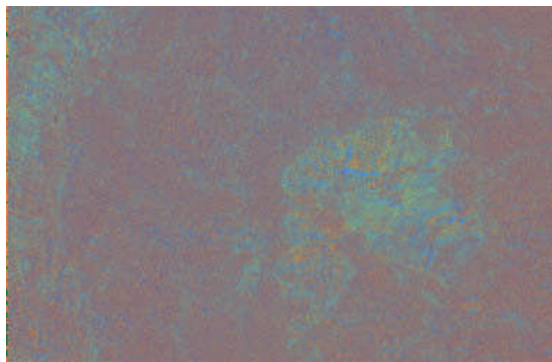
Fig. 28b Visual balancing of channel brightness
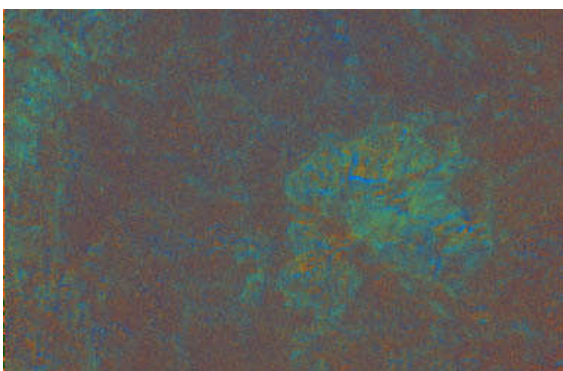
Fig. 28c AutoColor Function Applied

Figure 28c shows the result of applying the AutoColor function in Photoshop CS2, to the visually balanced result shown in Figure 28b. Figure 28d shows the result of increasing the contrast of the final RGB image by 50%.
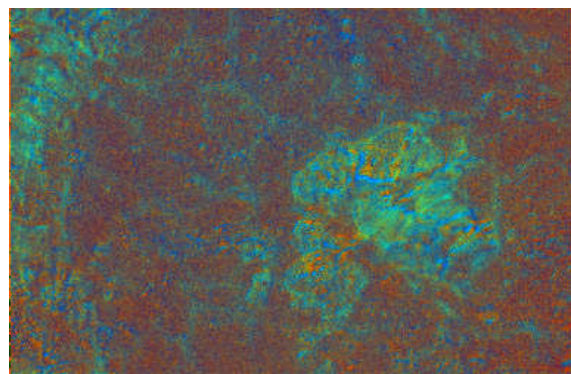
Fig. 28d RGB Image Contrast Increased 50%

The final result shows is a definite improvement over the unadjusted image.

References:

1. Yong-Liao Zou, Jian-Zhong Liu and Tao Xu, 2004. Reflectance Spectral Characteristics of Lunar Surface Materials. Chinese Journal of Astronomy and Astrophysics. Vol. 4 No. 1 pp. 97-104.

2. Pieters C and Englert P, 1993. Remote Geochemical Analysis: Elemental and Mineralogical Composition. Topics in Remote Sensing 4. (Cambridge University Press) Chapter 14 pp. 309-336.

3. Heicken, Grant; Vaniman, David; and French, Bevan editors, 1991. Lunar Sourcebook: A User's Guide to the Moon. (Cambridge University Press).

4. Tompkins, S; Margot, JL; Pieters, CM, 2000. Effects of topography on interpreting the composition of materials within the crater Tycho. Lunar and Planetary Science XXXI, abstract #1401.

5. Flor, EL; Jolliff, BL; Gillis, JJ, 2003. Mapping the concentration of iron, titanium,and thorium in lunar basalts in the western Procellarum region of the moon. Lunar and Planetary Science XXXIV, abstract#2086.

6. Hiesinger, H; Head, JW; Wolf, U; and Neukum, G, 2001. Lunar Mare Basalts: Mineralogical Variations with time. Lunar and Planetary Science. XXXII, abstract#8042.

7. Gillis, JJ; Jolliff, BL; Korotev, RL, 2004. Lunar surface geochemistry: global concentration of Th, K and FeO as derived from lunar prospector and clementine data. Geochimica and Cosmochimica Acta. Vol 68 (8) pp. 3791-3805.

8. Wieczorek, MA; Jolliff, BL; et al., 2006. The constitution and structure of the lunar interior. Reviews in Minerology and Geochemistry. Vol 60. pp. 221-364.

9. Giguere, T; Taylor, GJ; Hawke, BR; Lucey, PG, 2000. The titanium contents of lunar mare basalts. Meteoritics and Planetary Science. Vol 35. 193-200.

10. Lucey, PG; Blewett, DT. Hawke BR, 1998. Mapping FeO and TiO_2 content of the lunar surface with multispectral imaging. J. Geophysical Research Vol. 103 No. E2 p. 3679

11. Lucey, PG; Taylor, GJ;

Malaret, E, 1995. Abundance and distribution of iron on the moon. Science. Vol 268 pp. 1150-1153.

12. Gaddis, LR; Staid, MI et al., 2003. Compositional analyses of lunar pyroclastic deposits. Icarus. pp. 261-280.

13. Le Mouelic, S; Langevin, Y. Erard, S, 1999. Discrimination between olivine and pyroxene from Clementine NIR data: application to Aristarchus. Lunar and Planetary Science XXX 1098.pdf.

14. Spudis, PD; Shoemaker, E. et al., 1994. The Clementine Mission. Initial Mapping Results. NASA Goddard Space Flight Center. NASA TM-11-555 N95-24994.

15. McEwen, AS; Robinson, MS; Eliason, EM et al., 1994. Clementine observations on the Aristarchus region of the moon. Science.Vol. 266 pp. 1858-1862.

16. Steutel, D; Lucey, PG, 2001. Mid infrared multispectral imaging of the moon. Lunar and Planetary Science. XXXII, abstract#1975.

17. Malaret, E; Perez, L; Taylor H, 1999. ACTs (Applied Coherent Technology's) Final Report to NASA . Clementine's In-Flight Calibration Results (UVVIS Camera). (NASW-5014).

VERTICAL STUDIES ABOUT RUPES BÜRG

By Christian Wöhler, Raffaello Lena, Jim Phillips, Maria Teresa Bregante, Paolo Lazzarotti, Gerardo Sbarufatti

Geologic Lunar Research (GLR) group

Abstract

In this article we illustrate the results of a study about the slope and height of Rupes Bürg. The height of the fault amounts to 400 m and decreases towards the north, where it becomes a rille which fades away in the mare plane further to the north. The slope angle is about 19° for the highest and steepest part of the fault and decreases towards the north, where a slope of 8° was computed. The data are compared with preceding studies carried out on Rupes Cauchy and Rupes Recta and their slopes and heights.

1. Introduction

Mare Serenitatis is located in the northeastern Quadrant of the Moon. It is situated on the site of an ancient and large basin, irregular in outline, formed by a major impact during pre-Nectarian time. This basin has been flooded by basaltic lavas whose ages are ranging from 3.8 to 3.3 Ga. Mare Serenitatis appears smooth and nearly featureless with only a few wrinkle ridges and small craters within its basin. Geology and stratigraphy of the basaltic lavas in Mare Serenitatis have been extensively studied (Head, 1979 and references therein). The Mare Serenitatis spills into a smaller lava field named Lacus Somniorum, and then further north into the even smaller Lacus Mortis, located at 45°N and 27°E. This is an ancient lava flooded crater with several rilles: possibly faults laid in the bedrock by the Serenitatis impact and later reactivated by stresses created by lava loading. The western rim of Lacus Mortis is sharp and very straight, but the eastern rim is squashed in and is partially missing. Off-centre the conspicuous crater Bürg is situated: its walls contain deep clefts and its ejecta blanket can be seen thrown out into two main swaths heading north and south from the impact zone. Between these two swaths of material are two well-defined rilles that intersect to form a large T, known as Rimae Bürg. Under low solar altitude, two ridges can be seen running from Bürg to the northern and southern rims of Lacus Mortis. Moreover, the tectonic fault Rupes Bürg extends across the southern portion of the Lacus. When Rupes Bürg is observed near the terminator at sunrise, a shadow can be seen west of the fault. During the lunar day the width of this shadow decreases. At sunset the fault appears very bright because the sun shines more steeply on the surface of the fault than on the surrounding mare surface. This observation demonstrates that the mare surface east of Rupes Bürg is higher than the surface west of it.

Fig. 1: Image taken by C.Wöhler on May 3, 2006, at 20:09 UT.

2.1 Sunrise illumination: shadow lengths and height of the fault

The coordinates of several locations along the fault were determined superimposing our images onto the corresponding Lunar Aeronautical Chart. The undistorted scales of the images were measured based on the crater Plana C of 14 km diameter. The local solar altitude was computed for different locations along the fault with the Lunar Observer's Toolkit software by H. D. Jamieson. The images were rotated such that the shadows are oriented horizontally along the pixel rows in the direction of solar illumination, i. e. in east-west direction.

In Figs. 1-4 north is to the top and west to the left. Note that a circular crater is perspectivically distorted into an ellipse in the image. The diameter of the crater, measured in km, is divided by the major axis of this ellipse, measured in pixels, to obtain the undistorted image scale. Now a shadow length L measured in pixels can be expressed in km. The measured shadow lengths were corrected for foreshortening with the factor $1/\cos \lambda_{eff}$, where λ_{eff} represents the effective selenographic longitude relative to the observed centre of the apparent lunar disk. Due to the effect of libration, the centre of the lunar disk has the selenographic coordinates (λ_c, β_c) which can be obtained from an ephemeris. It can be shown by applying spherical trigonometry that the effective coordinates $(\lambda_{eff}, \beta_{eff})$ relative to the apparent disk centre are given by

$$\beta_{eff}= \arcsin [\cos \beta_c \sin \beta - \sin \beta_c \sin \lambda_c \sin \lambda \cos \beta - \sin \beta_c \cos \lambda_c \cos \lambda \cos \beta] \qquad (1)$$

$$\lambda_{eff}= \arcsin [(\cos \lambda_c \sin \lambda \cos \beta - \sin \lambda_c \cos \lambda \cos \beta) / \cos \beta_{eff}] \qquad (2)$$

where the selenographic longitude and latitude are given by λ and β, respectively. However, if no high accuracy is required, libration may be neglected and λ_{eff} approximated by λ to compensate for foreshortening. The height difference h corresponding to a measured shadow length L is given by

$$h = L \tan \alpha \qquad (3)$$

where α denotes the local solar altitude.

Fig. 1 displays Rupes Bürg under a low solar altitude. The image was taken on May 03, 2006, at 20:09 UT by C. Wöhler using a 20 cm Newtonian telescope (the undistorted scale of the image is 500 m per pixel). Fig. 2 was taken on March 06, 2006, at 01:18 UT by J. Phillips using a 15 cm TMB refractor (the undistorted scale of the image is 280 m per pixel). Fig. 3 was taken on March 16, 2005, at 19:53 UT by P. Lazzarotti using a 25 cm Newtonian telescope (the undistorted scale of the image is 300 m per pixel). Another image, shown in Fig. 4, was taken on April 4, 2006, at 19:46 UT by R. Lena using a 13 cm TMB refractor (the undistorted scale of the image is 470 m per pixel). The results of our shadow length measurements are shown in Tables 1-4.

2.2 Sunset illumination: width of the fault

The width of the fault, measured perpendicular to the direction in which it is running, was determined by measuring the pixel coordinates (u_1, v_1) and (u_2, v_2)
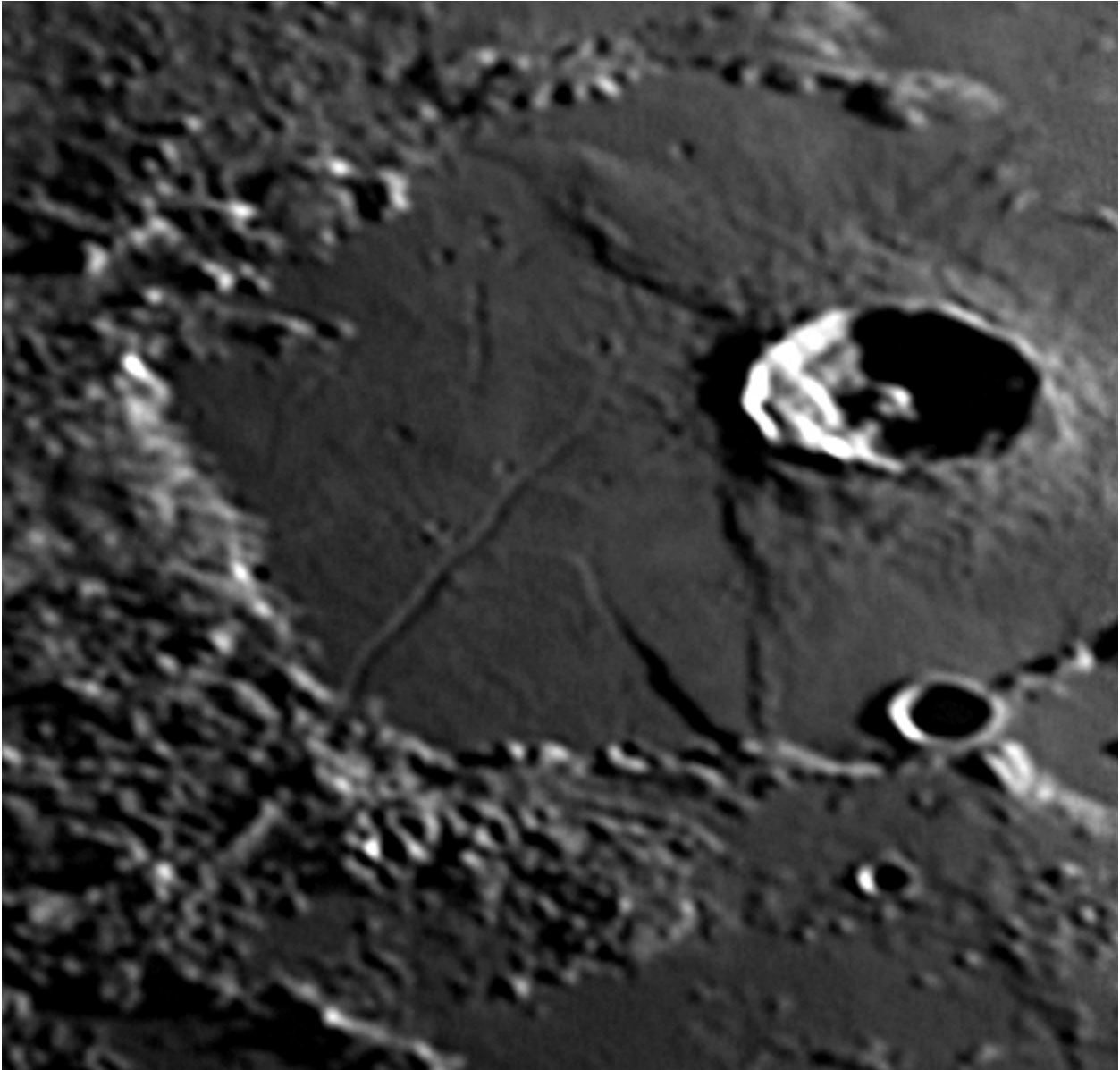
Figure 2: Image taken by J. Phillips on 6, 2006, at 01:18 UT.

of corresponding locations on both sides of the fault, respectively. Shadow length and fault width are thus measured in different directions. The upper left corner of the image has the coordinates $u = v = 0$. The image must be oriented north to the top and west to the left (Wöhler et al, 2006). The fault width w in pixels, corrected for foreshortening, is given by

w= sqrt $[(((u2 - u1) + |v2 - v1| \tan \beta \text{eff} \sin \lambda \text{eff}) / \cos \lambda \text{eff})^2 + ((v2 - v1) / \cos \beta \text{eff})^2]$. (4)

This rather complex relation results from the fact that in the image, distances in east-west direction are distorted by a different amount than distances in north-south direction. Note that Eq. (4) only holds if location 2 is north of location 1, which also means that $v2 < v1$.

Eq. (4) corresponds to measuring the width w on a map in simple cylindrical projection (Greeley and Batson, 1990) and is therefore only accurate for low to moderate latitudes and as long as a small latitude range is covered by the width of the fault. The value of w measured in pixels according to Eq. (4) can immediately be translated into kilometres by multiplying it with the previously determined undistorted pixel scale.

Fig. 5 displays Rupes Bürg under sunset illumination. This image was taken on October 03, 2004, at 01:18 UT by P. Lazzarotti, using the same equipment as for Fig. 3. In this image, the fault appears as a bright line. The undistorted scale of the image is 390 m per pixel. Fig. 6 was made on December 31, 2004, at 03:31 UT by G. Sbarufatti, using a 20 cm Schmidt-Cassegrain telescope. The undistorted scale of the image was determined to 466 m per pixel. Measurements of the fault width carried out in this image are in agreement with the data obtained for Fig. 5. The results for the width of Rupes Bürg are reported in Tables 5-6.

2.3 Width of the fault measured on Lunar Orbiter image

The width of the fault has been estimated using a Lunar Orbiter image (Fig. 7). The scale is 68 m per pixel, computed based on the 40 km crater Bürg. Here the fault is not wider than 17 pixels, corresponding to 1.16 km (Table 7). The larger values we measured in the telescopic images are caused by the effect of the Point Spread function (PSF) due to the telescope aperture and, more significantly, the seeing, leading to an effective image resolution which is comparable to or lower than the fault width. This effect typically occurs for narrow faults observed when they appear brighter than their surrounding. A diagram with the intensity cross-sections of Rupes Bürg at local sunset (Fig. 5), extracted perpendicular with respect to the fault for the seven locations we examined, is shown in Fig. 8 along with the width of the fault (1.16 km) measured in the Lunar Orbiter hires image.

2.4 Slope of the fault

Based on the data we measured, the slope ζ of the Bürg fault was computed using the relation

$\zeta = \arctan (h/w)$,   (5)

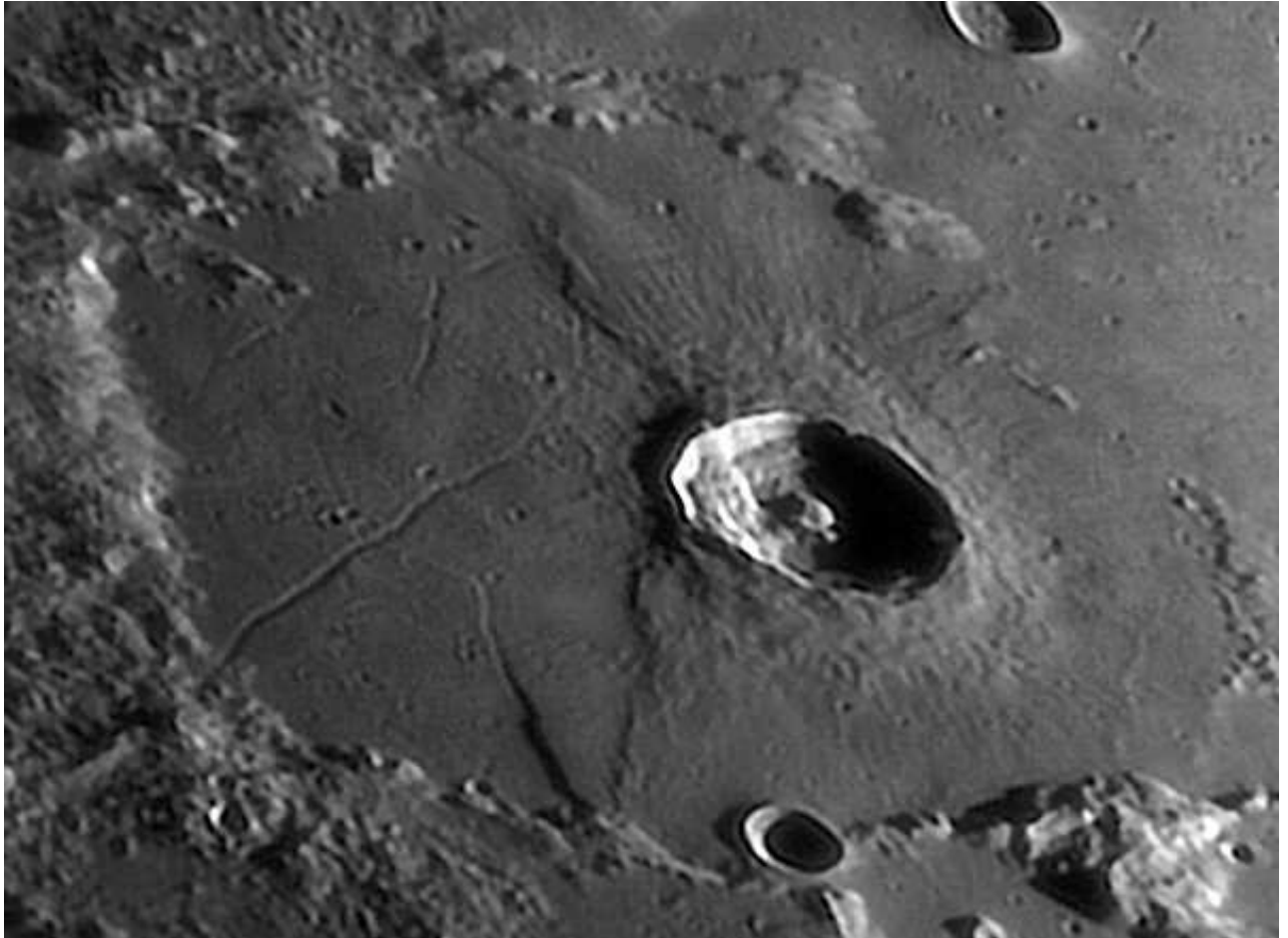where h and w denote the average

Fig. 3: Image taken by P. Lazzarotti on March 16, 2005, at 19:53 UT.

Table 1: Shadow length measurements obtained using the image shown in Fig.1

Longitude [°]	Latitude [°]	Solar altitude [°]	shadow length [pixels]	Shadow length (corrected for foreshortening) [pixel]	shadow length [km]	Height [m]
25.83	43.00	4.87	9±1	9.79	4.24±0.50	361±40
25.74	43.16	4.80	9.5±1	10.33	4.47±0.50	375±40
25.75	43.33	4.79	10.5±1	11.42	4.94±0.50	414±40
25.66	43.50	4.72	8.5±1	9.24	4.00±0.50	330±40
25.66	43.66	4.71	7.5±1	8.15	3.53±0.50	291±40
25.66	43.74	4.71	5±1	5.43	2.35±0.50	194±40
25.66	43.82	4.70	4.5±1	4.89	2.12±0.50	174±40

Table 2: Shadow length measurements obtained using the image shown in Fig. 2

Longitude [°]	Latitude [°]	Solar altitude [°]	shadow length [pixels]	Shadow length (corrected for foreshortening) [pixel]	shadow length [km]	Height [m]
25.83	43.00	6.25	12±1	13.33	3.73±0.30	408±30
25.74	43.16	6.16	12±1	13.33	3.73±0.30	401±30
25.75	43.33	6.15	12±1	13.33	3.73±0.30	400±30
25.66	43.50	6.06	7±1	7.76	2.17±0.30	230±30
25.66	43.66	6.06	5±1	7.76	2.17±0.30	230±30
25.66	43.74	5.99	5±1	5.54	1.55±0.30	161±30
25.66	43.82	5.99	5±1	5.54	1.55±0.30	161±30

Table 3: Shadow length measurements obtained using the image shown in Fig. 3

Longitude [°]	Latitude [°]	Solar altitude [°]	shadow length [pixels]	Shadow length (corrected for foreshortening) [pixel]	shadow length [km]	Height [m]
25.83	43.00	7.26	10±1	11.11	3.33±0.30	418±30
25.74	43.16	7.17	10±1	11.11	3.33±0.30	413±30
25.75	43.33	7.02	10±1	11.11	3.33±0.30	412±30
25.66	43.50	6.93	6±1	6.66	1.99±0.30	244±30
25.66	43.66	6.91	6±1	6.66	1.99±0.30	243±30
25.66	43.74	6.91	4±1	4.44	1.33±0.30	162±30
25.66	43.82	6.88	4±1	4.44	1.33±0.30	162±30

Table 4: Shadow length measurements obtained using the image shown in Fig. 4

Longitude [°]	Latitude [°]	Solar altitude [°]	shadow length [pixels]	Shadow length (corrected for foreshortening) [pixel]	shadow length [km]	Height [m]
25.83	43.00	8.77	5±1	5.55	2.58±0.50	392±40
25.74	43.16	8.68	5±1	5.55	2.58±0.50	390±40
25.75	43.33	8.67	5±1	5.55	2.58±0.50	388±40
25.66	43.50	8.58	3±1	3.33	1.55±0.50	230±40
25.66	43.66	8.56	3±1	3.33	1.55±0.50	230±40
25.66	43.74	8.55	2±1	2.28	1.06±0.50	158±40
25.66	43.82	8.54	2±1	2.28	1.06±0.50	158±40

Table 5: Measurements of the width of Rupes Bürg obtained using the image shown in Fig. 5

Longitude [°]	Latitude [°]	Solar altitude [°]	Width of the fault (corrected for foreshortening)	Width of the fault [km]
25.83	43.00	11.07	6.9±1.0	2.7±0.4
25.74	43.16	11.11	6.9±1.0	2.7±0.4
25.75	43.33	11.08	6.9±1.0	2.7±0.4
25.66	43.50	11.11	6.9±1.0	2.7±0.4
25.66	43.66	11.09	6.9±1.0	2.7±0.4
25.66	43.74	11.07	6.9±1.0	2.7±0.4
25.66	43.82	11.06	6.9±1.0	2.7±0.4

Table 6: Measurements of the width of Rupes

Longitude [°]	Latitude [°]	Solar altitude [°]	Width of the fault (corrected for foreshortening)	Width of the fault [km]
25.83	43.00	6.51	5.8±1.0	2.7±0.5
25.74	43.16	6.54	5.8±1.0	2.7±0.5
25.75	43.33	6.53	5.8±1.0	2.7±0.5
25.66	43.50	6.55	5.8±1.0	2.7±0.5
25.66	43.66	6.54	5.8±1.0	2.7±0.5
25.66	43.74	6.52	5.8±1.0	2.7±0.5
25.66	43.82	6.51	5.8±1.0	2.7±0.5

Table 7: Measurements of the width of Rupes Bürg obtained using the Lunar Orbiter image shown in Fig. 7.

Longitude [°]	Latitude [°]	Width of the fault [pixels]	Width of the fault [km]
25.83	43.00	17±1.0	1.16±0.07
25.74	43.16	17±1.0	1.16±0.07
25.75	43.33	17±1.0	1.16±0.07
25.66	43.50	17±1.0	1.16±0.07
25.66	43.66	17±1.0	1.16±0.07
25.66	43.74	17±1.0	1.16±0.07
25.66	43.82	17±1.0	1.16±0.07

Table 8: Height and slope values obtained for different locations along Rupes Bürg.

Longitude [°]	Latitude [°]	Width of the fault [km]	Height [m]	Slope [°]
25.83	43.00	1.16±0.07	396±30	18.84
25.74	43.16	1.16±0.07	395±30	18.80
25.75	43.33	1.16±0.07	403±30	19.15
25.66	43.50	1.16±0.07	258±30	12.53
25.66	43.66	1.16±0.07	248±30	12.07
25.66	43.74	1.16±0.07	169±30	8.28
25.66	43.82	1.16±0.07	164±30	8.05

Figure 4: Image taken by R. Lena on April 4, 2006, at 19:46 UT.

Figure 5: Image taken by P. Lazzarotti October 03, 2004, at 01:18 UT.

Results and discussion

Based on measurements of the shadow length and the width of Rupes Bürg, the height and the slope angle of Rupes Bürg were calculated for several locations. The height of the fault amounts to 400 m and decreases towards the north, where it becomes a rille which fades away in the mare plane further to the north. Correspondingly, the slope angle is about 19° for the highest and steepest part of the fault and decreases towards the north, where a slope of 8° was computed.

A study about Rupes Cauchy was recently published by Wöhler et al (2006). The height of Rupes Cauchy was determined as 340 m in the centre, slightly decreasing towards the south. The slope angle is about 12° for the highest and steepest part of the fault and decreases towards the north and the south. Hence, Rupes Bürg is steeper than Rupes Cauchy. Future observing schedules of the GLR group are being planned to investigate different lunar rupes on a case by case basis. The collected data and measurements will yield a core set of observations upon which more statistical analysis can be performed.

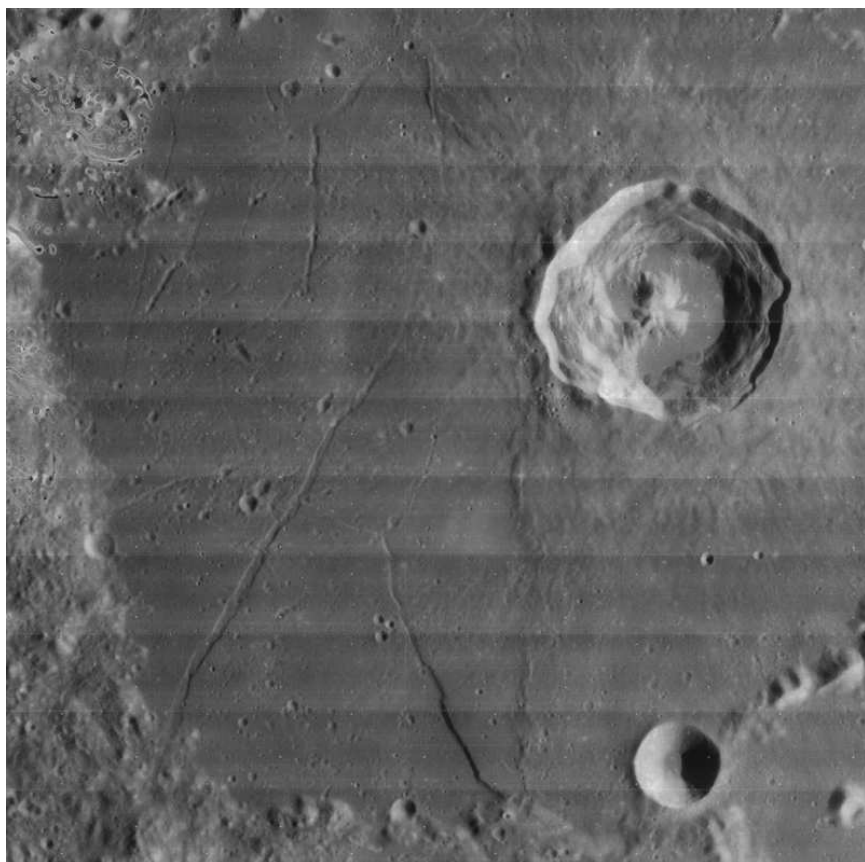*Fig. 6: Image taken by G. Sbarufatti December 31, 2004, at 03:31 UT.*
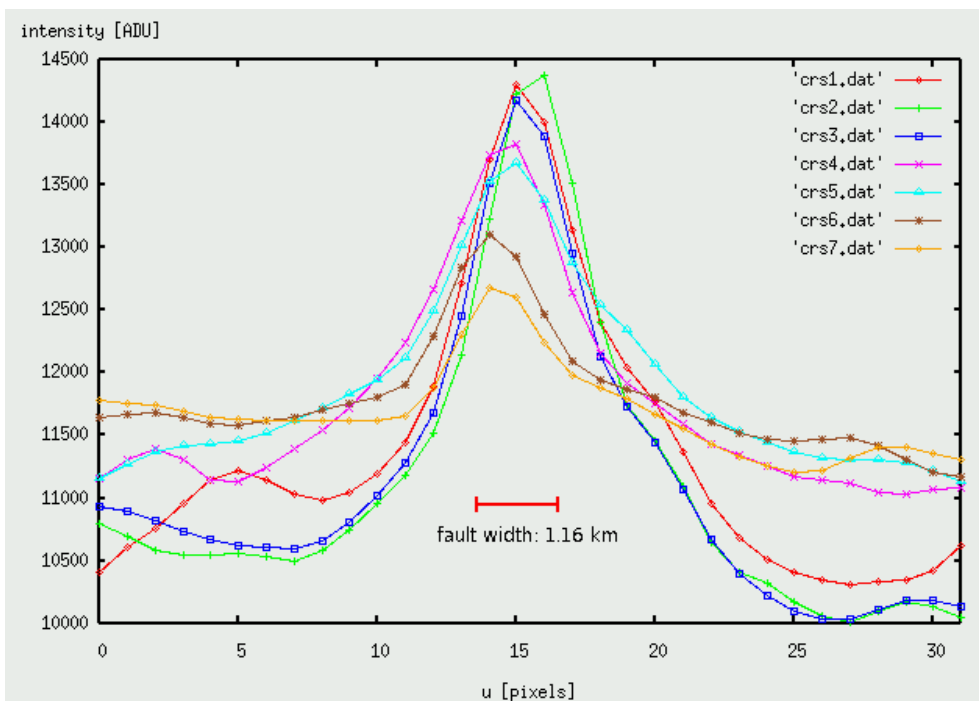
Fig. 7: Hires Lunar Orbiter Image IV-091-H2).

Fig. 8: Intensity cross-sections of Rupes Bürg at local sunset, extracted perpendicular with respect to the fault for the seven locations examined.

References

[1] Greeley, R., Batson, R. M., Planetary Mapping, Cambridge University Press, Cambridge, UK, 1990.

[2] Head, J. W., Serenitatis multi ringed basin: regional geology and basin ring interpretation, Moon and the Planets vol. 21, pp. 439-462, 1979.

[3] Wöhler, C., Lena, R., Bregante, M. T., Lazzarotti, P., Phillips, J., Vertical Studies about Rupes Cauchy, Selenology, vol.1, pp. 7-12, 2006.
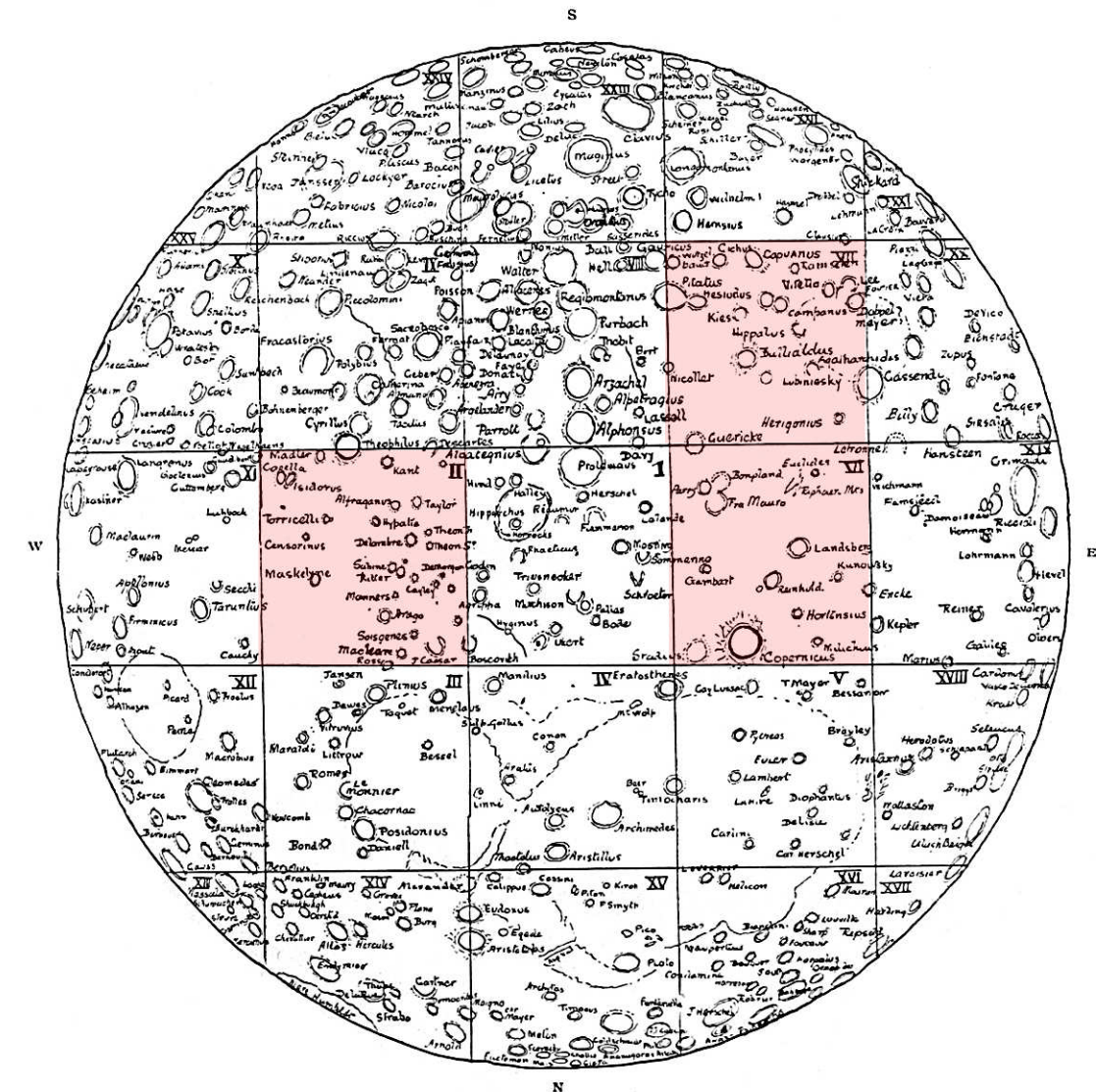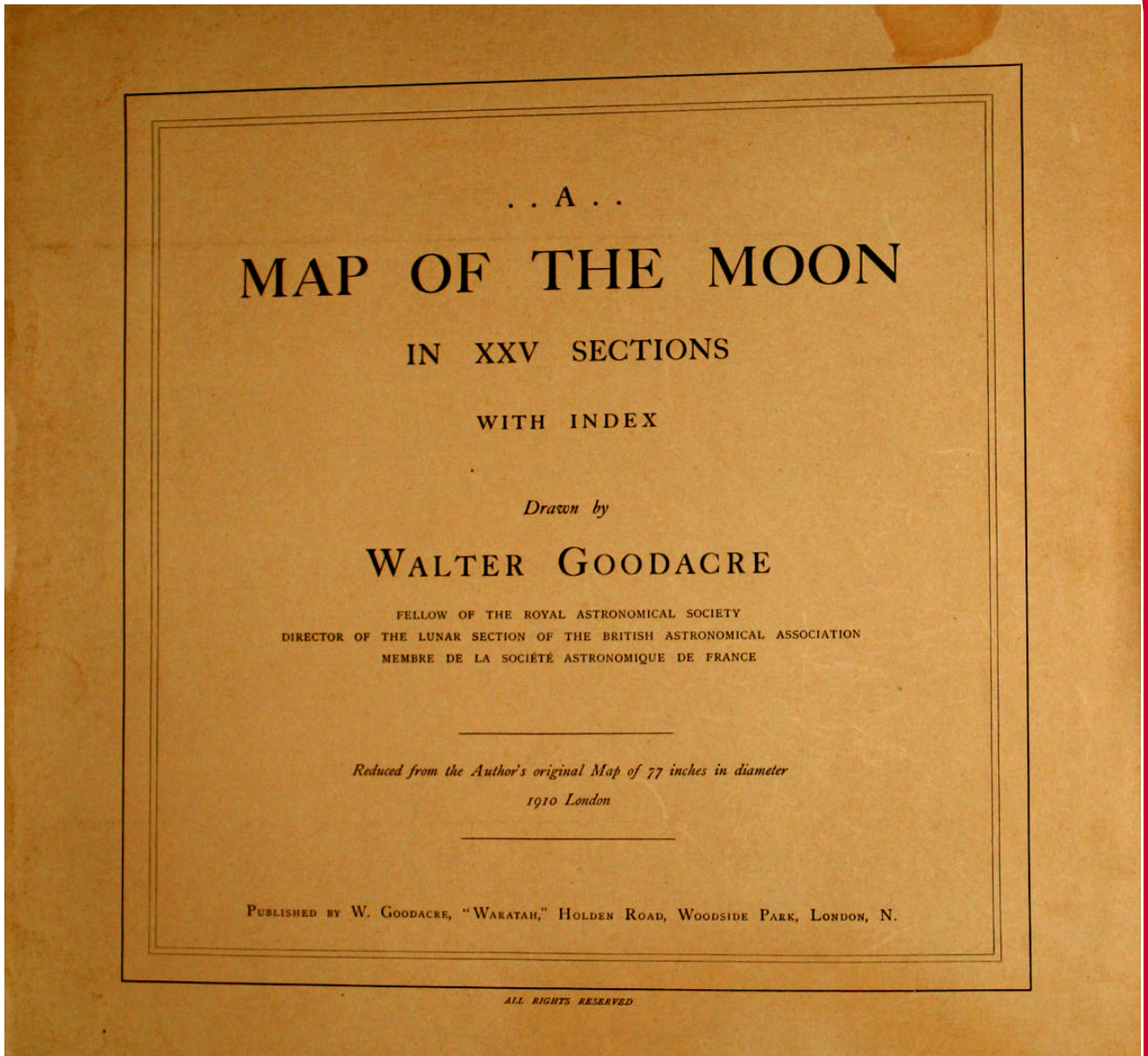
GOODACRE'S 1910 MAP OF THE MOON

Jim Phillips and Maria Teresa Bregante

Geologic Lunar Research (GLR) Group

When Galileo announced the existence of mountains, craters, and "seas" on the Moon, in the spring of 1610, our view of the universe was forever changed. Since antiquity the moon had been considered a "heavenly" body, eternal, immune to change. Galileo's observations showed that the Moon possessed topographic features similar to our own planet. This discovery raised questions about the Moon itself. If the Moon is a world, what is it like? Observers of the Moon have tried to answer these questions over the years since Galileo's observations. Pioneer lunar observers were only able to see detail on the Moon using unwieldy 100-foot telescopes, yet how beautiful their lunar engravings still appear. The detail present within the great nineteenth-century visual lunar atlases is astonishing, and the beauty seen within the turn-of-the-century photographic atlases, printed in brilliant photogravure or collotype, is

is absolutely stunning.

Here, we would like to present, for the interest of the avid lunar observer, some plates from the stunning 1910 lunar atlas, A Map of the Moon in XXV Sections**,** by W. Goodacre.

We have chosen to reproduce three sections showing details of lunar regions of special interest including domes studied by GLR. Section II centers on Mare Tranquilitatis and contains the well-known Arago domes, as well as the Apollo 11 landing site. In section IV, the craters Copernicus, Milichius and the classic dome near it can be seen. Also, Hortensius and the six well-known domes to the north, the so-called Schlumberger domes, are present. In Goodacre's book, The Moon**,** published in 1931 there is a magnificent drawing of these domes by R. Schlumberger with the following quote, "A little distance to the S (actually N) is a group of low round-topped hills on each summit of which R. Schlumberger, of Mulhouse, has found a crater

BIOGRAPHY

Walter Goodacre (1856-1938) was born in Loughborough, England, but went to live in London when aged 7. Following his education he entered the family business and worked there until retiring in 1929.

Goodacre was an enthusiastic amateur lunar observer. For a while he was Director of the Lunar Section of the Liverpool Astronomical Society and in 1897 he succeeded Thomas Gwyn Elger as the second Director of the Lunar Section of the British Astronomical Association (BAA). Goodacre was President of the BAA in 1922-24.

In 1910, Goodacre published a hand drawn 77-inch diameter map of the Moon; this was reduced to 60 inches and printed in 25 sections, in the manner of Lohrmann and Schmidt, for his 1931 book. The positions were based on 1433 measured points by the British amateur S.A. Saunder; the map itself relied on the photographs of the Paris Observatory atlas. Goodacre's map differs in appearance from others because it avoids any attempt at portraying relief. Some find this makes for a cleaner appearance; others have criticized it as lacking in artistry and failing to live up to the standard of Lohrmann, Mädler, and Schmidt.

pit, 1930, 8 April."

Goodacre's Section VII map is centered on Bullialdus and contains the ruined crater Kies along with the classic Kies Dome.

All illustrations are oriented as in the original publications; this means that north is at the bottom and south at the top.

Lunar nomenclature is established by the International Astronomical Union (IAU), and is rigorously latinized.

MAP OF THE MOON.   S   SECTION II

Drawn by WALTER GOODACRE, F.R.A.S., 1910.
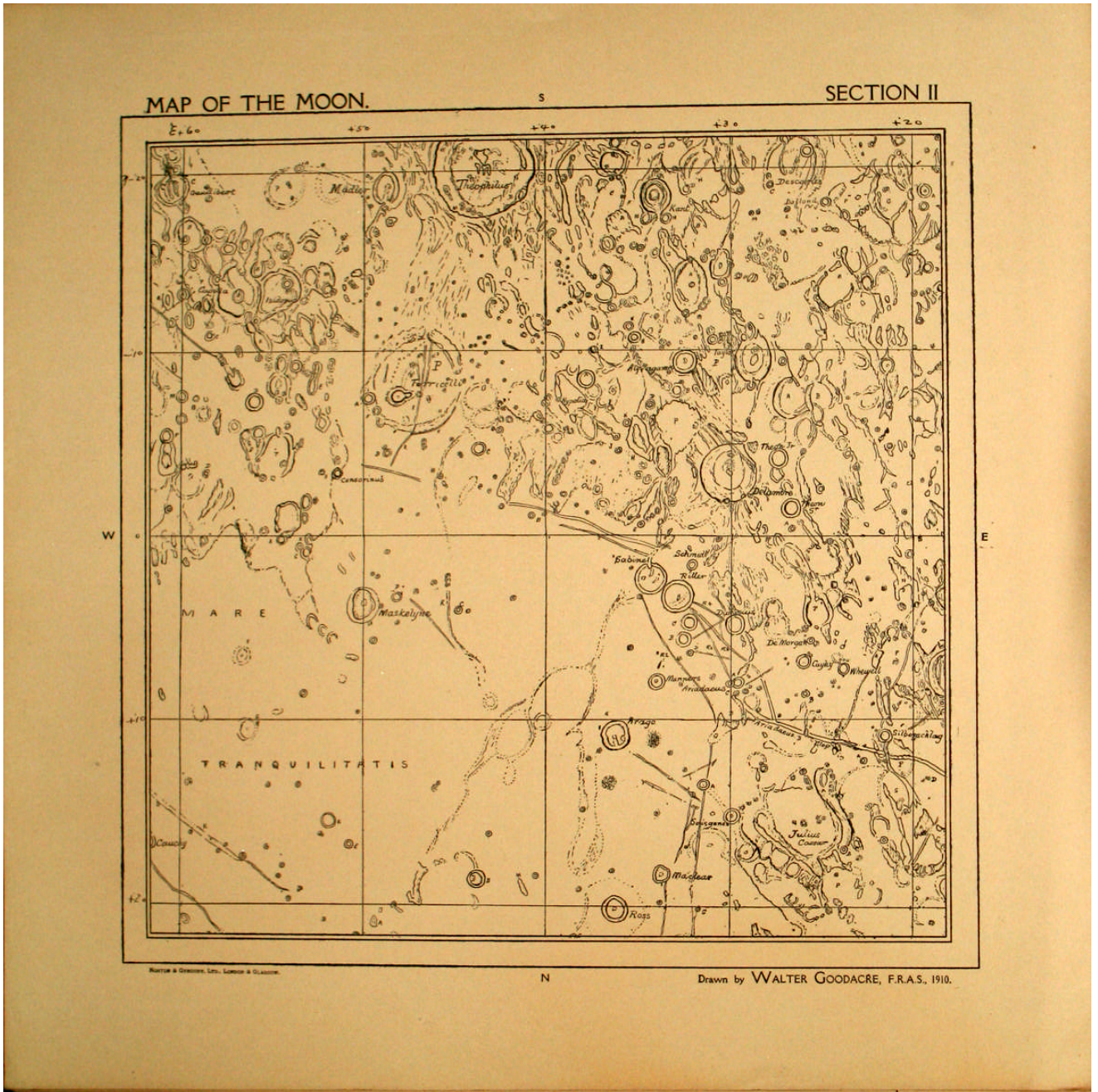
SAMPLES FROM GOODACRE'S MAP

SECTION II

This section embraces the S.E. Quadrant of the M. Tranquillitatis, on the surface and margin of which lie many interesting formations. Mare Tranquillitatis fills an ancient pre-Nectarian impact basin. Arago is a well-known crater located in the western part of Mare Tranquillitatis. Plate II is rich in the numbers of cleft systems present. Of these, the well-known Ariadaeus cleft is the most important. There are also minor systems associated with Sabine and

running along the margin of the Mare beyond Maclear. Though many of the seaward formations show the usual signs of erosion, others further removed from the shore retain their pristine contours. Of these the most noteworthy are Theophilus and Delambre. This section also contains Censorinus, one of the brightest craters on the Moon. On the eastern half of the section are a number of very circular shaped craters including Sabine, Ritter, Cayley and de Morgan.

Several domes are reported in this region. To the north of Arago lies the large lunar dome Arago Alpha (α). A similar-sized lunar dome is located to the west, named Arago Beta (β). Arago Alpha and Beta have very irregular profiles showing protrusions and possible eruptive vents. Between Arago Alpha and the crater Maclear four well-known aligned domes, 5 to 8 km wide, can be found. These domes have formed in basalt. Recently this region has been monitored by the GLR group. A low, previously unreported dome has been observed in this area, near Arago Alpha. It is situated at longitude +21.96° and latitude +7.66° and formed in basalts of relatively high TiO_2 abundance.
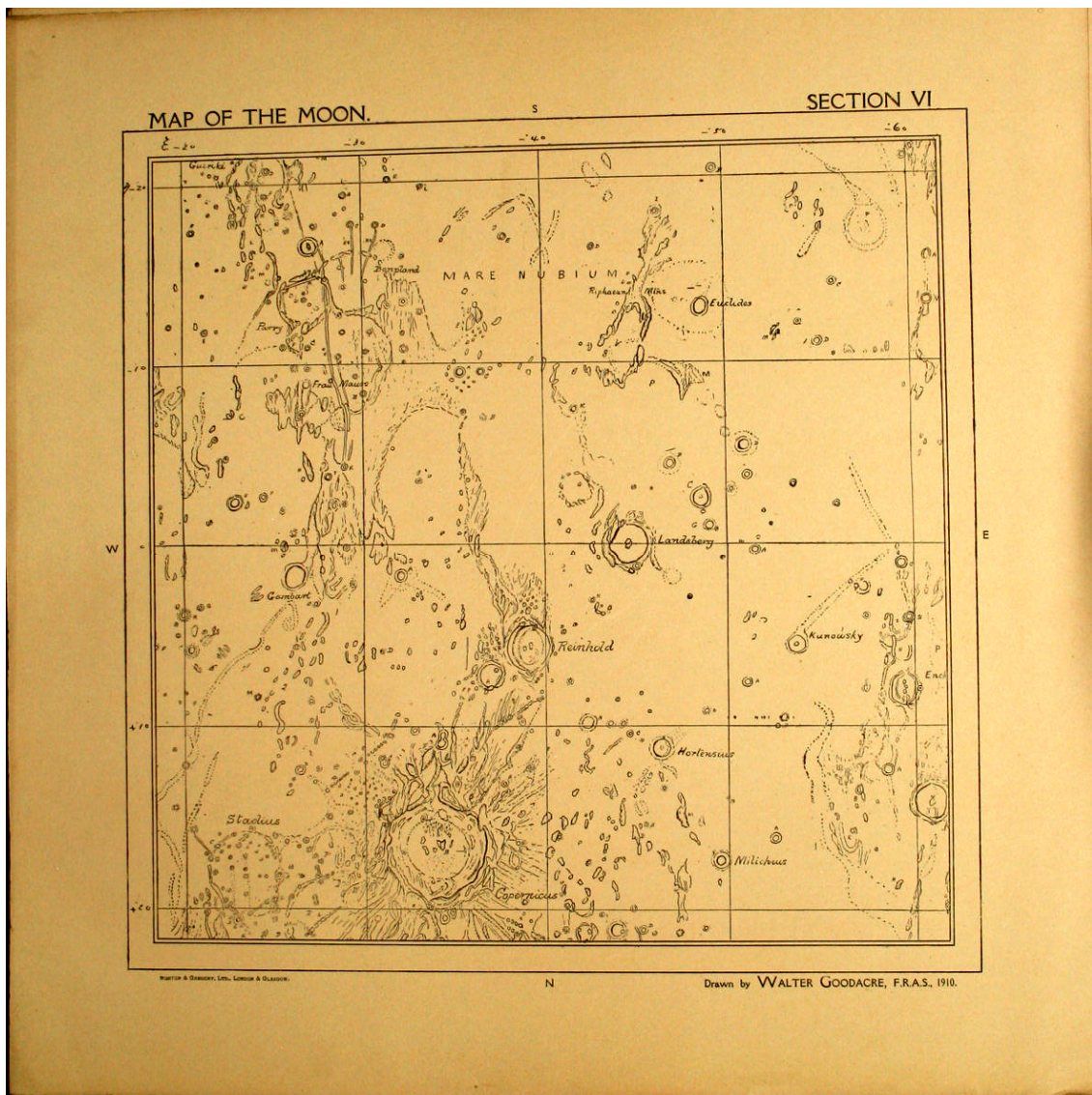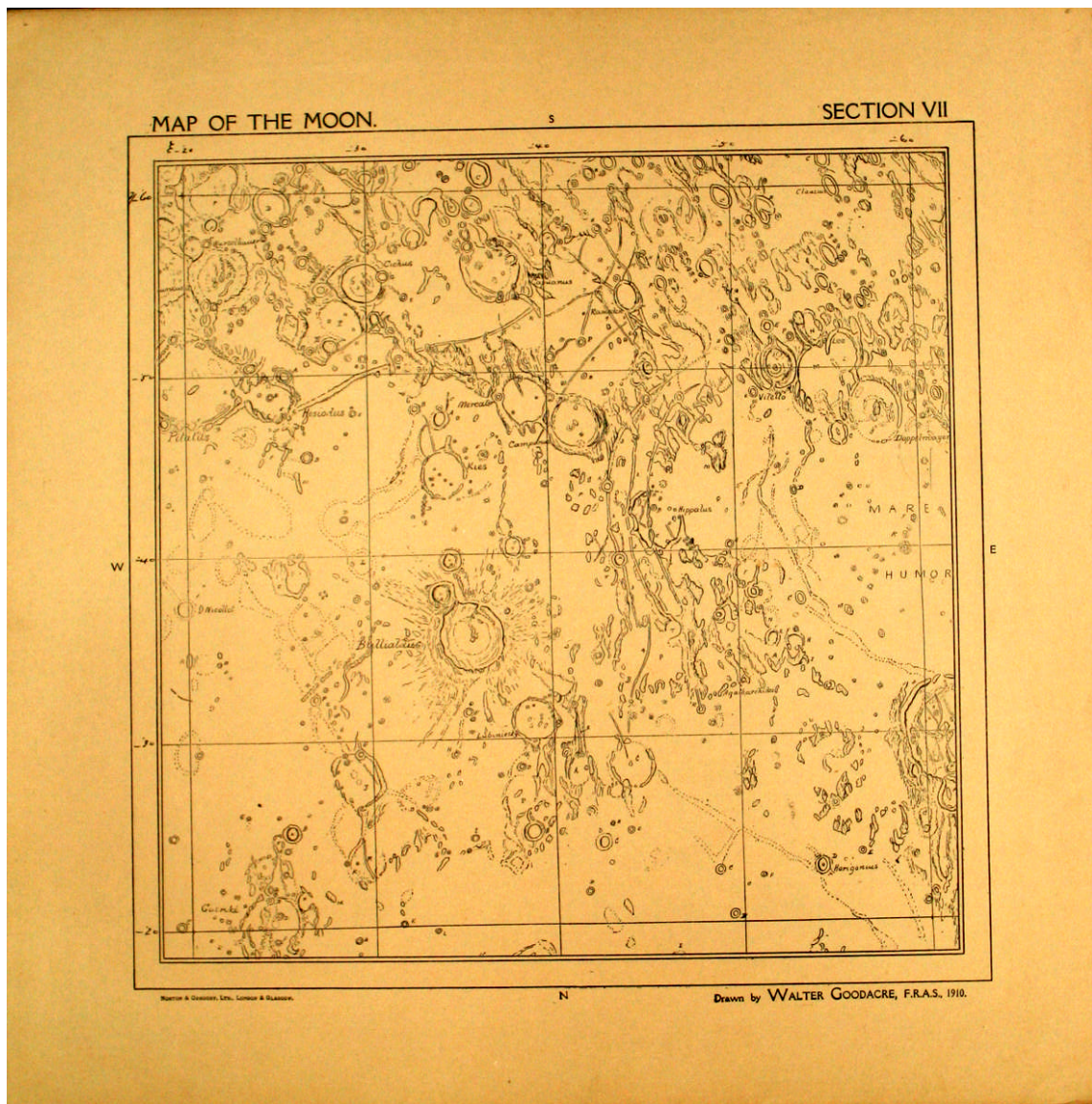
SECTION VI

This section is notable for containing the great crater Copernicus, the finest formation of its class. Except for two other craters, Reinhold and Landsberg, the surface contains few objects of great size. However, there remain many interesting more subtle features including fine example of ruined craters, of which Parry, Bonpland and Fra Mauro are chief. There are no major mountain ranges with only the minor elevations of the Riphaen group present. The most striking features in this area are the numerous examples of ruined formations, pointing eloquently to the destructive forces of ejecta from the formation of mare imbrium. Plate VI also shows the well-know craters, Milichius and Hortensius. The dome field near crater Milichius has been thoroughly studied since Goodacre's map was published. The A.L.P.O. Lunar Dome list reports several low domes in this region. Another comprehensive study of lunar domes was written in 1964 by Brungart. Based on comparisons with terrestrial volcanism these domes were probably formed when mare basalts erupted at a lower rate from a central vent.

SECTION VII

Plate VI is crowded with a great variety of most interesting objects exhibiting examples of every type of formation found on the lunar surface. Bullialdus is the Copernican type of massive crater which shows very little erosion; whilst at the other extreme we have ruined craters like Lubiniesky and Kies. This plate also contains the fine cleft systems associated with Hippalus, Hesiodus and Ramsden. The Western half of the M. Humorum is also included, and Gassendi partially shown. The famous crater Kies is here**.** Only the most superior part of its walls is visible, while the remainder is buried under this large plain. In the immediate vicinity of Kies crater we can see an example of a classic lunar dome with central crater pit, Kies Pi. This dome is a prominent lunar dome, and lies 20 km west of Crater Kies. The summit crater is a good object for steady skies.

[Editor note: please note that items in blue text and Goodacre's map have links to full resolution figure].